Development of High-performance Off-line and In-line Optical Coherence Tomography Techniques

Zijian Zhang

Department of Electrical Engineering and Electronics
University of Liverpool

Thesis submitted in accordance with the requirements of
the University of Liverpool
for the degree of
Doctor of Philosophy

September 2019

Copyright

Table of Content

List of Figures

List of Tables

Acronyms and Abbreviations

1D	One-Dimensional
2D	Two-Dimensional
3D	Three-Dimensional
AC	Alternating Current
AFM	Atomic Force Microscopy
API	Active Pharmaceutical Ingredient
ATP	Adenosine Triphosphate
CCD	Charge-Coupled Device
CMOS	Complementary Metal–Oxide–Semiconductor
CS	Compressive Sensing
CT	Computed Tomography
DC	Direct Current
DOF	Depth of Focus
FF-OCM	Full-Field Optical Coherence Microscopy
FF-OCT	Full-Field Optical Coherence Tomography
FFT	Fast Fourier Transform
FSIM	Feature Similarity
FWHM	Full Width at Half Maximum
Ge:Ga	Gallium doped Germanium
GSK	GlaxoSmithKline
LCI	Low-Coherence Interferometry
LED	Light-Emitting Diode

LF-OCT	Line-Field Optical Coherence Tomography
LIA	Lock-in Amplifier
LSF	Line Spread Function
MMSE	Minimum Mean Square Error
MRI	Magnetic Resonance Imaging
NA	Numerical Aperture
OCT	Optical Coherence Tomography
OPD	Optical Path Difference
PAT	Process Analytical Technologies
PCB	Printed Circuit Board
PSF	Point Spread Function
PSNR	Peak Signal-to-Noise Ratio
QCLs	Quantum Cascade Lasers
RI	Refractive Index
RIP	Restricted Isometry Property
ROI	Region of Interest
SD-OCT	Spectral-Domain Optical Coherence Tomography
SEM	Scanning Electron Microscope
SLD	Superluminescent Diode
SLM	Spatial Light Modulator
SNR	Signal-to-Noise Ratio
SRI	Stain Removal Index
SSIM	Structural Similarity
SS-OCT	Swept-Source Optical Coherence Tomography

TD-OCT	Time-Domain Optical Coherence Tomography
THz-TDS	Terahertz Time-Domain Spectroscopy
TPI	Terahertz Pulsed Imaging
UHR	Ultrahigh-Resolution
XμCT	X-ray Micro Computed Tomography

Acknowledgements

First and foremost, I would like to express my sincere gratitude to my supervisors Prof. Yaochun Shen and Prof. Yi Huang. I thank you both for your invaluable guidance and persistent support for my research. Without your guidance, this dissertation would not have been possible. I would also like to thank Dr. Hungyen Lin and Dr. Yalin Zheng for our close collaboration and great learning opportunities. It is my great honour and appreciation to become one of the PhD candidates in Prof. Yaochun Shen's group that always stimulates original ideas and insightful thoughts. I have thoroughly enjoyed the intellectual delight in our group. The beneficial discussions and selfless help from my colleagues are also much appreciated.

I would like to thank my family members, especially my wife, Ms. Yiyi Wang, my parents and my parents in law. Without their support during the whole of my academic years, I would not have been able to achieve my research goals.

Finally, deep gratitude and appreciation to my research lab colleagues: Dr. Samuel Lawman, Dr. Bryan Williams, Dr. Yue Dong, Dr. Jinke Zhang, Mr. Xiaoran Li, Mr. Xingyu Yang, Mr. Xinhua Li and Mr. Zhiyi Zhao as well as my research collaborators: Prof. Axel Zeitler, Dr. Lu Gan, Dr. Daniel Markl, Dr. Uyai Ikpatt and Dr. Alexander Valavanis. I have enjoyed working with you all, and I appreciate the help and support you all have provided during my research pursuit.

List of Publications

Journal Publications:

[1] **Z.J. Zhang**, U. Ikpatt, S. Lawman, B. Williams, Y.L. Zheng, H. Lin, and Y.C. Shen, "Sub-surface imaging of soiled cotton fabric using full-field optical coherence tomography," *Optics Express*, Vol. 27, no. 10, pp. 13951-13964, 2019.

[2] **Z.J. Zhang**, B. Williams, Y.L. Zheng, H. Lin, and Y.C. Shen, "Differentiating Generic versus Branded Pharmaceutical Tablets Using Ultra-High-Resolution Optical Coherence Tomography," *Coatings*, Vol. 9, no. 5, pp. 326, 2019.

[3] **Z.J. Zhang**, L. Liu, A.B Sajak, L. Gan, Y. Huang, Y.C. Shen, "Spinning Disk as a Spatial Light Modulator for Rapid Infrared Imaging," *IET Microwave, Antennas & Propagation*, Vol. 11, no. 3, pp. 317-323, 2017.

[4] H.Y. Lin, **Z.J. Zhang**, D. Markl, J.A. Zeitler, and Y.C. Shen, "A Review of the Applications of OCT for Analysing Pharmaceutical Film Coatings," *Applied Sciences*, Vol. 8, no. 12, pp. 2700, 2018.

[5] H. Lin, Y. Dong, D. Markl, **Z.J. Zhang**, Y.C. Shen, J.A. Zeitler, "Pharmaceutical film coating catalogue for spectral-domain optical coherence tomography", *Journal of Pharmaceutical Sciences*, Vol. 106, no. 10, pp. 3171-76, 2017.

[6] J.K. Zhang, B. Williams, S. Lawman, A. Dave, **Z.J. Zhang**, Y.L Zheng, Y.C. Shen, "Non-destructive Analysis of Flake Properties in Automotive Paints with Full-field Optical Coherence Tomography and 3D Segmentation", *Optics Express*, Vol. 25, no. 16, pp. 18614-28, 2017.

[7] Q. Zhang, P. Wang, H. Chen, Q.L. Huang, H.B. Jiang, **Z.J. Zhang**, Y.M. Zhang, X. Luo, S.J. Sun, "A novel method for urban area extraction from VIIRS DNB and MODIS NDVI data: a case study of Chinese cities", *International Journal of Remote Sensing*, Vol. 38, no. 21, 2017

[8] T. Sun, J.G. Liu, Y. Shi, W. Chen, Q.Q. Qin, **Z.J. Zhang**, "Computational imaging from non-uniform degradation of staggered TDI thermal infrared imager", Optics Express, Vol. 23, no. 19, pp. 24572-85, 2015.

Conference Publications:

[1] **Z.J. Zhang**, D. Markl, H. Lin, J.A. Zeitler, Y.C. Shen, "Imaging pharmaceutical micropellets with optical coherence tomography: a preliminary study", Pharmaceutical Solid State Research Cluster (PSSRC), Graz, Austria, 2017.

[2] **Z.J. Zhang**, L. Gan, Y. Huang, Y.C. Shen, "Compressive Terahertz Imaging: Deep Learning based Rapid Imaging Reconstruction Scheme", Poster Session at 2017 IEEE 10th UK-Europe-China Workshop on Millimetre Waves and Terahertz Technologies (UCMMT), Liverpool, U.K., 2017.

[3] **Z.J. Zhang**, L. Liu, X.R. Li, L. Gan, Y. Huang, Y.C. Shen, "Compressive Sensing for Rapid IR Imaging", on IET Colloquium on Millimetre-Waves and Terahertz Engineering & Technology, London, U.K., pp. 1-6, 2016.

[4] L. Liu, **Z.J. Zhang**, L. Gan, Y.C. Shen, Y. Huang, "Terahertz Imaging with Compressed Sensing", on 2016 IEEE 9th UK-Europe-China Workshop on Millimetre Waves and Terahertz Technologies (UCMMT), Qing Dao, China, 2016.

Work to be Submitted:

[1] **Z.J. Zhang**, H.Y. Lin, D. Markl, B. Williams, Y.L. Zheng, J.A. Zeitler, Y.C. Shen, "High Resolution imaging of multi-layered micropellet by full-field optical coherence tomography", for Journal of Pharmaceutical Sciences.

Abstract

Optical Coherence Tomography (OCT) is a non-destructive and non-contact optical technology that can produce depth profiles of three-dimensional (3D) objects. It was primarily developed and used for ophthalmic applications but utilising the technology in the field of non-destructive testing has increased in popularity. Examples of previously demonstrated applications range from the art diagnostics, polymers, subsurface defect detection, pharmaceutical tablet film coatings, automotive paints analysis, and the investigation of silicon integrated circuits. Imaging with OCT is based on low-coherence interferometry and typically achieved with a Michelson interferometer. The imaging modality is able to decouple the axial and lateral resolutions, where the former is governed by the temporal coherence of the illumination source, while the latter is primarily determined by the Numerical Aperture (NA) of the focus lens.

A single-shot Spectral-Domain OCT (SD-OCT) system has been developed to realise the in-line monitoring of the pharmaceutical pellet coating process. The system is arranged based on fibre optics, which features the advantages of compactness and portability. The use of a customised light source makes the whole system cost-effective. Considering that the developed coaters (i.e. pan coater and fluid bed coater) do not provide a specific Processing Analytical Technologies (PAT) port for an OCT sensor, the system employs an adjustable sensor head which can be integrated into a coater device. The achieved axial resolution of 9 µm, and the acquisition rate of faster than 40 KHz enables the changes in coating thickness to be resolved. The system has been tested in a real-world pellet coating process in a major pharmaceutical company. The pilot study result is part of the paper (DOI: https://doi.org/10.1016/j.xphs.2017.05.032**)** published in the *Journal of Pharmaceutical Sciences*.

A high-resolution Full-Field OCT (FF-OCT) system has been developed to investigate its applicability in the pharmaceutical industry, including the imaging of multi-layer micropellet (diameter < 1 mm) and the thin coating (thickness < 10 µm) used in Panadol tablet. Novel applications such as assessment of stain removal from cotton fabric and kitchen countertop were also studied. By aligning a broadband Light-Emitting Diode (LED) source and two identical objectives with an NA of 0.3, the system achieved an

axial resolution of 0.98 μm and 1.6 μm laterally. In addition, a complete software-based postprocessing method was developed for OCT image reconstruction. The measurement can be therefore operated continuously rather than employing the traditional phase shift method. The study relative to the thin coating used in Panadol tablet has been published in the *Journal of Coatings* (DOI: https://doi.org/10.3390/coatings9050326), and the application in the detergent industry has been published in the *Journal of Optics Express* (DOI: https://doi.org/10.1364/OE.27.013951).

In order to develop cutting-edge OCT technology, the Compressive-sensing (CS) based imaging technique has been studied. A block Toeplitz matrix based measurement matrix has been proved to offer a higher compression rate, and it can guarantee a close reconstruction quality as those fully random matrices used in CS imaging. This, therefore, is particularly suited to relieve memory burden that is required by three-dimensional (3D) imaging techniques such as OCT. As the first-step study, the developed measurement matrix was fabricated to a mechanically Spatial Light Modulator (SLM). The optical imaging in both infrared and terahertz frequencies have been investigated. The relevant work has been published in the *Journal of IET Microwave, Antennas & Propagation* (DOI: 10.1049/iet-map.2016.0398).

Chapter 1 Introduction

1.1 Research Overview

Optical Coherence Tomography (OCT) has been one of the most state-of-the-art and rapidly emerging imaging technologies in the last decades. OCT is often described as the optical analogue to ultrasound since it probes the sample with light instead of sound and maps the reflectivity as a function of depth. OCT is capable of providing real-time cross-sectional images, resolving the sample's inner structures with decoupled and high lateral and axial resolutions. Compared with other high-resolution optical imaging technique, such as confocal microscopy, it can achieve better penetration depth into a scattering sample. OCT is comparably inexpensive, capable of real-time imaging, and, uses non-ionizing imaging beam, which means it is safe for repeated examinations. With these advantages, OCT has illustrated the irreplaceability amongst popular tomography modalities such as ultrasound imaging, magnetic resonance tomography and X-ray computed tomography.

The first OCT device was demonstrated in 1991 to realise the imaging of the retina and the human coronary artery. For several years, OCT has been commercially available and accepted as a clinical standard within ophthalmology for diagnosis of retinal diseases [**1**]. Since the commercialisation of the first OCT systems by Humphrey Instruments (now owned by Carl Zeiss Meditec) in 1996, the market has rapidly grown. At present, there are more than 20 system manufacturers and a substantial number of suppliers for components and equipment [**2**]. Recently, the first commercial systems for intravascular imaging in cardiology have entered the market and were approved in the United States (US), Europe and Asia [**3**]. Emerging applications within biology, medicine and various technical fields are continuously explored by many research groups worldwide. In parallel, intense efforts are aiming at technological improvements in terms of imaging speed, resolution, image quality and functional capabilities.

From the perspective of economic impact, the estimated OCT system revenue is approaching £0.8 billion per year. Since the first commercial OCT was released, cumulative revenue has likely exceeded £4 billion [**4**]. Another measure to show the OCT's economic impact is the number of direct and indirect jobs created by the OCT

related marketplace. The studied data indicates that the OCT industry will have provided approximately 20,000 person-years of cumulative high-quality jobs [**4**].

Additionally, according to the information from the website of 'OCT News', in the contemporary market place, more than 300 organizations are undertaking OCT relevant research, more than 150 companies have been created to develop commercial OCT instruments, over 1000 OCT patents have been granted, and more than 25000 OCT research articles have been published [**3,4**].

The discovery, commercialisation, and growth of OCT over the past 25 years has been highly impactful scientifically, clinically, and economically. A complex worldwide ecosystem has advanced OCT to where it is today and will continue to power OCT into the future. Ultimately, multiple incremental and evolutionary advances can become translational and revolutionary, provided they are chosen carefully and executed efficiently. There are many exciting technology and application frontiers for OCT yet to be developed. On the technology side, there will be innovations in hardware, optics, systems, devices, light sources, multimodality imaging, medical devices, advanced display techniques and image processing. On the application side, only a few of the potential fields have been commercialised. There are several novel applications that could create broader markets to promote economic growth and benefit the lives of individuals in the foreseeable future.

1.2 Thesis Motivation

1.2.1 Inspection of Pharmaceutical Film Coating by OCT

Pharmaceutical film coatings are typically polymeric films formed from an aqueous latex dispersion. Coatings are generally used to protect the Active Pharmaceutical Ingredients (APIs) from light and moisture as well as to improve the visual appearance, taste masking and in some cases, brand differentiation. In advanced coatings, they serve a functional purpose to control the release rate of the APIs [**5**]. As the coating quality has a direct impact on therapeutic efficiency, there is a critical need for the use of analytical techniques to assess the film coating structures [**6,7**].

To date, various non-destructive techniques have been applied to assess pharmaceutical coating structures. These techniques include spectroscopic methods like near-infrared and Raman spectroscopy and imaging methods such as nuclear magnetic resonance imaging, Terahertz Pulsed Imaging (TPI) and OCT. Amongst all these different methods, TPI and OCT are attractive because they offer a direct calibration-free coating thickness measurement, where the only unknown element is the coating refractive index that can be obtained as a one-off measurement. TPI technique realises time-resolved and coherent detection, where the obtained time-domain spectrum with high Signal-to-Noise Ratio (SNR) provides information about the internal structure of the sample. Thus, the thickness of a coating can be directly determined by the time delay of the reflected pulses from different interfaces. The achieved spatial resolution by the reported TPI systems is 150–250 μm in the lateral and 30–40 μm in the axial directions.

In contrast to TPI, where submillimeter wavelengths are used for imaging, OCT exploits the light sources with near-infrared or visible frequencies to image the pharmaceutical coatings. OCT measurements are based on Low-Coherence Interferometry (LCI) and are typically achieved with a Michelson interferometer as the core part. OCT decouples the axial and lateral resolutions, in which the temporal coherence of the used light source determines the axial resolution and the used objective determines the lateral resolution. This allows both the high axial and lateral resolutions. To characterise even a thinner or more complex film coatings and to understand the coating process insightfully, there is a need to develop therefore high-performance OCT technique for both off-line and in-line measurements of pharmaceutical coatings.

1.2.2 Evaluation of Detergent Cleaning Efficiency by OCT

The ability to measure and monitor the removal of semi-solid fats or oils from a fabric or a hard surface substrate is important for the assessment of the effectiveness of a detergent product. Currently, the colourimetry method has been widely employed in wash studies to quantify colour and to derive colour differences from the soiled samples before and after washing [**8–10**]. The colorimetric evaluation according to a CIELAB system can be used for all the measured samples, where the ΔE* values between the washed and unwashed samples, as well as between the washed and unsoiled samples, represent the criteria for the soil removal efficiency. Although the colourimetric method is easy to use, it requires the measured sample to be dyed (indirect measurement), and it cannot provide depth-resolved information.

OCT is a non-destructive and non-contact optical detection technology that is capable of producing the depth profiles of measured samples. It has been well studied for ophthalmic applications, but interest in the field of non-destructive testing has also increased. Time-Domain (TD) Full-Field (FF) OCT imaging technique is first implemented on a commercial microscope body using an infrared Light-Emitting Diode (LED) light source. In an FF-OCT system, a Two-Dimensional (2D) detector array is used for image data acquisition rather than using a single pixel photodiode in a standard TD-OCT setup. Such paralleled imaging modality enables the capture of a 2D *en-face* image in single exposure time, and there is, therefore, no lateral scanning required by an FF-OCT measurement. Three-Dimensional (3D) volumetric data can be registered with a single depth scanning that moves either the reference or sample arms axially. High-resolution FF-OCT is very suited for the visualisation of the cleaning effect after the measured sample is washed by a detergent product. The changes from the sub-surface area between the washed and unwashed fabrics can be discriminated since the number of imaged fibres/fibrils will increase along with the removal of the soil from the sub-surface area. As for a hard surface sample such as kitchen countertop, FF-OCT can be also implemented as a surface profilometry tool to generate therefore surface topography image. Depending on the soil adhered on the hard surface, the derived height and the distribution information of the soil can be used to assess the soilability/cleanliness before and after washing the hard surface sample.

1.2.3 Compressive Sensing Technique for New-generation OCT

Compressive Sensing (CS) is a recent, growing field that has attracted substantial attention in signal processing, statistics, computer science and other scientific disciplines. CS can be used to acquire signals which are either sparse or compressible [**11**]. Sparsity is the inherent property of those signals for which, the whole of the information contained in the signal can be represented only with the help of a few significant components, as compared to the total length of the signal. There is the fact that a signal has sparse representation either in the original domain or in some transform domains such as cosine transform, Fourier transform, wavelet transform, etc. Studies have demonstrated that natural images are able to be sparsely represented in the wavelet domain, and speech signal can be represented by fewer components using Fourier transform, and a better model for medical images can be obtained using Radon transform. As a result, CS simplifies the signal acquisition by taking far fewer random measurements [**12,13**].

Combining CS and OCT techniques to develop a new-generation OCT system has significant advantages. For conventional Spectral-Domain OCT (SD-OCT), a spectrometer with few thousands of pixels is commonly used. The imaging depth of an SD-OCT is determined by the spectral resolution of the used spectrometer. Better imaging depth usually requires higher performance of spectrometer, such as having more sensor elements. This, therefore, results in a trade-off between the higher axial resolution and the better imaging depth due to the limitation of sampling by the Nyquist-criterion for a spectrometer. For conventional FF-OCT, the imaging speed is mainly determined by a frame rate of the used 2D Charge-Coupled Device (CCD) or Complementary Metal–Oxide–Semiconductor (CMOS) camera. However, a good-quality 3D OCT data requires finer scanning. This results in a slow measurement time due to the limited imaging speed of the camera, and the acquired 3D datacube may significantly increase storage burden. CS technique, in principle, is capable of solving the challenges because the achievable sampling performance is governed by the signal sparsity rather than the Nyquist-rate relied on the sampling device.

1.3 Thesis Outline

Chapter 2 begins by introducing the development of OCT technique. Then a detailed mathematical theory and the imaging mechanism of conventional TD-OCT and SD-OCT are explained by using equations and schematic diagrams. A systematic comparison is also discussed between TD-OCT and SD-OCT techniques from the aspects of system configuration, imaging theories and performance metrics, such as axial resolution, lateral resolution, imaging depth and signal to noise ratio. In addition, parallel OCT imaging schemes that are suited for fast 3D imaging are introduced, including FF-OCT and Line-Field (LF) OCT techniques.

Chapter 3 firstly reviews the reported OCT techniques that have been utilised for pharmaceutical applications, followed by a discussion of the achievements and challenges. A cost-effective SD-OCT system is presented in this chapter aiming at characterising pharmaceutical film coatings with tens of μm. The system design achieved performances and measurement settings are detailed. The developed SD-OCT, as an off-line inspection tool, is used to investigate the imaging applicability of 22 pharmaceutical tablets with differently common coating formulations. The SD-OCT is also used as a Process Analytical Technology (PAT) tool to in-line monitoring of the coating process of a pilot-scale pellet sample (3 Kg) with a fluid-bed coater.

Chapter 4 delivers an FF-OCT system with ultrahigh resolution as a powerful off-line inspection tool for pharmaceutical applications. Different from the phase-shift method that has been widely used in the conventional FF-OCT system, a continuous measurement scheme is presented in this chapter. The system design, reconstruction method, achieved performances and operation settings are then discussed. The FF-OCT system is used to differentiate generic and branded paracetamol tablets by resolving a thin film coating from Panadol tablets. The FF-OCT system is also used to characterise the inner micro-structures of multi-layer micropellets (diameter <1 mm), where a 3D segmentation technique is presented in order to obtain a high-resolution thickness map. In addition, X-ray Micro Computed Tomography (XμCT) technique is used to validate the FF-OCT system for the imaging of the same micropellet, where a Skyscan 1172 XμCT device was employed with an isotropic voxel size of 0.95 μm in both axial and lateral directions. The Skyscan 1172 provides better axial and lateral resolution performance than the one achieved by the developed FF-OCT (such as 1-μm axial

resolution and 1.6-µm lateral resolution). It is therefore a reliable tool for the validation of the FF-OCT measurement. It should be pointed out that the pellet sample was fixed on a Blu Tack with a clear mark prior to the measurement, thus guaranteeing the same measurement area on the pellet for both the FF-OCT and XµCT. In addition, the XµCT measurement was carried out at Cambridge University by our collaborator (Dr Daniel Markl).

Chapter 5 investigates the applicability of using the developed FF-OCT to assess the effectiveness of detergent washing from soiled cotton fabrics. This enables the tested fabric to be free of dyeing when compared with the conventional colourimetry method. The differences that exist in the sub-surface areas of clean, washed and soiled samples are discriminated by the FF-OCT. A cleaning effect quantification method, which is based on the analysis of the sub-surface fibres is presented, and the result is validated by the gold standard method of colourimetry. The FF-OCT is also used for imaging soiled countertops (treated with different-level of kitchen soils) to evaluate the soilability. In this study, the FF-OCT is operated as a non-invasive and non-contact surface profilometry tool to obtain the 3D surface topography image.

Chapter 6 reports cutting-edge imaging technique related to compressive imaging aiming at developing CS-OCT technology. A mechanical Spatial Light Modulator (SLM) is designed based on a block Toeplitz measurement matrix. It demonstrates a close image reconstruction ability when comparing with other fully random measurement matrices. A series of simulations are carried out for the discussion of the imaging performance of the SLM at different imaging frequencies. As a preliminary study, the SLM is deployed in a single-pixel imaging system (driven by a visible light source) to achieve a video-rate (10 frames per second) compressive imaging. Furthermore, the SLM is used to investigate the compressive imaging in terahertz (THz) frequency. In particular, a 3D THz imaging beam profile is compressively acquired and reconstructed.

Chapter 7 summarises all the completed work that has been achieved in this thesis, the key contributions and findings. The potential problems are identified, and recommendations for future optimisation are discussed.

References

[1] J. G. Fujimoto, "Optical coherence tomography," C. R. Acad. Sci. Paris Ser. IV 2, pp. 1099 – 1111, 2001.

[2] G. Smolka, "Optical coherence tomography – 2010: Technology, applications, and markets," Market Report OM-51, Strategies Unlimited, 2010.

[3] S. Marschall, B. Sander, M. Mogensen, T. M. Jørgensen and P. E. Andersen, "Optical coherence tomography—current technology and applications in clinical and biomedical research," Analytical and Bioanalytical Chemistry, vol. 400, no. 9, pp. 2699-2720, 2011.

[4] J. G. Fujimoto and E. A. Swanson "The development, commercialization, and impact of optical coherence tomography," Investigative Ophthalmology & Visual Science, vol. 57, no. 9, pp. OCT1-OCT13, 2016.

[5] G. M. Jantzen, J. R. Robinson, "Sustained-and controlled-release drug delivery systems," Drugs and The Pharmaceutical Sciences, vol. 72, pp. 575-610, 1996.

[6] J. A. Zeitler, Y. C. Shen, C. Baker, P. F. Taday, M. Pepper, and T. Rades, "Analysis of coating structures and interfaces in solid oral dosage forms by three-dimensional terahertz pulsed imaging," Journal of Pharmaceutical Sciences, vol. 96, no. 2, pp. 330-340, 2007.

[7] Y. C. Shen and P. F. Taday, "Development and application of terahertz pulsed imaging for nondestructive inspection of pharmaceutical tablet," IEEE Journal of Selected Topics in Quantum Electronics, vol. 14, no. 2, pp. 407-415, 2008.

[8] G. van Dalen, A. Don, J. Veldt, E. Krijnen, and M. Gribnau, "Colour analysis of inhomogeneous stains on textile using flatbed scanning and image analysis," in Conference on Colour in Graphics, Imaging, and Vision, 2008.

[9] E. Ilec, B. Simončič, and A. Hladnik, "Evaluation of surfactant detergency using statistical analysis," Textile Research Journal, vol. 79, no. 4, pp. 318-325, 2009.

[10] S. Shivaji Biranje, A. Nathany, N. Mehra, and R. Adivarekar, "Optimisation of detergent ingredients for stain removal using statistical modelling," Journal of Surfactants and Detergents, vol. 18, no. 6, pp. 949-956, 2015.

[11] D. L. Donoho, “Compressed sensing,” IEEE Transactions on Information Theory, vol. 52, no. 4, pp. 1289–1306, 2006.

[12] H. Shen, L. Gan, N. Newman, Y. Dong, C. Li, Y. Huang, and Y. C. Shen, "Spinning disk for compressive imaging," Optics Letters, vol. 37, no. 1, pp. 46-48, 2012.

[13] M. F. Duarte, M. A. Davenport, D. Takhar, J. N. Laska, T. Sun, K. F. Kelly, R. G. Baraniuk, "Single-pixel imaging via compressive sampling," IEEE Signal Processing Magazine, vol. 25, no. 2, pp. 83-91, 2008.

Chapter 2 Optical Coherence Tomography Technique

2.1 The Development of OCT

Tomography technology has been developed for over five decades [**1–5**]. The inventions of Computed Tomography (CT), Magnetic Resonance Imaging (MRI) and Ultrasonography enable the cross-sectional imaging of a scanned object (by ionising radiation in X-ray CT, magnetic fields in MRI or ultrasound waves in Ultrasonography) [**6–10**]. The internal structures of an object can be observed without cutting. Both the CT and MRI techniques have already been well applied in radiology and medical diagnosis to investigate anatomy and physiology, and the Ultrasonography has been widely utilised to examine the growing foetus inside a pregnant woman's uterus.

Optical Coherence Tomography (OCT) is an imaging technique which work similar to ultrasound; It simply uses light waves instead of sound waves [**3**]. By using the time-delay information contained in the light waves, which has been reflected from different depths inside a sample, an OCT system can reconstruct the depth profile of the sample structure. Three-dimensional (3D) images can then be created by scanning the light beam laterally across the sample surface. While the lateral resolution is determined by the spot size of the light beam, and the axial resolution depends primarily on the optical bandwidth of the light source. For this reason, OCT systems may combine high axial resolutions with large depths of field, so their primary applications have included *in vivo* imaging through thick sections of the biological systems, particularly in the human body [**11–21**]. The technique has already become established as a standard imaging modality for imaging of the eye [**11–16**], with many commercial instruments on the market. The application of OCT imaging to other biomedical areas, such as endoscopic imaging of the gastrointestinal and cardiovascular systems is currently an active field of research [**17–21**].

OCT may be directly compared with other tomography-relative techniques in terms of multiple criteria, such as resolution, imaging depth, acquisition rate, technology complexity, sample intrusiveness and device cost. Considering the first two, there is a niche occupied by the OCT technique as represented in Fig. 2.1. It is noticeable that its imaging depth is limited to a few millimetres, less than ultrasound [**8**], CT [**6**] or MRI

[**9**]; however, its resolution is better. This comparison is reversed concerning confocal microscopy. Like ultrasound, the acquisition time of OCT is short enough to support tomographic imaging at video rates, making it much more tolerant to subject motion than either CT or MRI. OCT does not require physical contact with the measured samples. OCT uses non-ionising radiation at biologically safe levels, allowing for long exposure time, and its level of complexity is closer to ultrasound than to CT or MRI, allowing for the realisation of low-cost portable scanners. The point-scanning nature of OCT technology allows it to be implemented in fibre optics, which makes endoscopic and catheter-based imaging possible [**17**].

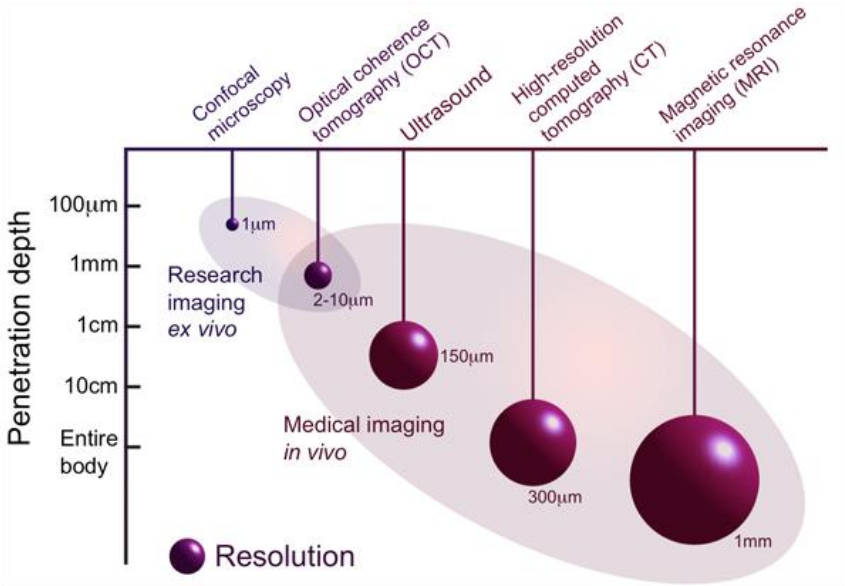

Figure 2.1 Comparison of Optical Coherence Tomography (OCT) resolution and imaging depths to those of alternative techniques. The "pendulum" length represents imaging depth, and the "sphere" size represents resolution (adapted from OBEL website)

There are two main categories of OCT instrumentation: Time-Domain OCT (TD-OCT) and Spectral-Domain OCT (SD-OCT). TD-OCT technology is more intuitive to understand, and most early research and commercial instrumentations were based on it [**22–32**]. SD-OCT is rapidly replacing the TD-OCT technology in most applications because it offers significant advantages in sensitivity and imaging speed [**33–43**].

Time-Domain OCT Development

In 1991, OCT was first demonstrated by Huang *et al*. [**22**], as shown in Fig 2.2. By the introduction of Low-Coherence Interferometry (LCI) technique in the time domain, the

system generated cross-sectional images by measuring the echo time delay and the intensity of light that was reflected/backscattered from the internal tissue microstructures. The system was aligned based on fibre optics and illuminated by a Superluminescent Diode (SLD) with a central wavelength at 830 nm. When the light reflected from each retinal layer combined with the light reflected from the reference mirror, the interferometric signal was recorded by using a photodiode. By displacing the reference mirror to different distances from the retina, the registered signal for the light reflected from each respective retinal layer formed a depth profile.

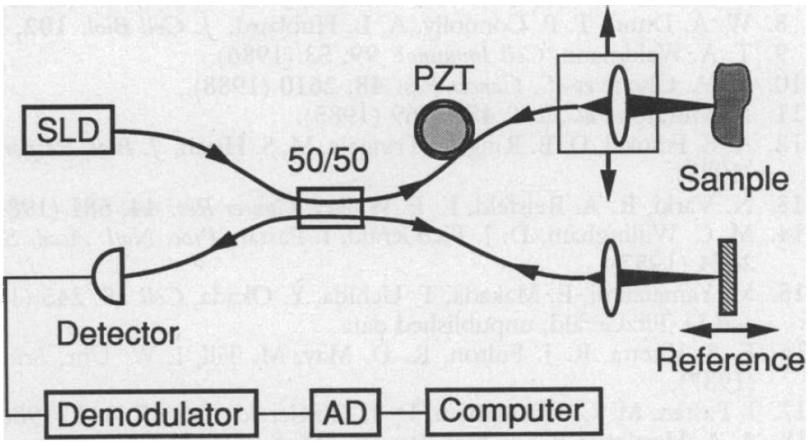

Figure 2.2 Schematic diagram of Huang's OCT system. (Adapted from Huang *et al*. [**22**])

A conventional TD-OCT requires two scans to obtain a cross-sectional image (B-scan): the lateral OCT scan addresses laterally adjacent sample positions, and the OCT depth-scan detects depth positions of the light re-emitting sites in the sample. Despite the apparent limitation in the measurement time of a standard TD-OCT, first commercial OCT instrument, the Zeiss OCT, was introduced in 1996.

In 1999, an Ultrahigh-Resolution (UHR) TD-OCT system was firstly presented by Drexler *et al* [**23**]. The proposed system deployed a Kerr-lens mode-locked Ti: sapphire laser that emitted sub-two-cycle pulses, corresponding to spectral bandwidths of up to 350 nm. This contributed to the ultrahigh axial resolution of about 1 μm in tissue, which demonstrated the potential of *in vivo* imaging of human cells.

In 2004, Tony *et al*. used two multiplexed broadband SLDs to achieve an ultrahigh axial resolution of 4.3 μm [**24**]. Specifically, the improvement was contributed by two spectrally multiplexed, independently driven SLD diodes operating at 840 nm and 920

nm, respectively. The SLDs had optical outputs with overlapping spectral bands that could be combined with a broadband fibre coupler. As a result, the combined SLD provided a spectral bandwidth of 155 nm and a central wavelength of 890 nm, and UHR retinal OCT images were acquired.

Despite these advances in resolution, several limitations remained. Although high-performance SLD light sources became available, which could achieve the UHR TD-OCT without the need for expensive femtosecond lasers, the limited detection sensitivity of an OCT with time-domain detection affected the image acquisition speeds.

Spectral-Domain OCT Development

SD-OCT was firstly reported by Fercher *et al.* in 1995 [**25**], as shown in Fig. 2.2. The system worked with a white light source centred at 780 nm, and the spectral bandwidth was only 3 nm. The detection components employed a diffraction grating with 1800 lines/mm and a two-dimensional (2D) Charge-Coupled Device (CCD) array with 320 × 288 pixels. The depth profile of the measured cornea sample was obtained by Fast Fourier Transform (FFT), and the corneal thickness was therefore measured.

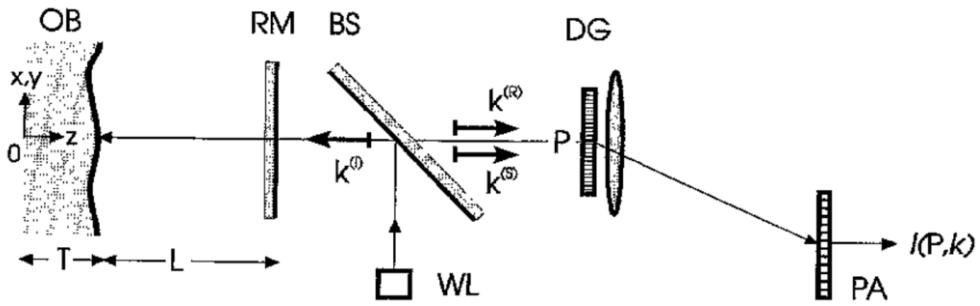

Figure 2.3 Schematic diagram of Fercher's OCT system. WL: white light source; BS: beamsplitter; RM: reference mirror; OB: object; DG: spectrometer diffraction grating; PA: photodiode array. (adapted from Fercher *et al*. [**25**])

In 1998, G. Häusler used a 'Spectral Radar' system to achieve *in vivo* measurement of human skin surface morphology [**26**]. He quantitively verified that skin sample containing melanomas backscatter at a higher intensity than normal skin samples. The system was driven by an SLD. The SLD had a central wavelength of 840 nm and a spectral bandwidth of 20 nm, which contributed to an axial resolution of 35 μm. Additionally, the achieved A-scan rate was approximately 10 Hz.

In 2002, Wojtkowski *et al*. applied an SD-OCT system to image the human retina for the first time [**27**]. The achieved lateral and axial resolutions are 30 μm and 15 μm, respectively, by using an objective lens with the Numerical Aperture (NA) of 0.42 and an SLD source emitting at 810 nm with a bandwidth of 20 nm. The system visualised the details of the macula and optic disk.

The use of supercontinuum lasers source to achieve ultrahigh axial resolution has been studied since 2011. Yadav *et al*. [**28**] demonstrated an SD-OCT with 1.1-μm axial resolution in tissues by using a Leukos supercontinuum source. Using an NKT supercontinuum lasers source, Cheung *et al*. [**29**] developed an SD-OCT with a constant axial resolution of 1.2 μm in varnish or paint throughout a detection range of 1.5 mm.

2.2 Principle and Imaging Mechanism of OCT

2.2.1 Principle of OCT

Low Coherence Length

OCT technique is based on LCI technique [**30–35**], which operates by the principle that two broad-band fields interfere only when the Optical Path Difference (OPD) of the two interferometer arms is within the coherence length of the low-coherence light source [**36–38**]. Thus, the coherence length determines the temporal width of the interferometric signal generated by the low-coherence interferometer and nominates the axial resolution of an OCT imaging system. There are many ways to define the coherence length, and the most commonly adopted metric in OCT is the product of the coherence time (determined by the low-coherence source) and the speed of light in vacuum. The reported study has discussed the limitations of assuming the shape of a source as the Gaussian profile, where it was concluded that the calculation of the coherence length from an assumed Gaussian spectrum might not be sufficiently reliable [**39**]. However, the Gaussian source assumption has been widely adopted in the OCT community, and the comparison work between this thesis and others is easy to be carried out. The Gaussian-shaped field spectrum and its corresponding intensity spectrum are used here. A normalised Gaussian source function is given as [**40**]:

$$S(k) = \frac{1}{\Delta k\sqrt{\pi}} \exp[-(\frac{k-k_0}{\Delta k})^2] \tag{2.1}$$

where $k = 2\pi/\lambda$ is known as the angular wave number used to describe the magnitude of the wave vector, Δk is the wave number bandwidth, and k_0 is the central wavenumber. The inverse Fourier transform of Eq. 2.1 represents the coherence function of the source, and it is also a Gaussian shape, which can be derived as

$$\Gamma(z) = \exp[-(z)^2 \Delta k^2] \tag{2.2}$$

Eq. 2.1 and Eq. 2.2 express the conversion from *k*-space to *z*-space. Further, the coherence length l_c can be written as [**41**]

$$l_c = \frac{4\ln(2)}{\pi}\frac{\lambda_0^{\,2}}{\Delta\lambda} \quad (z\text{-space})$$
$$l_c = \frac{4\sqrt{\ln(2)}}{\Delta k} \quad (k\text{-space}) \tag{2.3}$$

where λ_0 is the central wavelength of the light source and $\Delta\lambda$ is the spectral Full Width at Half Maximum (FWHM). To date, many types of light sources with advanced low-coherence properties have been used in developing OCT systems, where the popular light sources include SLD [**42**], broadband Light-Emitting Diode (LED) [**43**], thermal tungsten halogen lamp [**37**] and supercontinuum lasers [**44**]. The achieved coherence length spans the range from 1 µm to 20 µm. Particularly, supercontinuum lasers can be described as 'broad as a lamp, bright as a laser'. The developed supercontinuum lasers source can range from 400 nm to 2000 nm with a few watts of power. The use of supercontinuum lasers source to drive an OCT system can achieve therefore an ultrahigh axial resolution (such as less than 1 µm). However, the cost of such a source is normally over 20, 000 GBP.

Michelson Interferometer

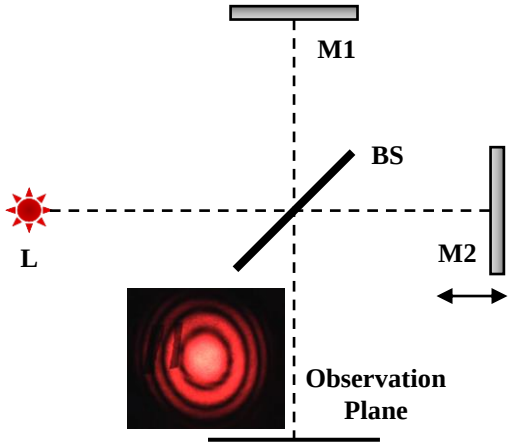

Figure 2.4 Schematic diagram of a Michelson interferometer. L – light source; M1, M2 – mirror; BS – beamsplitter; Insert – interference pattern (adapted from TSG Physics/Youtube)

Once the light source part is selected well, the main body of an OCT system can be aligned. The most appropriate method to fully understand the imaging mechanism of an OCT system is to inspect the Michelson interferometer in detail [**45–50**] since it is equipped as the core elements of a typical OCT system. A classic Michelson

interferometer consists of at least two mirrors utilised for two interferometer arms and a partially reflecting mirror known as beamsplitter. It enables the precise measurement of physical distance in terms of light wavelengths by counting the number of interference fringes when one of the mirrors moves. As shown in Fig. 2.4, the incident light is divided into two parts by the beamsplitter. The reflected beam propagates to the stationary mirror M1, and the transmitted beam travels to the movable mirror M2. The returning beam from M1 then passes straight through the beamsplitter to the observation plane, and the returning beam from M2 is then deflected by 90 degrees at the beamsplitter toward the observation plane. As demonstrated from the positions shown in Fig 2.1, M1 and M2 share the same length to the centre of the beamsplitter. When M2 is moved, and it generates an OPD between the two mirrors, denoted as Δz, it will lead to a phase change $\Delta\emptyset$, which can be expressed as

$$\Delta\phi = \frac{2\pi}{\lambda_0}\Delta z = k\Delta z \tag{2.4}$$

as a result, the observable constructive interference patterns when

$$\Delta\phi = m\pi \text{ or } \Delta z = m\frac{\lambda_0}{2}, \text{ (m = 0, } \pm 1, \pm 2, ...) \tag{2.5}$$

and destructive interference patterns when

$$\Delta\phi = (2m+1)\pi \text{ or } \Delta z = (m+\frac{1}{2})\lambda_0, \text{ (m = 0, } \pm 1, \pm 2, ...) \tag{2.6}$$

The insert of Fig. 2.4 shows a practical example generated by a Michelson interferometer. The relation revealed from Eq. 2.4 to Eq. 2.6 provide a clear understanding of the property of an interferogram.

OCT Configuration

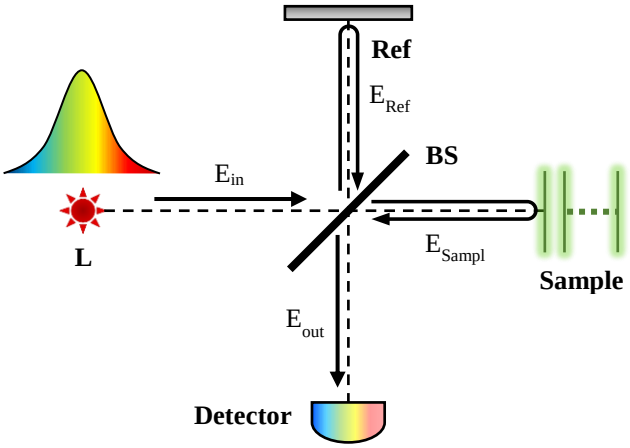

Figure 2.5 Schematic diagram of a Michelson interferometer used in an OCT system. L – low-coherence light source; Ref – reference mirror; BS – beamsplitter.

If the above Michelson interferometer is driven by a low-coherence source (broadband and Gaussian-shaped) and a sample with multi-layer structures is detected by a photosensitive detector, an OCT system is then determined. Figure 2.5 shows the schematic diagram of an OCT system, which employs the Michelson configuration. A common way to describe OCT mathematically is to introduce the electric field formula in the complex form as

$$E_{in}(k,\omega) = s(k,\omega)\exp[i(kz-\omega t)] \tag{2.7}$$

where the first term $s(k,\omega)$ is source field amplitude as a function of the angular wavenumber k and angular frequency ω, in which k is related to spatial frequency ξ, as $k = 2\pi\xi = 2\pi/\lambda$, and ω is related to the frequency of light ν, as $\omega = 2\pi\nu = 2\pi c/\lambda$ (c is the speed of light in vacuum). The second exponential term depicts the accumulated phase, which is related to the optical path z and time variation t [**51**]. For the reference arm, the electric filed reflectivity and power reflectivity of the reference mirror can be assumed and respectively denoted as r_{Ref} and $R_{Ref} = |r_{Ref}|^2$, and the optical path between the reference mirror and the beamsplitter is denoted as z_{Ref}. For the sample arm, by assuming negligible dispersion within the sample, the electric field reflectivity is the function with the optical path variable related to the distance from different reflectors within the sample to the beamsplitter, which can be expressed as

$$r_{Sampl}(z_{Sampl}) = \sum_{i=1}^{N} r_{Sampl\text{-ith}}\,\delta[z_{Sampl} - z_{Sampl\text{-ith}}] \tag{2.8}$$

where $r_{Sampl-i\text{th}}$ represents the reflectivity of the *i*th layer, it varies with refractive index change resulting from the layered structures of the sample. The Dirac delta function term points out the position of each layer. The power intensity from the *i*th layer can be written as $R_{Sampl-i\text{th}} = \left|r_{Sampl-i\text{th}}\right|^2$. Here, the beamsplitter is assumed to have an ideal power splitting rate of 0.5. The electric fields reach the beamsplitter after returning from the reference arm and sample arm can be written as

$$\begin{aligned} E_{Ref}(k,\omega) &= \frac{1}{2}E_{in}(k,\omega)r_{Ref}\,\exp[i(2kz_{Ref})] \\ &\quad and \\ E_{Sampl}(k,\omega) &= \frac{1}{2}E_{in}(k,\omega)\int r_{sampl}(z_{Sampl})dz_{Sampl} \\ &= \frac{1}{2}E_{in}(k,\omega)\sum_{i=1}^{N} r_{Sampl\text{-ith}}\,\exp[i(2kz_{Sampl\text{-ith}})] \end{aligned} \tag{2.9}$$

where, factor 2 in the exponential terms takes the consideration of the round-trip path length in both the reference and sample interferometer arms. Accordingly, the output electric field can be written as

$$E_{out}(k,\omega) = E_{Ref}(k,\omega) + E_{Sampl}(k,\omega) \tag{2.10}$$

Since the detector used in OCT systems is photoconductive, it detects light intensity which is proportional to the square of the output electric field as

$$I(k,\omega) \propto E_{out}(k,\omega)E_{out}^{*}(k,\omega) \tag{2.11}$$

where E_{Out}^{*} is the complex conjugate of E_{Out}. In practice, the angular frequency ω changes too fast for a detector to react. It records, therefore, the average value over the response time of the detector. The registered intensity can be expressed as

$$I(k) = \lim_{T\to\infty}\frac{1}{2T}\int_{-T}^{T} E_{out}(k)E_{out}^{*}(k)dt \tag{2.12}$$

By substituting Eq. 2.10 into Eq. 2.12, it can be found that the intensity consists of three terms as

$$I(k) = \left\langle E_{Ref}(k)E_{Ref}^{*}(k)\right\rangle + \left\langle E_{Sampl}(k)E_{Sampl}^{*}(k)\right\rangle + 2\Re\left\{\left\langle E_{Sampl}(k)E_{Ref}^{*}(k)\right\rangle\right\} \tag{2.13}$$

where, the angular brackets denote the integration of the time-average. Making relevant substitution from Eq. 2.7 to Eq. 2.9 and using the aforementioned source intensity function $S(k)$, the resultant OCT interferogram after simplifying the exponential terms by Euler's formula can be finally given as

$$I(k) = \frac{1}{4}\left[S(k)[R_{Ref} + \sum_{i=1}^{N} R_{Sampl-\text{ith}}] \right] + \frac{1}{4}\left[S(k) \sum_{i \neq j=1}^{N} \sqrt{R_{Sampl\text{-ith}} R_{Sampl\text{-jth}}} \cos[2k(z_{Sampl\text{-ith}} - z_{Sampl\text{-jth}})] \right] + \frac{1}{2}\left[S(k) \sum_{i=1}^{N} \sqrt{R_{Ref} R_{Sampl\text{-ith}}} \cos[2k(z_{Ref} - z_{Sampl\text{-ith}})] \right] \quad (2.14)$$

where the first term is commonly defined as the Direct Current (DC) component, which is dominated by the source spectrum and the reflectivities of the reference mirror and sample. The second term is defined as the auto-correlation component, which is dominated by the layered sample. It is also regarded as an artefact with an OCT system since it could affect OCT image quality when its corresponding intensity is comparable to the DC term. The last term known as the cross-correlation component depends on the OPDs between the reference mirror and sample's reflectors, and it carries the internal structure information of the sample. To reconstruct this term is the most important task in OCT signal and image processing work.

2.2.2 Time-Domain and Spectral-Domain OCT

To date, several OCT techniques have been presented including Polarization-Sensitive OCT [**52–56**], Swept-Source OCT [**57–61**], Doppler OCT [**62–65**], Differential Absorption OCT [**66–68**], Adaptive Optics OCT [**69–73**]. These reported OCT techniques can be broadly classified into two groups, namely TD-OCT and SD-OCT [**74**]. For a TD-OCT system, the interferogram from each reflector within a sample can be collected by displacing reference arm to achieve axial scanning over a distance that is equal to the depth position of the probing interface. In contrast to TD-OCT, the recorded spectral interferogram by an SD-OCT system takes all the depth information of the measured sample, and is therefore free of the axial scanning mechanism. The acquired time-domain or spectral-domain interferogram can be reconstructed to tomography signal.

TD-OCT Imaging Mechanism

Figure 2.3 shows the schematic diagram of a typical TD-OCT system. In this case, the probing beam from a broadband light source is split using a beamsplitter and reaches the reference mirror and the sample surface. The returning beams from the reference arm and the sample arm are recombined at the beamsplitter. Due to the low-coherence property of the light source, an interference signal can be obtained only when the OPD between the two interferometer arms is within the coherence length. By displacing the reference mirror with a motorised stage, the depth/axial scanning of the sample can be achieved. This enables the detection of the interference signal from any given interface within the sample. Intrinsically, this mechanism (conventional TD-OCT) is time-consuming for data acquisition.

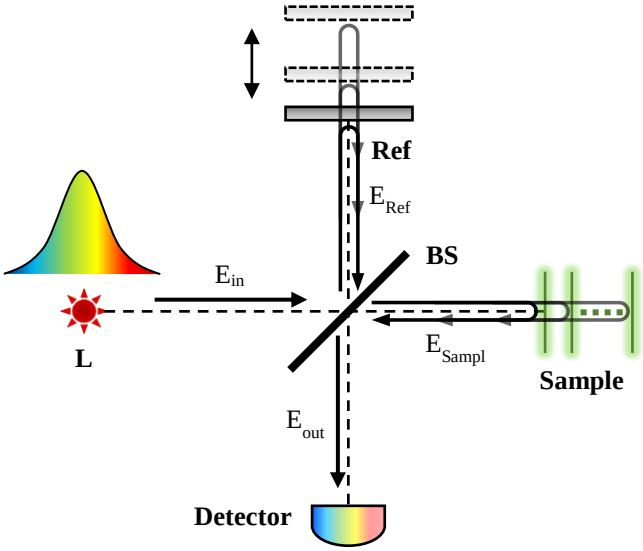

Figure 2.6 Schematic diagram of a Time-Domain OCT (TD-OCT) system.
L – low-coherence light source; Ref – reference mirror; BS – beamsplitter.

In a TD-OCT system, the interference intensity signal corresponding to a single-point measurement can be registered by using a single photodetector. The wavenumber-dependent intensity $I(k)$ shown in Eq. 2.14 can be mathematically described as a function of the reference arm delay z_{Ref}. The original A-scan signal can be then defined as the integration of Eq. 2.14 as [**40**]

$$I_{TD-OCT}(z_{Ref}) = \frac{1}{4} S_0 \left\{ \left[R_{Ref} + \sum_{i=1}^{N} R_{Sampl-\text{ith}} \right] + \right.$$
$$\left[\sum_{i \neq j=1}^{N} \sqrt{R_{Sampl\text{-ith}} R_{Sampl\text{-jth}}} \Gamma(z_{Sampl\text{-ith}} - z_{Sampl\text{-jth}})] \cos[2k_0 (z_{Sampl\text{-ith}} - z_{Sampl\text{-jth}})] \right] + \quad (2.15)$$
$$\left. 2 \left[\sum_{i=1}^{N} \sqrt{R_{Ref} R_{Sampl\text{-ith}}} \Gamma(z_{Ref} - z_{Sampl-\text{ith}}) \cos[2k_0 (z_{Ref} - z_{Sampl-\text{ith}})] \right] \right\}$$

where $S_0 = \int_0^\infty S(k) dk$ is the integrated spectrum power of the light source over the wavenumber k. In the brace, the first term represents the DC signal, which is contributed by the reference mirror and sample reflectivities. The second term is the auto-correlation signal resulted from the interference between the different reflectors within the sample. Since the auto-correlation signal is independent of the reference delay z_{Ref}, it can be regarded as an additional signal offset. The third term describes the cross-correlation signal between the reference mirror and multiple reflectors within the sample. In this term, the amplitude envelope is defined as the convolution between sample reflectivity and the source coherence function (used as axial Point Spread Function (PSF)), and it is modulated by the cosinusoidal carrier signal, the frequency of which is proportional to the central wavenumber k_0. Furthermore, the amplitude envelope signal can be demodulated to obtain $R_{Ref} R_{Sampl}$, which is the intensity of the A-scan signal. It is noticeable that the weak sample reflectivity R_{Sampl} has been amplified by the stronger reference reflectivity R_{Ref}.

SD-OCT Imaging Mechanism

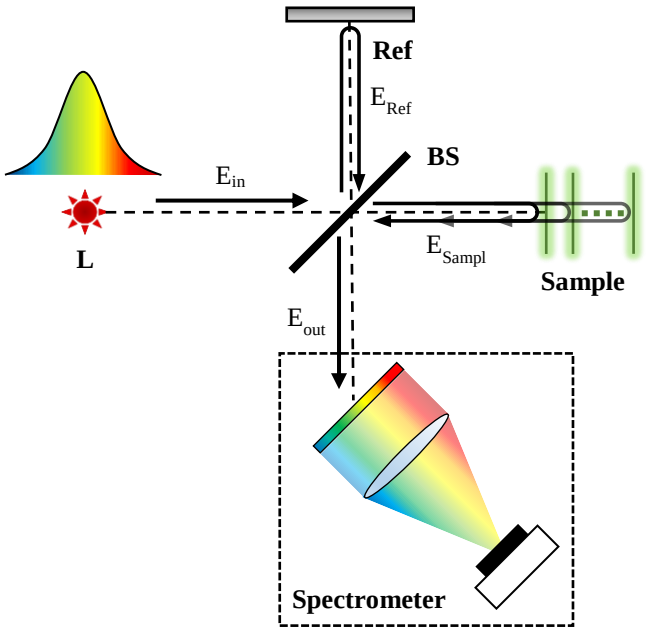

Figure 2.7 Schematic diagram of a Spectral-Domain OCT (SD-OCT) system. L – low-coherence light source; Ref – reference mirror; BS – beamsplitter.

Figure 2.7 shows the schematic diagram of a typical SD-OCT system. SD-OCT is based on the fact that each wavelength of the used low-coherence light source will interfere even if the OPD between the reference and sample arms is out of the coherence length determined by the source. Under such circumstances, the beamsplitter splits the incident beam to a fixed reference mirror and the sample. There is no moving part that is required to carry out a depth/axial scanning. The spectral interferogram is recorded by using a spectrometer device. Obviously, this mechanism is significantly faster than the TD-OCT since all the reflection/backscattering from different reflectors within the sample are acquired simultaneously.

In a spectrometer-based SD-OCT system, all spectral components of the interference signal corresponding to a single-point measurement are simultaneously detected by a linear detector array such as a One-Dimensional (1D) CCD. For the wavenumber-dependent interference signal $I_{SD-OCT}(k)$, the carrier signal frequency is related to the OPD between the two interferometer arms, and it will vary for the reflectors at different depths of the sample. Therefore, the Fourier transform of the interference signal will produce the internal profile of the sample, and this can be written as

$$I_{SD-OCT}(z) = \mathcal{F}^{-1}\{I_{SD-OCT}(k)\} = \frac{1}{8}\Gamma(z) \otimes \left\{ \left[R_{Ref} + \sum_{i=1}^{N} R_{Sampl-\text{ith}} \right] + \left[\sum_{i \neq j=1}^{N} \sqrt{R_{Sampl\text{-ith}} R_{Sampl\text{-jth}}}\, \delta[z \pm 2(z_{Sampl\text{-ith}} - z_{Sampl\text{-jth}})] \right] + 2\left[\sum_{i=1}^{N} \sqrt{R_{Ref} R_{Sampl\text{-ith}}}\, \delta[z \pm 2(z_{Ref} - z_{Sampl\text{-ith}})] \right] \right\} \quad (2.16)$$

where $\otimes$ denotes the convolution operator, $\pm$ denotes a pair of the conjugate path in z space due to the inverse Fourier transform, which determines a mirror A-scan signal along with the negative path direction. Similar to the TD-OCT, the first term in the brace is the DC intensity signal, and the second term is the auto-correlation intensity signal generated from the different reflectors within the layered sample. The auto-correlation signal here cannot be treated as a constant offset as TD-OCT. However, it can be noticed that the OPD within the layered sample are often much smaller than the OPD with the reference arm path length. The auto-correlation signal therefore in practice is hard to be observed, and it normally locates around the DC signal position (zero OPD). The third term in the brace is the cross-correlation intensity signal. It describes the reflectivity from each detected reflector modulated by the Dirac delta function at its corresponding depth as the OPD of $z_{Ref} - z_{Sampl-\text{ith}}$. In addition, all the terms in the brace are convolved with the coherence function of the source (used as PSF) to obtain the A-scan signal.

In OCT community, an A-scan signal is referring to one of the tomography signals (depth profile) of a measured sample, which can be obtained by axially scanning the sample in a TD-OCT or by performing inverse Fourier transform to the acquired spectral interferogram in an SD-OCT. Additionally, a B-scan image comprises a number of A-scan signals to form therefore the cross-sectional image of the measured sample, which can be achieved by laterally scanning the sample.

2.2.3 Comparison between Time-Domain OCT and Spectral-Domain OCT

Axial Resolution

The axial resolution in both TD-OCT and SD-OCT is dominated by the property of the light source. Eq. 2.3 provides the coherence length of a low-coherence source with the

Gaussian-shaped spectrum. The axial resolution is defined as half the coherence length, which can be written as

$$\delta z = \frac{l_c}{2} = \begin{matrix} \frac{2\ln(2)}{\pi}\frac{{\lambda_0}^2}{\Delta\lambda} \approx 0.44\ \frac{{\lambda_0}^2}{\Delta\lambda} & (z\text{-space}) \\ \frac{4\ln(2)}{\Delta k} \approx 2.77\frac{1}{\Delta k} & (k\text{-space}) \end{matrix} \tag{2.17}$$

Taking into account that the broadband sources used in OCT systems do not have Gaussian spectra, their achievable axial resolutions are determined by introducing the spectral shaping techniques [**75–77**]. An estimated axial resolution for a broadband source can be written as

$$\delta z = \begin{matrix} \frac{4\ln(2)}{\pi}\frac{\lambda_{\max}\lambda_{\min}}{\lambda_{\max}-\lambda_{\min}} & (z\text{-space}) \\ \frac{8\ln(2)}{k_{\max}-k_{\min}} & (k\text{-space}) \end{matrix} \tag{2.18}$$

where the indices max and min indicate the spectrum range of the light source. It can be observed that a higher central wavelength and broader bandwidth could contribute to a better axial resolution. However, the choice of light source parameters depends on the absorption and scattering properties of the studied samples. Despite that shorter central wavelengths delivers a higher axial resolution, increased scattering effects cannot be ignored, which could affect the penetration depth.

Lateral Resolution and Depth of Focus

The lateral resolution in both TD-OCT and SD-OCT is dominated entirely by the properties of the optics employed in the sample arm. Most of the OCT systems use the scanning beam to detect the inner structures of a studied sample, where the lateral scan resolution is dependent on the ability of the system to distinguish two consecutive light spots (similar to Rayleigh's criterion for Airy discs). Assuming the OCT imaging beam is a Gaussian beam, the lateral resolution can be defined as [**40**]

$$\delta x = \frac{4\lambda_0}{\pi}\frac{f}{d} \approx \frac{2\lambda_0}{\pi}\frac{1}{NA} \tag{2.19}$$

where f is the focal length of the objective lens and d is the $1/e^2$ Gaussian beam waist of the probing beam at the lens, $NA \approx d/2f$ is the NA determined by the utilised lens. It can be seen from Eq. 2.19 that a better lateral resolution can be achieved by using a higher NA to minimize the focal spot. However, the Depth of Focus (DOF) at the same time is compromised because of diffraction. The DOF which is quantified by the confocal parameter b can be defined as two times the Rayleigh range

$$b = 2z_{Rayleigh} = \frac{\pi \delta x^2}{\lambda_0} \tag{2.20}$$

where the Rayleigh range $z_{Rayleith}$ is the distance from the focal plane to the place where the beam diameter has increased by $\sqrt{2}$ times. It can be noticed that the imaging optics utilised in traditional SD-OCT systems are commonly devised with a large DOF to accommodate the entire range of the A-scan signal. This limits the possibility of using high-NA objectives to enhance lateral resolution.

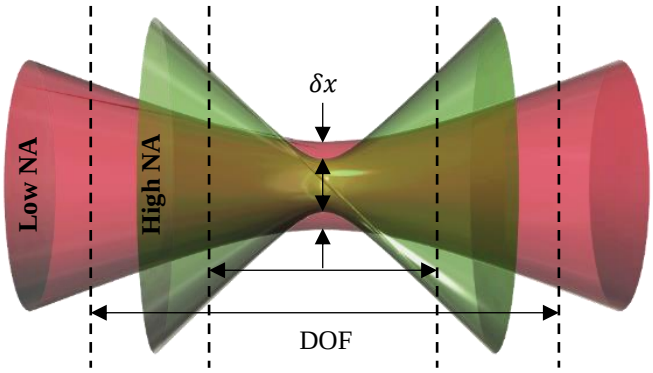

Figure 2.8 Relationship between high lateral resolution and high Depth of Focus (DOF). Red beam represents DOF achieved by using low Numerical Aperture (NA) objective; Green beam represents DOF achieved by using high-NA objective.

Imaging Depth

Without considering the optical attenuation that results from sample scattering and absorption effects and defocusing caused by the use of high-NA objective, the achievable imaging depth of a TD-OCT system is determined by the travel distance of the reference arm. In contrast to TD-OCT, the depth range can be probed by an SD-OCT system, that is dependent on the spectrometer performance (i.e. spectral resolution). Eq. 2.16 has demonstrated that the larger the OPD is between the two

interferometer arms, the higher the carrier signal frequency is. Thus, the maximum detectable depth relies on the resolvability of high-frequency spectra. Given that the maximum imaging depth is $z_{Sampl-Max}$, its correspondingly constructive interference period according to Eqs. 2.4–2.6 can be derived as

$$T = \frac{\pi}{n_{ave} z_{Sampl-Max}} \tag{2.21}$$

where n_{ave} represents the averaged refractive index of the sample. According to the Nyquist-Shannon sampling theorem, the spectrometer can be allowed to sample the interferogram with the sampling frequency that is over twice of the interference signals. In this case, the wavenumber resolution of the spectrometer δk is expected to be smaller than half of the interference period T, and the maximum imaging depth can be therefore written as

$$\begin{aligned} z_{Sampl-Max} &= \frac{\pi}{2 n_{ave} \delta k} \\ (\delta k &= \frac{k_{\max} - k_{\min}}{N_{pixel}}) \end{aligned} \tag{2.22}$$

where k_{max} and k_{min} are the maximum and minimum wavenumbers that can be probed by the used spectrometer, and N_{pixel} is the total pixel size of the line-array detector of the spectrometer. The resolution of the used spectrometer is commonly represented as the function of the wavelength, which is known as spectral resolution $\delta\lambda$. The relationship between the wavenumber resolution and spectral resolution can be expressed as

$$\begin{aligned} \delta k &= \frac{k_{\max} - k_{\min}}{N_{pixel}} \\ &= \frac{2\pi(\lambda_{\max} - \lambda_{\min})}{\lambda_{\max}\lambda_{\min} N_{pixel}} \approx \frac{2\pi}{{\lambda_0}^2}\delta\lambda \\ (\delta\lambda &= \frac{\lambda_{\max} - \lambda_{\min}}{N_{pixel}}) \end{aligned} \tag{2.23}$$

where λ_{max} and λ_{min} are the maximum and minimum wavelengths. By substituting Eq. 2.23 to Eq. 2.22, the achievable imaging depth of an SD-OCT can be written as

$$z_{Sampl-Max} = \frac{{\lambda_0}^2}{4n_{ave}\delta\lambda} \tag{2.24}$$

As highlighted from Eq. 2.24, a higher spectral resolution of a spectrometer enables better imaging depth.

Signal-to-Noise Ratio

In the OCT community, minimum detectable optical power compared to the power generated by a perfectly reflecting mirror can be used to represent the Signal-to-Noise Ratio (SNR) or the sensitivity of an OCT (SNR and sensitivity are often used interchangeably) [**40**]. It can be noticed that in both TD-OCT and SD-OCT (Eq. 2.15 and Eq. 2.16) the peak signal power of the cross-correlation term occurs at the zero OPD position of the two interferometer arms, which can be defined as

$$\mathcal{S}_{Sampl} = \frac{2\varepsilon^2 {q_e}^2}{{E_v}^2}\left[P_{Ref}P_{Sampl}\right] \tag{2.25}$$

where ε is the detector quantum efficiency, q_e is the electron charge, E_v is the photo quantum energy. P_{Ref} and P_{Sampl} are the optical powers related to the reference arm and the sample arm, and they are the product between the integrated source power and sample/reference power reflectivities. Shot noise describes the 'graininess' of low power measurements due to the quantisation of the light field and its interaction with electrons within the detector [**51**]. An OCT system is usually arranged to achieve shot-noise limited detection, in which the electric field in the reference arm is much higher than that in the sample arm. This indicates that the shot noise is dominated by the optical power of the reference arm. In this case, the shot noise power can be expressed as

$$\mathcal{N}_{shot} = \frac{2\varepsilon {q_e}^2}{E_v}P_{Ref} \tag{2.26}$$

In TD-OCT, the total shot noise power for measurement over the full spectral width is obtained by integration over the electronic detection bandwidth B, which can be expressed as

$$\mathcal{N}_{TD-OCT} = \mathcal{N}_{shot}B = \left(\frac{2\varepsilon {q_e}^2}{E_v}P_{Ref}\right)B \tag{2.27}$$

The SNR for a TD-OCT can be given as

$$SNR_{TD-OCT} = \frac{\mathcal{S}_{Sampl}}{\mathcal{N}_{TD-OCT}} = \frac{\varepsilon P_{Sampl}}{E_v B} \tag{2.28}$$

In SD-OCT, the electronic detection bandwidth is distributed over multiple spectral bands, which is achieved by a spectrometer. In this case, the detection bandwidth reduces correspondingly to the number of separately detected spectral bands M. The shot noise of SD-OCT can be then written as

$$\mathcal{N}_{SD-OCT} = \frac{\mathcal{N}_{TD-OCT}}{M} = \left(\frac{2\varepsilon {q_e}^2}{E_v} P_{Ref}\right)\left(\frac{B}{M}\right) \tag{2.29}$$

The acquisition time for a spectral element is inversely proportional to the detection bandwidth, denoted as $\tau = 1/2\mathrm{B}$. The total acquisition time τ_{Ascan} of an SD-OCT A-scan signal is the product of τ and M, and Eq. 2.29 can be rewritten as

$$\mathcal{N}_{SD-OCT} = \left(\frac{2\varepsilon {q_e}^2}{E_v} P_{Ref}\right)\left(\frac{1}{2\tau_{Ascan}}\right) \tag{2.30}$$

As discussed above that that the interference signal of an SD-OCT consists of real and complex parts after Fourier transform. Thus, the detected signal power is half the whole signal, and the SD-OCT SNR can be then expressed as

$$SNR_{SD-OCT} = \frac{\mathcal{S}_{Sampl}}{2\mathcal{N}_{SD-OCT}} = \frac{\varepsilon P_{Sampl}\tau_{Ascan}}{E_v} \tag{2.31}$$

From Eq. 2.28 and Eq. 2.31, the SNR difference between the TD-OCT and the SD-OCT can be deduced as

$$SNR_{SD-OCT} = \frac{M}{2} SNR_{TD-OCT} \tag{2.32}$$

This implies that an SD-OCT system is intrinsically more sensitive than a TD-OCT system by the factor of $M/2$. Note that the number of pixels M easily surpasses 1000 contributed from the current development of CCD or Metal–Oxide–Semiconductor (CMOS) detectors. This is in accordance with the fact that the SD-OCT collects the signals from multiple depths within the sample during the entire signal acquisition time [**78–80**].

2.3 Parallelization Imaging Scheme of OCT

2.3.2 Full-Field OCT Imaging Modality

Conventional TD-OCT is based on a single-point imaging mechanism, whereby both the lateral and axial scans need to be performed to obtain a B-scan image. There is a scheme that can achieve fast B-scan imaging: introducing a low NA objective lens to keep the confocal gate long enough to cover the full imaging range in the sample. This configuration avoids the need to translate the sample along its depth direction (z-direction). The A-scan signal corresponding to each lateral point can be obtained by modulating the optical path of the reference arm at high speed, and a B-scan image can then be obtained by scanning the sample along with the lateral position. However, the use of a low NA objective sacrifices the lateral resolution.

In 1998, Beaurepaire *et al*. demonstrated at first time the configuration of Full-Field Optical Coherence Microscopy (FF-OCM) [**81**]. The full field of view on the sample was irradiated using an infrared LED source centred at 840 nm with a spectral bandwidth of 31 nm. A 2D CCD array was used rather than a single-pixel photodiode for a traditional TD-OCT. The images from the *en-face* plane were recorded by lock-in detection and phase modulation techniques. The use of high-NA (0.25) microscope objectives achieved a lateral resolution of 2 μm, which was able to resolve the cells of an onion sample. The achieved axial resolution by the FF-OCM system was 8 μm, which was limited by the used source. Since the confocal gating was narrow due to the high-NA objectives, the sample could be scanned in depth to several hundred microns by moving the sample in the z-direction to create a 3D volumetric data.

The parallel imaging modality revealed by the time-domain FF-OCT significantly improves the acquisition speed. The analysis from the perspective of *en-face* view is similar to most standard medical imaging schemes. It has been therefore applied in non-invasive detections of biomedical samples, in which the sample structures can be interpreted from their B-scan (x-z cross-section) images, *en-face* (x-y cross-section) images and even full 3D datacubes. To date, a number of *ex vivo* and *in vivo* imaging studies using FF-OCT have been reported [**82–86**].

2.3.3 Line-Field OCT Imaging Modality

In 1998, the concept of axial-lateral parallel TD-OCT was demonstrated by Zeylikovich *et al* [**87**]. In the proposed system, a diffraction grating was installed in the reference arm with Littrow position (incident angle and diffraction angle are identical), and a cylindrical lens was used in the sample arm to achieve a line illumination. The diffraction grating introduced a continuous optical delay along the direction of grating dispersion, which produced a sample depth scan. The depth-lateral optical information generated by the light from the grating and the sample can be then captured using a 2D CCD array. Thus, the whole system was free of axial and lateral scanning.

It has been discussed that SD-OCT has the advantage in SNR over conventional TD-OCT. A high-quality OCT image can be guaranteed in the case of an SD-OCT even with low light levels and high detection speed. At the same time, it also allows for better penetration depth in the sample. Researchers have investigated developing Line-field SD-OCT, in which x-z cross-section image of the samples can be acquired in a single shot by a 2D CCD in contrast to the *en-face* images in a time-domain FF-OCT.

In 1999, Zuluaga and Kortum, for the first time, demonstrated a spectral-domain Line-Field OCT (LF-OCT) configuration [**88**]. This was accomplished by optical imaging of a line on the sample surface in the sample arm, which was placed onto the entrance slit of an imaging spectrograph coupled to an array detector. At the output of the spectrograph, the wavelength information encoded the depth-resolved remission of the sample, and the spatial direction encoded the imaged, lateral direction on the sample. By performing a Fourier transformation line by line along the wavelength direction, the spectrogram information was reconstructed to the OCT B-scan image. Thus, there were no moving parts required for generating 2D images as conventional SD-OCT. A technical sample was imaged in the study.

In 2005, Grajciar *et al*. developed the first LF-OCT system for *in vivo* measurement of the human eye, where the *in vivo* images of the anterior chamber, cornea and iris were recorded by the system [**89**]. Since 2006, many groups have reported their LF-OCT systems with improved performance for biomedical imaging and other promising applications [**90,91**].

2.4 Conclusion

This chapter has reviewed the development of TD-OCT and SD-OCT techniques. A systematic comparison has been made between the TD-OCT and SD-OCT from their corresponding system setups, imaging theories and performance metrics as axial resolution, lateral resolution, imaging depth and SNR. It is concluded that both of the two OCT imaging variants have unique advantages. TD-OCT is still popular due to system simplicity and straightforward operations. TD-OCT system allows using high-NA objectives to achieve ultrahigh lateral resolution (i.e. approximately 1 μm). SD-OCT has its intrinsic advantages at higher SNR and faster acquisition speed when compared with conventional TD-OCT. It is therefore very suited to be deployed for time-critical imaging tasks. In addition, the parallel OCT imaging strategies such as time-domain FF-OCT technique and spectral-domain LF-OCT technique have been elaborated. They enable the 3D OCT imaging with a single scan (*z*-axis scan in FF-OCT and *x*- / *y*- axis scan in LF-OCT) rather than raster scan required by a single-point OCT configuration. FF-OCT and LF-OCT are obtaining popularity in many application areas.

References

[1] A. Fercher, K. Mengedoht, and W. Werner, "Eye-length measurement by interferometry with partially coherent light," Optics Letters, vol. 13, no. 3, pp. 186-188, 1988.

[2] J. G. Fujimoto, M. E. Brezinski, G. J. Tearney, S. A. Boppart, B. Bouma, M. R. Hee, J. F. Southern, E. A. Swanson, "Optical biopsy and imaging using optical coherence tomography," Nature Medicine, vol. 1, no. 9, pp. 970-972, 1995.

[3] A. F. Fercher, "Optical coherence tomography," Journal of Biomedical Optics, vol. 1, no. 2, pp. 157-174, 1996.

[4] B. Bouma and G. Tearney, "Handbook of optical coherence tomography". Taylor & Francis, 2001.

[5] W. Drexler and J. G. Fujimoto, "Optical Coherence Tomography: Technology and Applications", Springer Publishing, 2008.

[6] F. H. Albee, "Studies in bone growth: triple calcium phosphate as a stimulus to osteogenesis," Annals of Surgery, vol. 71, no. 1, p. 32, 1920.

[7] I. G. Zubal, C. R. Harrell, E. O. Smith, Z. Rattner, G. Gindi, and P. B. Hoffer, "Computerized three-dimensional segmented human anatomy," Medical Physics, vol. 21, no. 2, pp. 299-302, 1994.

[8] D. H. Howry, G. Posakony, C. R. Cushman, and J. H. Holmes, "Three-dimensional and stereoscopic observation of body structures by ultrasound," Journal of Applied Physiology, vol. 9, no. 2, pp. 304-306, 1956.

[9] P. D. Gatehouse, J. Keegan, L. A. Crowe, S. Masood, R. H. Mohiaddin, K. F. Kreitner, D. N. Firmin, "Applications of phase-contrast flow and velocity imaging in cardiovascular MRI," European Radiology, vol. 15, no. 10, pp. 2172-2184, 2005.

[10] A. Carrillo, J. L. Duerk, J. S. Lewin, and D. L. Wilson, "Semiautomatic 3-D image registration as applied to interventional MRI liver cancer treatment," IEEE Transactions on Medical Imaging, vol. 19, no. 3, pp. 175-185, 2000.

[11] A. Fercher, "In vivo optical coherence tomography in ophthalmology," in Medical Optical Tomography: Functional Imaging and Monitoring, Bellingham, USA, 1993.

[12] E. A. Swanson, J. A. Izatt, M. R. Hee, D. Huang, C. Lin, J. Schuman, C. Puliafito, and J. G. Fujimoto, "In vivo retinal imaging by optical coherence tomography," Optics Letters, vol. 18, no. 21, pp. 1864-1866, 1993.

[13] A. F. Fercher, C. K. Hitzenberger, W. Drexler, G. Kamp, H. Sattmann, L. F. Schmetterer, I. Strasser, C. J. Unfried, "In-vivo dual-beam optical coherence tomography," in Microscopy, Holography, and Interferometry in Biomedicine, Budapest, Hungary, 1994.

[14] M. R. Hee, C. A. Puliafito, C. Wong, J. S. Duker, E. Reichel, J. S. Schuman, E. A. Swanson, and J. G. Fujimoto, "Optical coherence tomography of macular holes," Ophthalmology, vol. 102, no. 5, pp. 748-756, 1995.

[15] M. C. Savastano, B. Lumbroso, and M. Rispoli, "In vivo characterization of retinal vascularization morphology using optical coherence tomography angiography," Retina, vol. 35, no. 11, pp. 2196-2203, 2015.

[16] A. Shahlaee, W. A. Samara, J. Hsu, E. A. T. Say, M. A. Khan, J. Sridhar, B. K. Hong, C. L. Shields, and A. C. Ho, "In vivo assessment of macular vascular density in healthy human eyes using optical coherence tomography angiography," American Journal of Ophthalmology, vol. 165, pp. 39-46, 2016.

[17] G. Tearney, S. Boppart, B. Bouma, M. Brezinski, N. Weissman, J. Southern, and J. Fujimoto, "Scanning single-mode fiber optic catheter–endoscope for optical coherence tomography," Optics Letters, vol. 21, no. 7, pp. 543-545, 1996.

[18] O. Raffel, T. Akasaka, and I. Jang, "Cardiac optical coherence tomography," Heart, vol. 94, no. 9, pp. 1200-1210, 2008.

[19] P. Feyter and K. Nieman, "New coronary imaging techniques: what to expect?," Heart, vol. 87, no. 3, pp. 592, 2002.

[20] M. V. Sivak Jr, K. Kobayashi, J. A. Izatt, A. M. Rollins, R. Ung-Runyawee, A. Chak, R. C. Wong, G. A. Isenberg, and J. Willis, "High-resolution endoscopic

imaging of the GI tract using optical coherence tomography," Gastrointestinal Endoscopy, vol. 51, no. 4, pp. 474-479, 2000.

[21] P. A. Testoni and B. Mangiavillano, "Optical coherence tomography in detection of dysplasia and cancer of the gastrointestinal tract and bilio-pancreatic ductal system," World Journal of Gastroenterology: WJG, vol. 14, no. 42, p. 6444, 2008.

[22] D. Huang, E. A. Swanson, C. P. Lin, J. S. Schuman, W. G. Stinson,W. Chang, M. R. Hee, T. Flotte, K. Gregory, C. A. Puliafito, and J. G. Fujimoto, "Optical coherence tomography," Science, vol. 254, no. 5035, pp. 1178-1181, 1991.

[23] W. Drexler, U. Morgner, F. Kärtner, C. Pitris, S. Boppart, X. Li, E. Ippen, and J. Fujimoto, "In vivo ultrahigh-resolution optical coherence tomography," Optics Letters, vol. 24, no. 17, pp. 1221-1223, 1999.

[24] T. H. Ko, D. C. Adler, J. G. Fujimoto, D. Mamedov, V. Prokhorov, V. Shidlovski, and S. Yakubovich, "Ultrahigh resolution optical coherence tomography imaging with a broadband superluminescent diode light source," Optics Express, vol. 12, no. 10, pp. 2112-2119, 2004.

[25] A. F. Fercher, C. K. Hitzenberger, G. Kamp, and S. Y. El-Zaiat, "Measurement of intraocular distances by backscattering spectral interferometry," Optics Communications, vol. 117, no. 1-2, pp. 43-48, 1995.

[26] G. Hausler and M. W. Lindner, ""Coherence radar" and "spectral radar"-new tools for dermatological diagnosis," Journal of Biomedical Optics, vol. 3, no. 1, pp. 21-31, 1998.

[27] M. Wojtkowski, R. Leitgeb, A. Kowalczyk, T. Bajraszewski, and A. F. Fercher, "In vivo human retinal imaging by Fourier domain optical coherence tomography," Journal of Biomedical Optics, vol. 7, no. 3, pp. 457-464, 2002.

[28] R. Yadav, K.-S. Lee, J. P. Rolland, J. M. Zavislan, J. V. Aquavella, and G. Yoon, "Micrometer axial resolution OCT for corneal imaging," Biomedical Optics Express, vol. 2, no. 11, pp. 3037-3046, 2011.

[29] C. Cheung, M. Spring, and H. Liang, "Ultra-high resolution Fourier domain optical coherence tomography for old master paintings," Optics Express, vol. 23, no. 8, pp. 10145-10157, 2015.

[30] B. L. Danielson and C. Boisrobert, "Absolute optical ranging using low coherence interferometry," Applied Optics, vol. 30, no. 21, pp. 2975-2979, 1991.

[31] D. W. Robinson and G. T. Reid, Interferogram analysis, digital fringe pattern measurement techniques. CRC Press, 1993.

[32] J. Szydlo, H. Bleuler, R. Wälti, and R. Salathé, "High-speed measurements in optical low-coherence reflectometry," Measurement Science and Technology, vol. 9, no. 8, p. 1159, 1998.

[33] C. Palavicini, Y. Jaouën, G. Debarge, E. Kerrinckx, Y. Quiquempois, M. Douay, C. Lepers, A. F. Obaton, G. Melin, "Phase-sensitive optical low-coherence reflectometry technique applied to the characterization of photonic crystal fiber properties," Optics Letters, vol. 30, no. 4, pp. 361-363, 2005.

[34] N. Delachenal, R. Gianotti, R. Walti, H. Limberger, and R. Salathé, "Constant high-speed optical low-coherence reflectometry over 0.12 m scan range," Electronics Letters, vol. 33, no. 24, pp. 2059-2061, 1997.

[35] D. Coric, H. G. Limberger, and R. P. Salathé, "Distributed measurements of fiber birefringence and diametric load using optical low-coherence reflectometry and fiber gratings," Optics Express, vol. 14, no. 24, pp. 11804-11813, 2006.

[36] T. H. Ko, D. C. Adler, J. G. Fujimoto, D. Mamedov, V. Prokhorov, V. Shidlovski, S. Yakubovich, "Ultrahigh resolution optical coherence tomography imaging with a broadband superluminescent diode light source," Optics Express, vol. 12, no. 10, pp. 2112-2119, 2004.

[37] A. F. Fercher, C. K. Hitzenberger, M. Sticker, E. Moreno-Barriuso, R. Leitgeb, W. Drexler, H. Sattmann, "A thermal light source technique for optical coherence tomography," Optics Communications, vol. 185, no. 1-3, pp. 57-64, 2000.

[38] L. Goldberg and D. Mehuys, "High power superluminescent diode source," Electronics Letters, vol. 30, no. 20, pp. 1682-1684, 1994.

[39] C. Akcay, P. Parrein, and J. P. Rolland, "Estimation of longitudinal resolution in optical coherence imaging," Applied Optics, vol. 41, no. 25, pp. 5256-5262, 2002.

[40] W. Drexler and J. G. Fujimoto, Optical coherence tomography: technology and applications. Springer Science & Business Media, 2008.

[41] A. F. Fercher, W. Drexler, C. K. Hitzenberger, and T. Lasser, "Optical coherence tomography-principles and applications," Reports on Progress in Physics, vol. 66, no. 2, p. 239, 2003.

[42] T. H. Ko, D. C. Adler, J. G. Fujimoto, D. Mamedov, V. Prokhorov, V. Shidlovski, S. Yakubovich, "Ultrahigh resolution optical coherence tomography imaging with a broadband superluminescent diode light source," Optics Express, vol. 12, no. 10, pp. 2112-2119, 2004.

[43] J. Schmitt, S. Lee, and K. Yung, "An optical coherence microscope with enhanced resolving power in thick tissue," Optics Communications, vol. 142, no. 4-6, pp. 203-207, 1997.

[44] W. Yuan, J. Mavadia-Shukla, J. Xi, W. Liang, X. Yu, S. Yu, X. Li, "Optimal operational conditions for supercontinuum-based ultrahigh-resolution endoscopic OCT imaging," Optics Letters, vol. 41, no. 2, pp. 250-253, 2016.

[45] M. Ikram and G. Hussain, "Michelson interferometer for precision angle measurement," Applied Optics, vol. 38, no. 1, pp. 113-120, 1999.

[46] J. Lawall and E. Kessler, "Michelson interferometry with 10 pm accuracy," Review of Scientific Instruments, vol. 71, no. 7, pp. 2669-2676, 2000.

[47] R. Kashyap and B. Nayar, "An all single-mode fiber Michelson interferometer sensor," Journal of Lightwave Technology, vol. 1, no. 4, pp. 619-624, 1983.

[48] C. K. Hitzenberger, "Measurement of corneal thickness by low-coherence interferometry," Applied Optics, vol. 31, no. 31, pp. 6637-6642, 1992.

[49] O. Mokryy, V. Koshovyy, I. Romanyshyn, and R. Sharamaga, "Stabilized detection scheme of surface acoustic waves by Michelson interferometer," Optica Applicata, vol. 40, no. 2, 2010.

[50] R. Scholl and B. W. Liby, "Using a Michelson interferometer to measure coefficient of thermal expansion of copper," The Physics Teacher, vol. 47, no. 5, pp. 306-308, 2009.

[51] P. H. Tomlins and R. Wang, "Theory, developments and applications of optical coherence tomography," Journal of Physics D: Applied Physics, vol. 38, no. 15, p. 2519, 2005.

[52] J. F. De Boer, T. E. Milner, M. J. van Gemert, and J. S. Nelson, "Two-dimensional birefringence imaging in biological tissue by polarization-sensitive optical coherence tomography," Optics Letters, vol. 22, no. 12, pp. 934-936, 1997.

[53] A. Baumgartner, S. Dichtl, C. K. Hitzenberger, H. Sattmann, B. Robl, A. Moritz, A. F. Fercher, W. Sperr, "Polarization–sensitive optical coherence tomography of dental structures," Caries Research, vol. 34, no. 1, pp. 59-69, 2000.

[54] M. Pircher, E. Goetzinger, R. Leitgeb, and C. K. Hitzenberger, "Three dimensional polarization sensitive OCT of human skin in vivo," Optics Express, vol. 12, no. 14, pp. 3236-3244, 2004.

[55] J. F. De Boer and T. E. Milner, "Review of polarization sensitive optical coherence tomography and Stokes vector determination," Journal of Biomedical Optics, vol. 7, no. 3, pp. 359-372, 2002.

[56] J. F. De Boer, S. M. Srinivas, A. Malekafzali, Z. Chen, and J. S. Nelson, "Imaging thermally damaged tissue by polarization sensitive optical coherence tomography," Optics Express, vol. 3, no. 6, pp. 212-218, 1998.

[57] M. A. Choma, M. V. Sarunic, C. Yang, and J. A. Izatt, "Sensitivity advantage of swept source and Fourier domain optical coherence tomography," Optics Express, vol. 11, no. 18, pp. 2183-2189, 2003.

[58] M. Gora, K. Karnowski, M. Szkulmowski, B. J. Kaluzny, R. Huber, A. Kowalczyk, M. Wojtkowski, "Ultra high-speed swept source OCT imaging of the anterior segment of human eye at 200 kHz with adjustable imaging range," Optics Express, vol. 17, no. 17, pp. 14880-14894, 2009.

[59] R. Huber, M. Wojtkowski, J. G. Fujimoto, J. Jiang, and A. Cable, "Three-dimensional and C-mode OCT imaging with a compact, frequency swept laser source at 1300 nm," Optics Express, vol. 13, no. 26, pp. 10523-10538, 2005.

[60] M. V. Sarunic, S. Weinberg, and J. A. Izatt, "Full-field swept-source phase microscopy," Optics Letters, vol. 31, no. 10, pp. 1462-1464, 2006.

[61] C. Viehland, B. Keller, O. M. Carrasco-Zevallos, D. Nankivil, L. Shen, S. Mangalesh, A. N. Kuo, C. A. Toth, J. A. Izatt, "Enhanced volumetric visualization for real time 4D intraoperative ophthalmic swept-source OCT," Biomedical Optics Express, vol. 7, no. 5, pp. 1815-1829, 2016.

[62] J. A. Izatt, M. D. Kulkarni, S. Yazdanfar, J. K. Barton, and A. J. Welch, "In vivo bidirectional color Doppler flow imaging of picoliter blood volumes using optical coherence tomography," Optics Letters, vol. 22, no. 18, pp. 1439-1441, 1997.

[63] X. Li, T. H. Ko, and J. G. Fujimoto, "Intraluminal fiber-optic Doppler imaging catheter for structural and functional optical coherence tomography," Optics Letters, vol. 26, no. 23, pp. 1906-1908, 2001.

[64] V. X. Yang, S. J. Tang, M. L. Gordon, B. Qi, G. Gardiner, M. Cirocco, P. Kortan, G. B. Haber, G. Kandel, I. A. Vitkin, and B. C. Wilson, "Endoscopic Doppler optical coherence tomography in the human GI tract: initial experience," Gastrointestinal Endoscopy, vol. 61, no. 7, pp. 879-890, 2005.

[65] G. Liu and Z. Chen, "Advances in doppler oct," Chinese Optics Letters, vol. 11, no. 1, p. 011702, 2013.

[66] J. Schmitt, S. Xiang, and K. Yung, "Differential absorption imaging with optical coherence tomography," JOSA A, vol. 15, no. 9, pp. 2288-2296, 1998.

[67] M. Pircher, E. Götzinger, R. Leitgeb, A. F. Fercher, and C. K. Hitzenberger, "Measurement and imaging of water concentration in human cornea with differential absorption optical coherence tomography," Optics Express, vol. 11, no. 18, pp. 2190-2197, 2003.

[68] M. Wei, J. Qian, Q. Zhan, F. Cai, A. Gharibi, and S. He, "Differential absorption optical coherence tomography with strong absorption contrast agents of gold nanorods," Frontiers of Optoelectronics in China, vol. 2, no. 2, pp. 141-145, 2009.

[69] R. J. Zawadzki, S. M. Jones, S. S. Olivier, M. Zhao, B. A. Bower, J. A. Izatt, S. Choi, S. Laut, and J. S. Werner, "Adaptive-optics optical coherence tomography for high-resolution and high-speed 3D retinal in vivo imaging," Optics Express, vol. 13, no. 21, pp. 8532-8546, 2005.

[70] B. Hermann, E. J. Fernández, A. Unterhuber, H. Sattmann, A. F. Fercher, W. Drexler, P. M. Prieto, and P. Artal, "Adaptive-optics ultrahigh-resolution optical coherence tomography," Optics Letters, vol. 29, no. 18, pp. 2142-2144, 2004.

[71] D. Miller, O. Kocaoglu, Q. Wang, and S. Lee, "Adaptive optics and the eye (super resolution OCT)," Eye, vol. 25, no. 3, p. 321, 2011.

[72] G. Shi, Y. Dai, L. Wang, Z. Ding, X. Rao, and Y. Zhang, "Adaptive optics optical coherence tomography for retina imaging," Chinese Optics Letters, vol. 6, no. 6, pp. 424-425, 2008.

[73] M. Pircher and R. J. Zawadzki, "Review of adaptive optics OCT (AO-OCT): principles and applications for retinal imaging," Biomedical Optics Express, vol. 8, no. 5, pp. 2536-2562, 2017.

[74] W. Drexler, M. Liu, A. Kumar, T. Kamali, A. Unterhuber, and R. A. Leitgeb, "Optical coherence tomography today: speed, contrast, and multimodality," Journal of Biomedical Optics, vol. 19, no. 7, p. 071412, 2014.

[75] R. Tripathi, N. Nassif, J. S. Nelson, B. H. Park, and J. F. de Boer, "Spectral shaping for non-Gaussian source spectra in optical coherence tomography," Optics Letters, vol. 27, no. 6, pp. 406-408, 2002.

[76] J. Gong, B. Liu, Y. L. Kim, Y. Liu, X. Li, and V. Backman, "Optimal spectral reshaping for resolution improvement in optical coherence tomography," Optics Express, vol. 14, no. 13, pp. 5909-5915, 2006.

[77] A. C. Akcay, J. P. Rolland, and J. M. Eichenholz, "Spectral shaping to improve the point spread function in optical coherence tomography," Optics Letters, vol. 28, no. 20, pp. 1921-1923, 2003.

[78] R. Leitgeb, C. Hitzenberger, and A. F. Fercher, "Performance of fourier domain vs. time domain optical coherence tomography," Optics Express, vol. 11, no. 8, pp. 889-894, 2003.

[79] J. F. De Boer, B. Cense, B. H. Park, M. C. Pierce, G. J. Tearney, and B. E. Bouma, "Improved signal-to-noise ratio in spectral-domain compared with time-domain optical coherence tomography," Optics Letters, vol. 28, no. 21, pp. 2067-2069, 2003.

[80] M. A. Choma, M. V. Sarunic, C. Yang, and J. A. Izatt, "Sensitivity advantage of swept source and Fourier domain optical coherence tomography," Optics Express, vol. 11, no. 18, pp. 2183-2189, 2003.

[81] E. Beaurepaire, A. C. Boccara, M. Lebec, L. Blanchot, and H. Saint-James, "Full-field optical coherence microscopy," Optics Letters, vol. 23, no. 4, pp. 244-246, 1998.

[82] K. Grieve, M. Paques, A. Dubois, J. Sahel, C. Boccara, and J.-F. Le Gargasson, "Ocular tissue imaging using ultrahigh-resolution, full-field optical coherence tomography," Investigative Ophthalmology & Visual Science, vol. 45, no. 11, pp. 4126-4131, 2004.

[83] M. Jain, N. Narula, B. Salamoon, M. M. Shevchuk, A. Aggarwal, N. Altorki, B. Stiles, C. Boccara, and S. Mukherjee, "Full-field optical coherence tomography for the analysis of fresh unstained human lobectomy specimens," Journal of Pathology Informatics, vol. 4, 2013.

[84] W.-Y. Oh, B. Bouma, N. Iftimia, R. Yelin, and G. Tearney, "Spectrally-modulated full-field optical coherence microscopy for ultrahigh-resolution endoscopic imaging," Optics Express, vol. 14, no. 19, pp. 8675-8684, 2006.

[85] A. Latrive and A. C. Boccara, "In vivo and in situ cellular imaging full-field optical coherence tomography with a rigid endoscopic probe," Biomedical Optics Express, vol. 2, no. 10, pp. 2897-2904, 2011.

[86] M. Laubscher, M. Ducros, B. Karamata, T. Lasser, and R. Salathe, "Video-rate three-dimensional optical coherence tomography," Optics Express, vol. 10, no. 9, pp. 429-435, 2002.

[87] I. Zeylikovich, A. Gilerson, and R. Alfano, "Nonmechanical grating-generated scanning coherence microscopy," Optics Letters, vol. 23, no. 23, pp. 1797-1799, 1998.

[88] A. F. Zuluaga and R. Richards-Kortum, "Spatially resolved spectral interferometry for determination of subsurface structure," Optics Letters, vol. 24, no. 8, pp. 519-521, 1999.

[89] B. Grajciar, M. Pircher, A. F. Fercher, and R. A. Leitgeb, "Parallel Fourier domain optical coherence tomography for in vivo measurement of the human eye," Optics Express, vol. 13, no. 4, pp. 1131-1137, 2005.

[90] S. Lawman, Y. Dong, B. M. Williams, V. Romano, S. Kaye, S. P. Harding, C. Willoughby, Y. C. Shen, and Y. Zheng, "High resolution corneal and single pulse imaging with line field spectral domain optical coherence tomography," Optics Express, vol. 24, no. 11, pp. 12395-12405, 2016.

[91] S. Lawman, B. Williams, J. Zhang, Y.-C. Shen, and Y. Zheng, "Scan-less line field optical coherence tomography, with automatic image segmentation, as a measurement tool for automotive coatings," Applied Sciences, vol. 7, no. 4, p. 351, 2017.

Chapter 3 In-line Monitoring Pharmaceutical Coating Process

3.1 Introduction

In pharmaceutical manufacturing, film coating on solid oral dosage forms are performed as part of the secondary manufacturing process commonly associated with the production of final dosage forms. The film coating process is a widely used unit operation in the pharmaceutical industry for ensuring colour uniformity, light protection and taste masking of the final products. For advanced coatings such as active coatings and sustained release, they allow formulators to control the rate of drug release as a function of the environment, that is, the initial drug release kinetics should be aligned to the pH of the environment [**1–5**]. Coating can be performed either as a batch or continuous operation. Even though the latter is receiving increasing attention in development as part of continuous manufacturing, batch operations are more commonly used commercially. Depending on the size of the solid dosage forms, coatings are routinely performed inside a pan-coater or a fluid-bed apparatus. For example, small dosage forms such as granules, pellets and mini-tablets with a diameter 5 – 6 mm and less are typically coated inside a fluid-bed apparatus. Even though coating processes have been used for many decades, there are still remaining challenges in part due to the inherent complexity of the process itself. The process ultimately represents a complex interplay between three main physical phenomena: 1) system thermodynamics; 2) spray atomization; 3) mixing of dosage forms, where these phenomena, in turn, are influenced by the equipment design, operating parameters and properties of dosage forms [**6,7**].

A lack of scientific understanding of these complex interactions and how they impact product quality makes it difficult to produce coatings with exact thicknesses and densities, and with only small variations between batches. As the process for the dosage forms to receive coatings is stochastic in nature, the coating thickness of the final product inevitably will follow a distribution. The realistic aim of a successful coating operation is, therefore, to make this distribution as narrow as possible or minimise coating variation. Process understanding can be achieved by process modelling where advances have been made [**8–12**]. At the same time, developments in Process Analytical Technologies (PAT) have allowed measurements of the dosage forms

throughout the process to be acquired, not only useful for quality control, but also for understanding the physicochemical changes of the film during manufacturing. Many analytical techniques have been demonstrated to date for the assessment of the coatings on the dosage forms, and extensive reviews on the subject matter have been presented [**13,14**]. Optical Coherence Tomography (OCT) is fast gaining popularity as a non-destructive method for quantitative evaluation of pharmaceutical coatings, where Spectral-Domain OCT (SD-OCT) technique with its advantages such as high data acquisition rate, high axial and lateral resolutions and high Signal-to-Noise Ratio (SNR) has been developing towards a powerful coating imaging tool for both the off-line and in-line applications.

The first demonstration of SD-OCT's potential for coating analysis of pharmaceutical tablets was presented in 2009 [**15**]. In the study, tablets of different shapes and coating formulations were tested using a commercial SD-OCT and a Swept-Source OCT (SS-OCT) operating at 930 nm and 1325 nm, respectively. It was found that differences between the Refractive Index (RI) of the respective coating layers were the reason behind the contrast between interfaces, which was necessary for resolving the different coating layers. A penetration depth of approximately 500 µm was demonstrated, though this value would likely to change depending on the materials scattering and absorption properties at the wavelengths of the illumination source. Although the penetration depth may be increased with a longer wavelength source at 1325 nm, an improvement over the shorter wavelength source at 930 nm was found to be negligible. The advantage of a shorter wavelength source, however, is the increase in the achievable spatial and axial resolution, at 9 and 6.5 µm, respectively. The authors also highlighted the high data acquisition rates used, i.e. tomography signal (A-scan) acquisition rate of 5 kHz (cross-sectional (B-scan) imaging rate of 4 frames per second (fps)) and 16 kHz (B-scan rate of 25 fps) for the SD-OCT and the SS-OCT, respectively.

In order to better assess the applicability of SD-OCT, coatings in the thickness range between 10–140 µm were measured by an in-house SD-OCT and a commercial Terahertz Pulse Imaging (TPI) system [**16**]. Note that the thickness of the film coating applied to a tablet dosage form is usually between 20–100 µm. This work studied, therefore, enough tablet samples with differently typical thickness. The TPI technique is relatively well-established for pharmaceutical tablet coating analysis [**17–20**]. The reported in-house SD-OCT featured a white light source in the form of a halogen lamp

and a broadband Charge-Coupled Device (CCD) based spectrometer in order to ensure good axial resolution and SNR. By actuating the reference beam repetitively, the phase-shifting method was implemented to increase measurement sensitivity. To ensure a comparable spot size to TPI, a multi-mode fibre with a diameter of 200 µm was used to collect the back reflected reference and sample beam. By comparing SD-OCT and TPI measurements, the study found that the two techniques are complementary from a coating thickness measurement perspective, where SD-OCT is suitable for coatings 10-60 µm, while TPI is suitable for 40 µm and above for the particular coating materials used. The relevant studies based on the combined sensors ("TPI + OCT") has further advanced in quantifying coating thickness and inter- and intra-tablet coating uniformity [**21,22**].

Coating variations between tablets were investigated for the first time by Koller *et al* [**23**], where a commercial SD-OCT system operating at 820 nm was used to characterise pharmaceutical tablet coatings sampled at 15 different stages of a tablet coating process (i.e. during heating, coating, drying and cooling) and with a coating thickness from uncoated to a target thickness of approximately 70 µm. Three-Dimensional (3D) visualisation of tablet coating was additionally presented to further demonstrate the potential use of SD-OCT as a diagnostic tool during and after tablet production.

Furthermore, the feasibility of using SD-OCT as an in-line quality control tool for tablet coating process had been investigated [**22**,**24**], where an SD-OCT system operating at a centre wavelength of 830 nm was used. As part of the pilot study, the OCT sensor head was mounted onto an *x-y* stage in order to traverse across a static tablet bed at speeds up to 0.7 ms^{-1} in order to simulate an ideal in-process measurement condition. Even though there was a loss in spatial resolution due to the broadening in the optical beam spot at high traversal speeds, the pilot study with a read-out rate of approximately 28 kHz demonstrated the potential of extracting both the inter-tablet and intra-tablet coating uniformity.

In a similar manner, an SD-OCT system was demonstrated to measure pellet coating thickness and coating uniformity inside a lab-scale fluid-bed coating process [**25**]. Measurement, in this case, was acquired through the viewing window where dispersion had to be compensated at the reference arm of the system. Even coating thickness of individual pellets had to be calculated manually from the in-line acquired OCT B-scan

images, coating thickness growth and both intra-, and inter-pellet coating uniformity could be resolved and validated against off-line OCT and particle analyser measurements.

Even though the previous studies have demonstrated promising results, there is still work to be conducted toward real-world application, i.e. 1) coating imaging limitation and 2) in-line monitoring through a fluid-bed device. For the former one, to date, only a few coating formulations have been studied and there is very little information on the applicability of in the literature to other coatings. As it is well documented that optical methods including OCT are prone to scattering effects leading to limited penetration depth, some pharmaceutical coatings may not be measured by this technique. For the latter field, to my best knowledge, so far only one paper has presented the in-line monitoring of the pellet coating process through a fluid-bed device. It should be noted that the sensor head used in an in-line OCT cannot run an internal scanning procedure, such as galvanometer mirrors, which are commonly used to acquire Two-Dimensional (2D) or 3D images of static objects. In-line OCT configurations utilise the movement of the sample (or of the sensor head) and continuously acquired A-scan signals. The successive A-scan signals then yielded B-scans images of the moving sample. This, therefore, requires a high acquisition rate of an SD-OCT sensor, especially for the small pellet (diameter is approximately 1 mm) application.

In this chapter, a single-point SD-OCT system is proposed, which is built up by using a customised light source. In contrast to the previously reported SD-OCT systems in the application where expensive SLDs or supercontinuum lasers (i.e. > £5k) were used [**23**–**25**], the customised source reduces both the cost and weight of the whole SD-OCT system, thus enabling the compactness and portability. On the other hand, the proposed SD-OCT uses an adjustable fibre coupler collimator as the sensor head, which allows the suitability for multiple types of coaters. By using the SD-OCT system, 22 different common coatings were measured to examine the transparency of a range of coating formulation which enables the assessment of the SD-OCT (typically centred at 840 nm) applicability. Moreover, a pilot-scale (3 kg) pellet coating process was monitored by the SD-OCT with BOSCH Solidlab 2 fluid-bed coater (provided by Bosch Hüttlin GmbH). The potential of the SD-OCT was demonstrated with the in-line experiment.

3.2 Development of A Single-point SD-OCT

3.2.1 Customised Light Source based on SLD

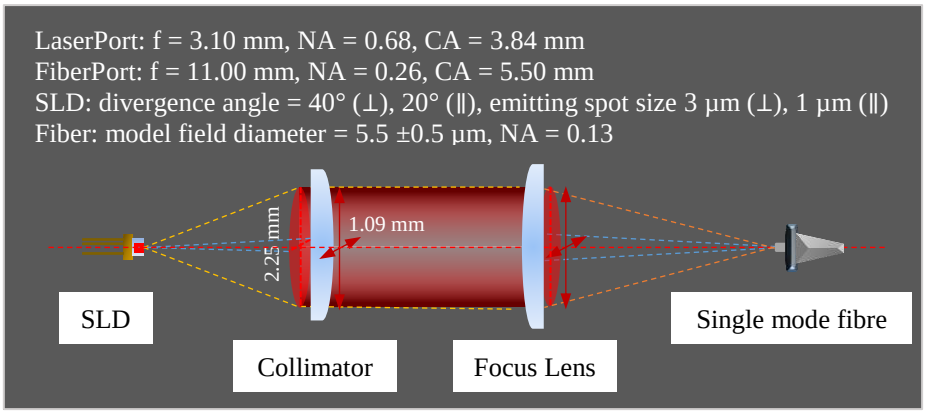

Figure 3.1 Cost-effective light source design based on a Superluminescent Diode (SLD) and infrared light focusing and collection components. The achieved coupling efficiency by the design is 44%. The collimated beam dimension is an elliptical pattern with its size of 2.25 mm vertically and 1.09 mm horizontally. The emitting spot sizes of the SLD are 3 µm and 1 µm in vertical and horizontal directions compared with the focused spot of 5.2 µm and 10.8 µm.

Figure 3.1 shows the schematic of the customised light source. An SLD (EXS210040-01, EXALOS) centred at a wavelength of 840 nm with a Full Width at Half Maximum (FWHM) bandwidth of 50 nm was used as the illumination source. The working power of the SLD is 5 mW. The divergence angles of the SLD are 40 and 20 degrees in vertical and horizontal directions, respectively. This results in an elliptical beam pattern after the emitting light is collimated by an aspherical lens (focal length: 3.1 mm; Numerical Aperture (NA): 0.68). The SLD can be connected to a laser diode mount (SR9B, Thorlabs) and driven by a Light-Emitting Diode (LED) driver (LEDD1B, Thorlabs) in CW mode. The paralleled beam is then focused by another aspherical lens (A220TM-B, Thorlabs) into a fibre coupler (TW850R5F2, Thorlabs), where the single-mode fibre has a mode field diameter of 5 ± 0.5 µm. The focused spot size was calculated as 5.2 µm and 10.8 µm in vertical and horizontal directions, respectively. This led to a coupling efficiency of about 44%. However, the incident power on the pharmaceutical coatings is approximately 1 mW (depending on coating material), which can still guarantee a good imaging performance in practical applications, such as an A-scan rate of 45 kHz. The total cost of the customised light source unit is approximately £800, and

this can be compared with the commercial SLD light sources (> £5k) and supercontinuum light sources (> £10k) often used in the application.

3.2.2 Experimental Setup

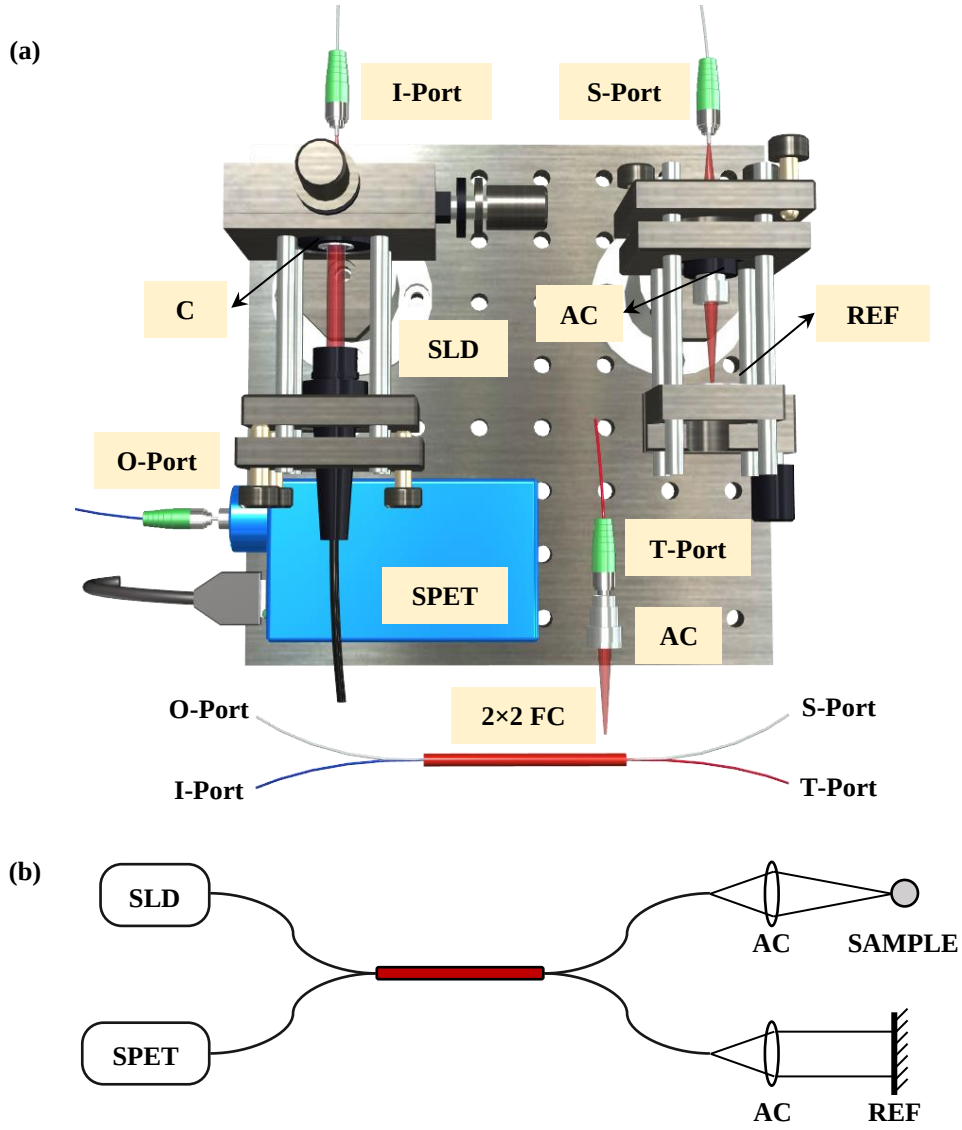

Figure 3.2 The developed Spectral-Domain Optical Coherence Tomography (SD-OCT) imaging system (a) prototype design and (b) system schematic diagram. SLD – superluminescent diode; C – collimator; AC – adjustable collimator; REF – reference mirror; SPET – spectrometer; 2×2 FC – 2 × 2 wideband single mode fiber coupler (50:50): I-port – input port connected with light source part; S-port – signal port connected with reference arm; T-port – tap port connected with sample arm; O-port – output port connected with spectrometer. For the 50:50 coupler, the signal and the tap ports have the same output power.

Figure 3.2 shows the in-house fibre-optic-based SD-OCT system, which was developed for pharmaceutical film coating applications. The system was arranged on a 200 mm × 200 mm optical breadboard (MB2020/M, Thorlabs). As shown in Fig. 3.2, the collimated light from the customised light source was first coupled into the input port of a 2 × 2 wideband single mode fibre couplers. The light beam was subsequently split (50:50) into a reference and a probe beam arriving at the signal port and tap port of the coupler, respectively. The reference beam was focused onto a reference mirror using an adjustable collimator (CFC-2X-B, Thorlabs), and the probe beam was focused onto the measured sample surface by using another identical adjustable collimator. The backscattered probe beam interfered with the reflected reference beam at the output port of the fibre coupler. The interferogram was collected by using a high-resolution spectrometer (Cobra SRC, Wasatch Photonics), which employs a linear array CCD camera with 2048 pixels.

3.2.3 Imaging Performance

As aforementioned, the spectral FWHM (50 nm) and centre wavelength (840 nm) determine the theoretical axial resolution, which is calculated as 6.2 μm according to Eq. 2.17. In practice, the axial resolution is determined by the FWHM of the main peak in an A-scan signal. Figure 3.3(a) shows one of the A-scan when placing a silver mirror (as the sample). The highest peak at zero Optical Path Difference (OPD) position represents the DC signal. The following two peaks that are symmetrical to the zero OPD position represent the interference signal intensity of the measured mirror sample. The FWHM of them represents the achieved axial resolution in air, which was measured as 9 μm. The lateral resolution of the SD-OCT was determined by raster scanning of a positive resolution target USAF 1951 (Thorlabs). Figure 3.3(b) shows the *en-face* image of the scanned resolution target sample. As a result, the element 5 in group 5 of the target was resolved, corresponding to the lateral resolution of 19.6 μm. In addition, the achieved SNR of the system was measured as 76 dB.

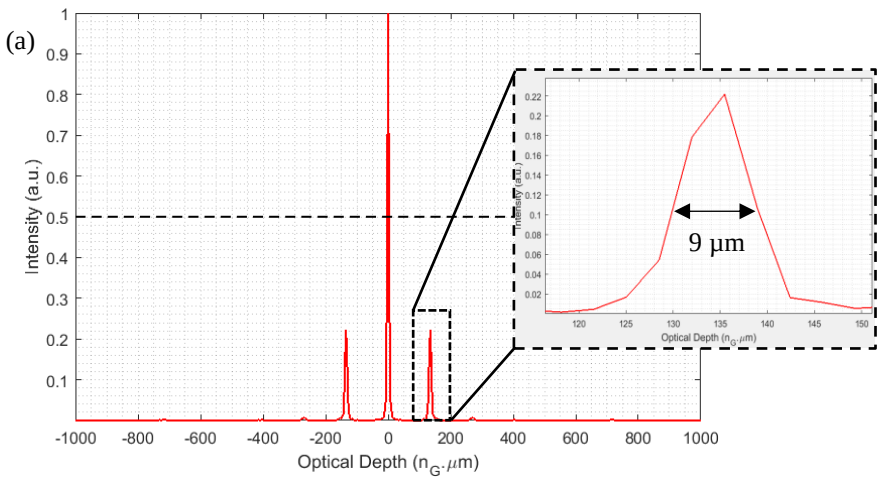

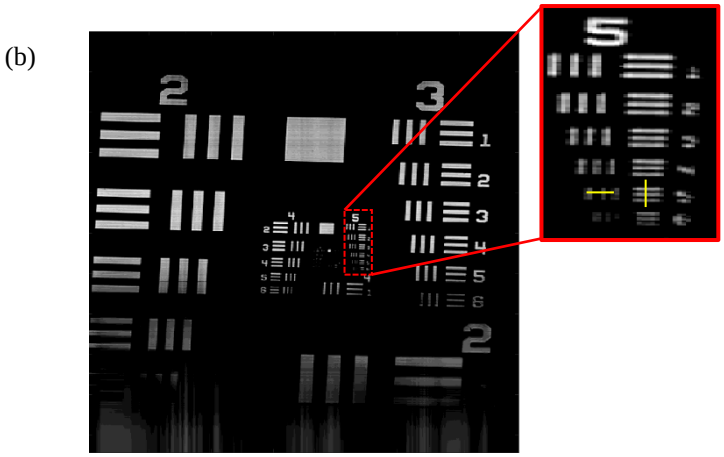

Element	Group Number									
	-2	-1	0	1	2	3	4	5	6	7
1	0.250	0.500	1.00	2.00	4.00	8.00	16.00	32.00	64.00	128.00
2	0.280	0.561	1.12	2.24	4.49	8.98	17.95	36.0	71.8	144.0
3	0.315	0.630	1.26	2.52	5.04	10.10	20.16	40.3	80.6	161.0
4	0.353	0.707	1.41	2.83	5.66	11.30	22.62	45.3	90.5	181.0
5	0.397	0.793	1.59	3.17	6.35	12.70	25.39	50.8	102.0	203.0
6	0.445	0.891	1.78	3.56	7.13	14.30	28.50	57.0	114.0	228.0

Values are in lp/mm.

Figure 3.3 Axial and lateral resolution of the SD-OCT system. (a) Tomography signal (A-scan) of a mirror sample where the Full Width at Half Maximum (FWHM) measured from the A-scan signal is 9 µm (insert figure in a) as the axial resolution. (b) Measured USAF 1951 resolution target sample for determination of lateral resolution. The zoom-in image indicates the achieved resolution by the system, where the lines in group 5 element 5 (yellow lines indicated) are resolvable with the naked eye. The chart below lists the number of line pairs per millimetre (lp/mm) for a given element within a group (adapted from Thorlabs website), and the lateral resolution can be determined as 19.6 µm.

3.3 Material

3.3.1 Tablet Sample Used for SD-OCT Imaging Feasibility Study

The tablet samples used in this study were provided by Colorcon Ltd. (Dartford, UK), which comprised 22 tablets chosen from 22 different batches, where a different coating formulation was used for each of the batches. The coating product name, the corresponding alias used in this study and the photographs of the coated tablets are shown in Table 3.1. Coating materials were applied to bi-convex shaped tablet cores that contained 50% lactose monohydrate and 50% microcrystalline cellulose. Film coating was then performed with a 15" fully perforated Labcoat IIX (O'Hara Technologies Inc., Canada) equipped with one spray nozzle (970 Düsen-Schlick GmbH, Untersiemau, Germany). The pan coater dimensions were 380 mm in diameter and had a full volume of 4.5 L enabling a batch size of 500 g. The average thickness, diameter and weight of the tablet cores (n=6) were 4.079 ± 0.018 mm, 10.069 ± 0.005 mm and 321 ± 3 g, respectively. To facilitate subsequent measurement comparisons, one side of each of the tablet was annotated by a scratch mark to serve as a datum. Film coating thickness was then estimated by measuring the physical dimensions of coated tablets with a micrometre gauge and subtracting it away from the average core thickness.

3.3.2 Pellet Sample Used for In-line Coating PAT Study

The pellet samples that are used for the PAT study with the SD-OCT system were provided by Hüttlin GmbH, BOSCH (the detailed formulation of the pellet coating have not been permitted to be published). To determine coating material transparency with the SD-OCT, off-line studies were performed before the in-line measurement. The measured pellets alias and their corresponding B-scan images are shown in Table 3.2. As a result, the coating 3 and the coating 6 used for Nicardipine and 14-64-V4 Homni pellets are resolved by the SD-OCT. The coating 6, which is composed of Kollicott SR 30D, Kollicoat IR, propylene glycol and diluent water, is selected for the in-line measurement. Additionally, the pellet core used in the study had a diameter of 1.2 mm; the lactose monohydrate is the main component.

Table 3.1 Images of the tablets coated with the respective coating product and the corresponding alias.

	Product ID			**Product ID**			**Product ID**	
Coating 1	03F190003 (opadry)		Coating 9	03F220071		Coating 17	114F210058	
Coating 2	20A29015 (opadry)		Coating 10	33G200004		Coating 18	114F250049	
Coating 3	31F29070 (opadry II)		Coating 11	03B205020 (opadry)		Coating 19	200F220052	
Coating 4	45F29058 (opadry II)		Coating 12	03F205017		Coating 20	493Z240008	
Coating 5	02A240002 (opadry)		Coating 13	85F205105		Coating 21	TC-117-205006	
Coating 6	02B220014		Coating 14	85G200008		Coating 22	TC-116-205001	
Coating 7	85F190000 (opadry II)		Coating 15	88A210007 (opadry amb II)				
Coating 8	70W29079 (opadry ns-g)		Coating 16	112A210011				

Table 3.2 Off-line cross-sectional (B-scan) imaging of coated pellet to investigate the suited coating material for in-line measurement with the Spectral-Domain Optical Coherence Tomography (SD-OCT)

	Product ID	**B-scan Image**
Coating 1	15-16-V10 Omeprazole DL coating	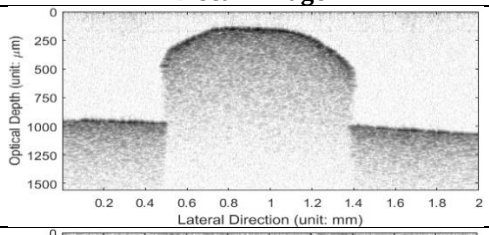
Coating 2	15-65-V1	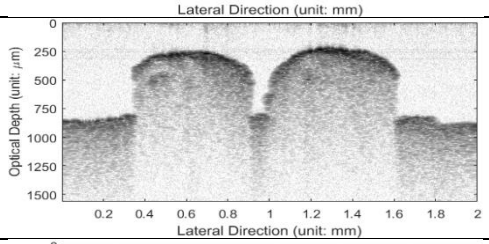
Coating 3	Nicardipine	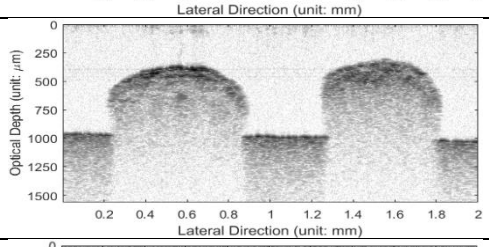
Coating 4	Lypron Substrates	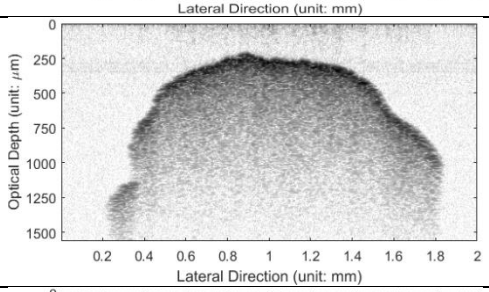
Coating 5	15-43-V1 Metoprolol Pellets (substrates)	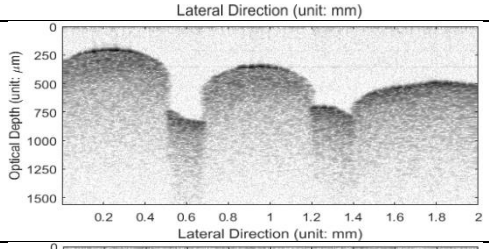
Coating 6	14-64-V4 Homni	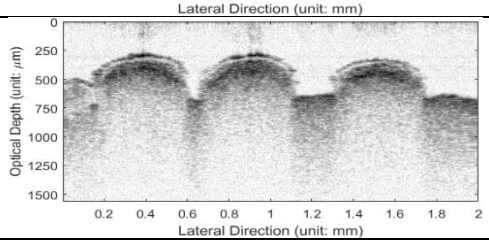

3.4 Investigation of Applicable Coating Formulation for SD-OCT Imaging

Figure 3.4 shows the acquired B-scan images of the tablets coated with the 22 coatings investigated in this study. Evidently, the coating/core interface for the coatings 1, 2, 7, 8, 13 and 18 can be visibly observed. The level of contrast between the air/coating and coating/core interface in the coatings 1, 4 and 13 may be enhanced with denoising techniques previously introduced [**21**]. In order to better isolate the causes behind OCT opaqueness at 840 nm, the coating compositions, the estimated coating thickness and the OCT transparency are listed in Table 3.3 for the respective coatings.

In this study, all of the analysed coating layers are greater than the OCT resolution limit (>9 µm). It can be seen that in compositions where there are no pigments or colourants, generally the coating/core interface can be clearly identified, with the exceptions to the coatings 3 and 4. The only difference between coatings 1 and 3 is the additional lactose and polydextrose in the coating formulation, which may have caused pronounced scattering effects and/or reduces the RI difference between the tablet core and coating as the core also contains 50% lactose monohydrate. This would, in turn, reduce the signal intensity reflecting from the coating/core interface resulting in no clear discrimination of the coating/core interface. It should be noted here that clear discrimination of the coating/core interface underpins automatic coating thickness quantification [**21,26**].

Assuming little or no absorption of the optical beam in the polymer binder material [**27**], for compositions containing pigments, in particular, titanium dioxide, the coating/core interface is generally not visible at all. This is because of the pigment particle size and a relatively high value of the effective RI that in turn, increases reflection at the air/coating interface meaning that only a fraction of incidence beam can actually penetrate into the coating [**27**]. As the beam travels through the coating results, more scattering is encountered leading to an attenuated signal for measurement.

The penetration depth in principle could be increased with an illumination source operating at a longer wavelength (i.e. 1300 or 1550 nm), but the improvement may not always be significant [**15**]. The advantage of working with a shorter wavelength source, on the other hand, is the improvement in the lateral and axial resolutions that is useful for studying coating uniformity [**15, 23**]. The effect of scattering for yellow iron oxide

compared to titanium dioxide is generally weaker at near-infrared wavelengths [**28**]. Despite this, coating 9 is still opaque to OCT because of the gradual change in RI encountered as the result of the coating dispersion penetrating into the core material during the coating operation [**29,30**].

Additionally, 3% weight gain red coating (coating 18) is transparent to OCT largely due to a comparatively larger contrast between the coating and tablet core RI in spite of the increased air/coating reflection from the similar coloured coating and the incident beam [**31**]. For another red coating (coating 20), the coating/core interface is not visible at all due to the titanium dioxide used in a comparatively thicker coating layer (10% weight gain). Finally, it is interesting to note that where the coating contains only talc and dye in the colourant as in the case of coating 13, the coating/core interface is marginally visible.

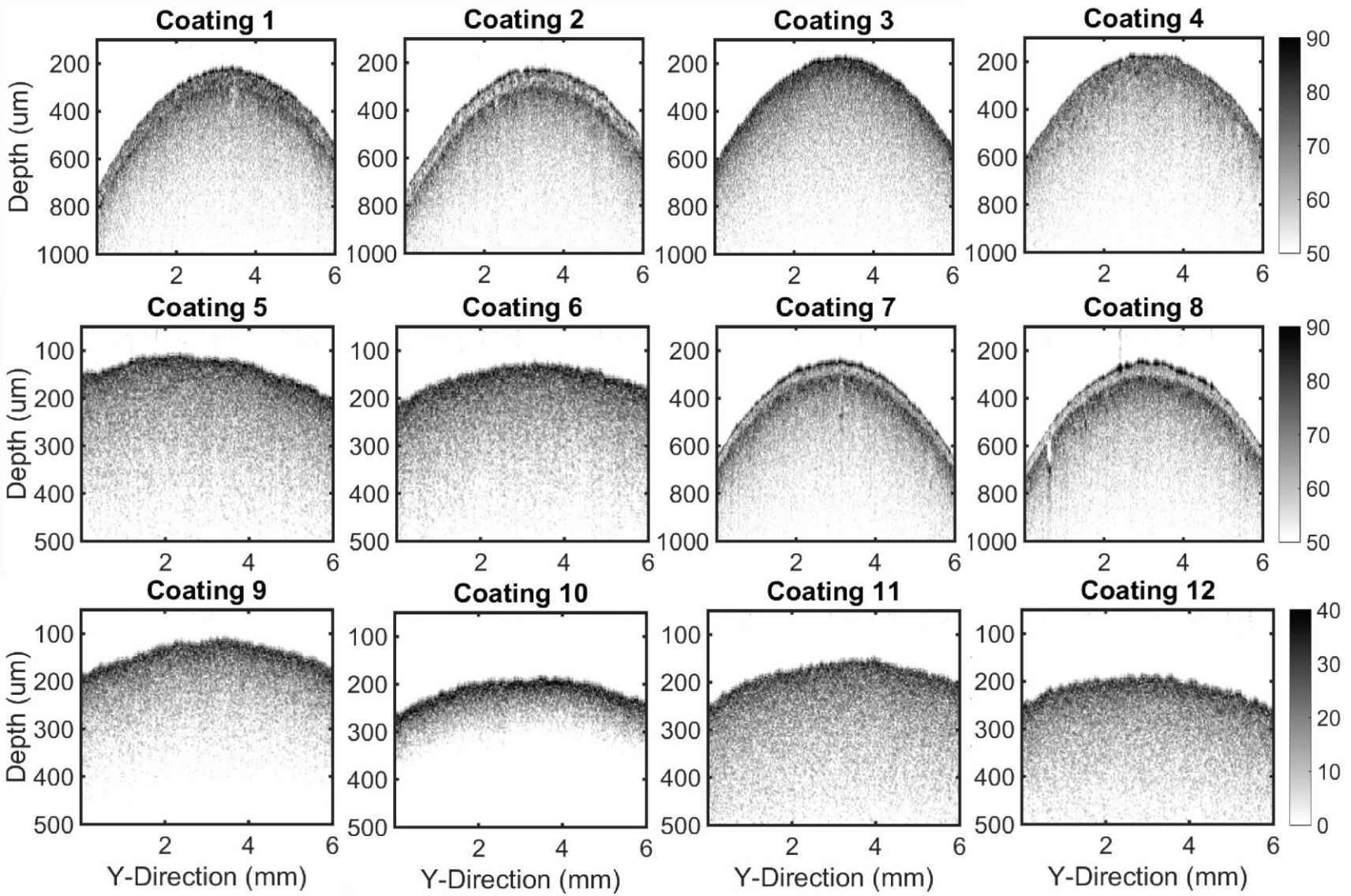
Coating 1
Coating 2
Coating 3
Coating 4
Coating 5
Coating 6
Coating 7
Coating 8
Coating 9
Coating 10
Coating 11
Coating 12
Depth (um)
Y-Direction (mm)

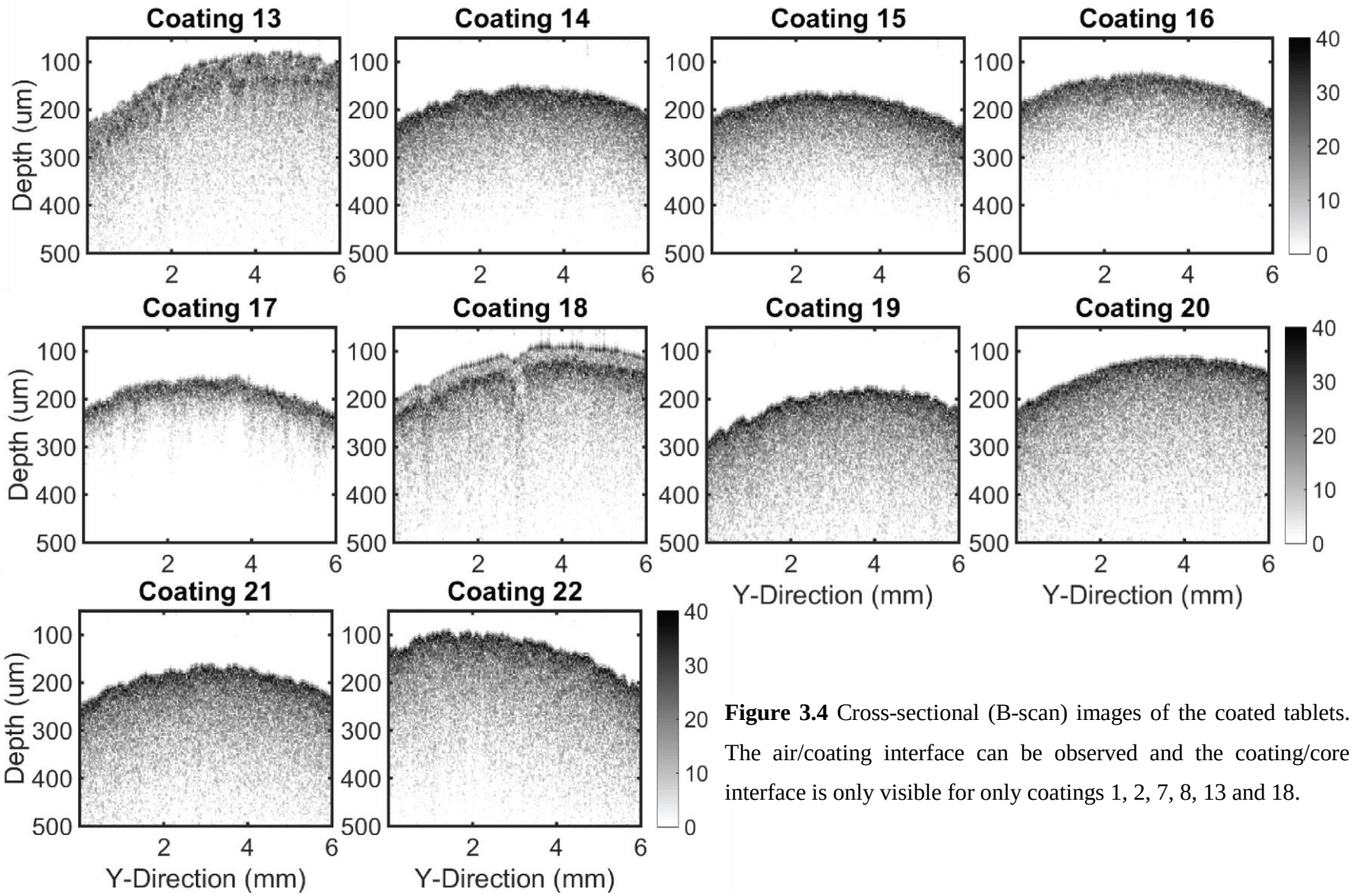

Figure 3.4 Cross-sectional (B-scan) images of the coated tablets. The air/coating interface can be observed and the coating/core interface is only visible for only coatings 1, 2, 7, 8, 13 and 18.

Table 3.3 Coating compositions of the coating aliases with the highlighted rows corresponding to OCT transparency.

	Nominal weight gain	**Measured weight gain** (%)	**Estimated coating thickness** (µm)	**Polymer**	**Plasticizer**	**Colourants**		**Auxiliary**
						Pigment	**Dye**	
Coating 1	3%	5.1 ± 1.1	40 ± 3	HPMC	PEG			
Coating 2	3%	5.5 ± 1.1	54 ± 5	HPMC HPC				
Coating 3	3%	6.2 ± 1.1	46 ± 4	HPMC	PEG			Lactose
Coating 4	3%	6.0 ± 1.1	50 ± 3	HPMC	Propylene glycol			Polydextrose
Coating 5	3%	3.4 ± 1.1	47 ± 9	HPMC		Red iron oxide Yellow iron oxide Titanium dioxide Talc		
Coating 6	3%	2.1 ± 1.2	27 ± 13	HPMC	PEG	Yellow iron oxide Titanium dioxide		
Coating 7	3%	5.1 ± 1.2	37 ± 4	PVA	PEG	Talc		
Coating 8	3%	5.7 ± 1.1	41 ± 3	Sodium CMC		Tapioca dextrin		Lecithin Sodium citrate Dextrose
Coating 9	3%	3.6 ± 1.1	59 ± 10	HPMC	PEG	Yellow iron oxide		

Coating 10	3%	3.2 ± 1.4	50 ± 18	HPMC	PEG Triacetin	Yellow iron oxide Black oxide Titanium dioxide		Lactose
Coating 11	3%	3.4 ± 1.0	53 ± 9	HPMC	PEG	Titanium dioxide	Blue	Capmul
Coating 12	3%	3.5 ± 1.1	55 ± 11	HPMC	PEG	Titanium dioxide Talc	Blue	
Coating 13	3%	3.1 ± 1.1	52 ± 10	PVA	PEG	Talc	Blue	
Coating 14	3%	3.4 ± 1.3	47 ± 12	PVA	PEG	Black oxide Carmine Titanium dioxide Talc	Blue	Lecithin
Coating 15	4%	4.3 ± 1.1	52 ± 12	PVA		Titanium dioxide Talc	Cu Chlorophillin	SLS
Coating 16	4%	5.0 ± 1.1	59 ± 10	HPMC HPC		Titanium dioxide Talc	Cu Chlorophillin	
Coating 17	3%	3.3 ± 1.2	60 ± 14	PVA	PEG	Riboflavine Spirilina Veg carbon black Titanium dioxide Talc		
Coating 18	3%	2.2 ± 1.1	28 ± 12	PVA	PEG	Yellow iron oxide Carmine Talc		Polysorbate
Coating 19	4%	6.4 ± 1.4	70 ± 15	PVA Eudragit	PEG	Yellow iron oxide Titanium dioxide Talc	Blue Yellow	
Coating 20	10%	9.9 ± 1.6	105 ± 13	Eudragit		Carmine Titanium dioxide Talc		Poloxamer SLS Sodium bicarbonate

								Calcium silicate
Coating 21	3%	3.4 ± 1.1	48 ± 10	PVA	PEG	Titanium dioxide Talc	Blue Yellow	Lecithin
Coating 22	3%	3.8 ± 1.2	54 ± 12	HPMC	Propylene glycol	Titanium dioxide	Blue	

3.5 Preliminary Study of In-line Monitoring of Pilot-scale Pellet Coating Process

In-line Experiment Setup

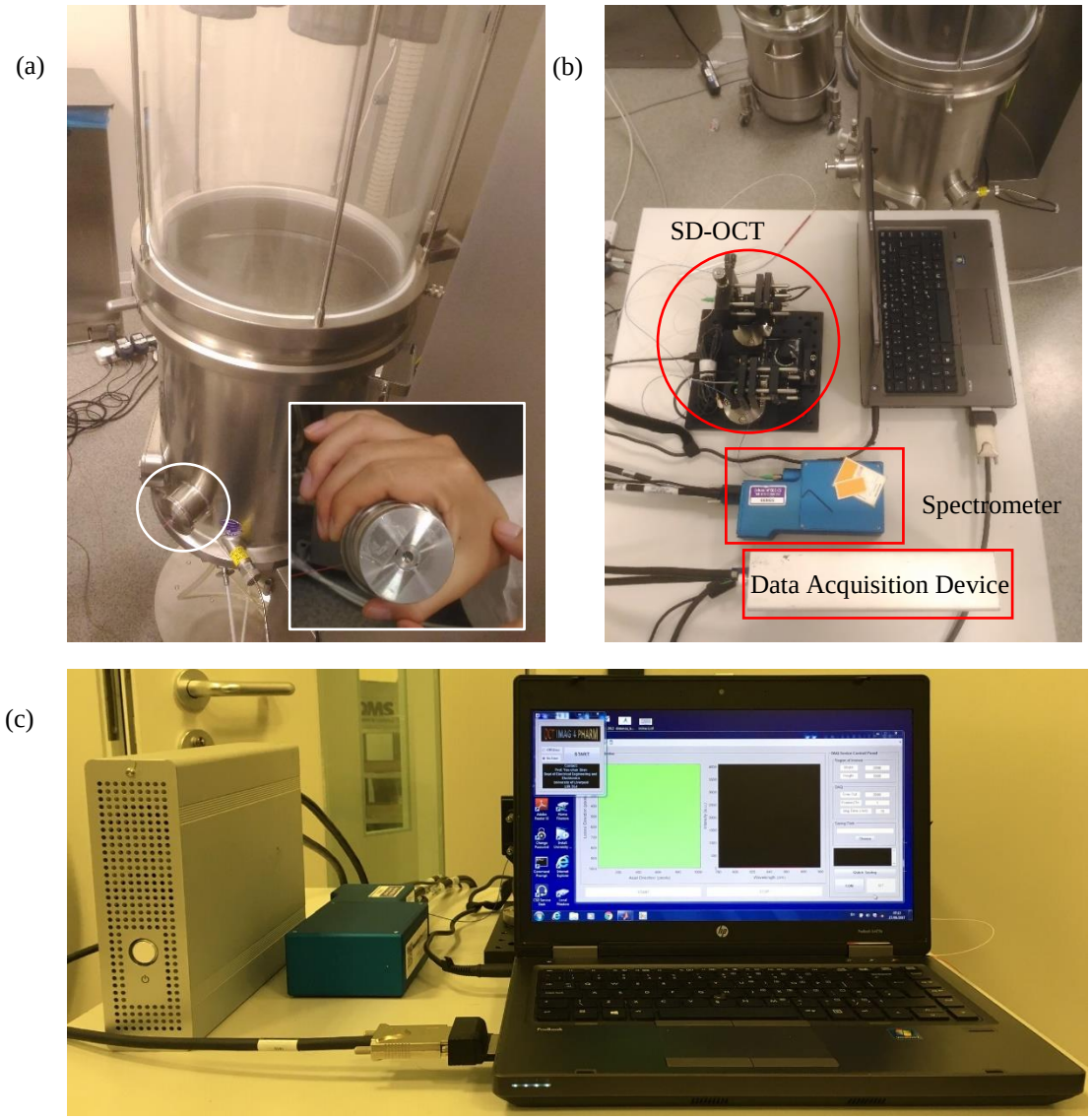

Figure 3.5 In-line SD-OCT experimental setup. (a) BOSCH Solidlab 2 fluid-bed coater and the insert is the port used for fixing the OCT sensor head. (b) SD-OCT system on-site installation at Bosch Hüttlin GmbH (Schopfheim, Germany). (c) In-line measurement monitoring software.

Figure 3.5 illustrates the on-site experimental setup, including the fluid-bed coater, the SD-OCT system, and the real-time monitoring software. Specifically, Figure 3.5(a) shows the fluid-bed coater utilised for the study, which is BOSCH Solidlab 2 (Bosch Hüttlin GmbH). The use of Solidlab 2 is important as it mimics a realistic process for a

possible scale up to a pilot and production scale process. Further, the unit comes with the PAT container for retrofitting sensors to monitor the process. This, therefore, removes the need of through the glass cylinder measurement that would, in turn, require dispersion compensation. The insert of Fig. 3.5(a) shows that the SD-OCT sensor head was fixed on the port of the PAT container. A sellotape was stuck together with the sensor head to shelter the pellets from damaging the sensor head. The whole system enables the quick on-site installation, which is contributed by the compact and portable design. A data acquisition device (National Instruments) was used to transfer the acquired raw spectrum signal from the spectrometer (Cobra 800, Wasatch Photonics) to the laptop with 4 Gbyte RAM. In addition, Figure 3.5(c) shows the in-line monitoring software, which was developed with MATLAB platform (MATLAB 2015a, MathWorks).

In-line measurement was carried out up to 65 minutes in total, with a sampling of 20 g every 6 minutes from the PAT container for off-line analysis. The acquired measurement data were processed to B-scan images and were directly displayed with a B-scan imaging rate of approximately 1 fps. It should be noted that the B-scan imaging rate includes the time to store the original spectra. Validation of the in-line measurements was performed by off-line analysis of the samples with the same SD-OCT system and a particle size analyser (the analysis results were provided by BOSCH). In addition, to assess the reproducibility, the coating experiment was repeated two times under the same coating conditions.

Result and Discussion

Figure 3.6 shows a series of B-scan images corresponding to the incremental coating operation time. A Region of Interest (ROI) searching method was used to localise the pellet positions. As aforementioned (Section 2.2.3), the imaging depth of an SD-OCT system is in principle decided by the spectrometer performance. However, the practical imaging depth is limited by the attenuation properties of the optical beam in the coating and the pellet core. Therefore, most of the images show only half of the pellet. The pellet width of the B-scan image is determined not only by the real size of the pellet (1.2 mm in diameter) but also by the pellet speed when it flies across the imaging beam. The speed range can be estimated by comparing the result of a mock in-line measurement, as shown in Fig. 3.7. Several small Homni pellets were fixed on a metal

lid with a diameter of 20 cm. A hole was drilled at the centre of the lid which was utilised to install a motor to rotate it at a rate of about one rotation per second. Each of the imaged Homni pellets had 80–100 pixels in the B-scan image. It can be estimated that the in-line measurements on the 1.2-mm pellet provided a speed range of 60–80 cm/s.

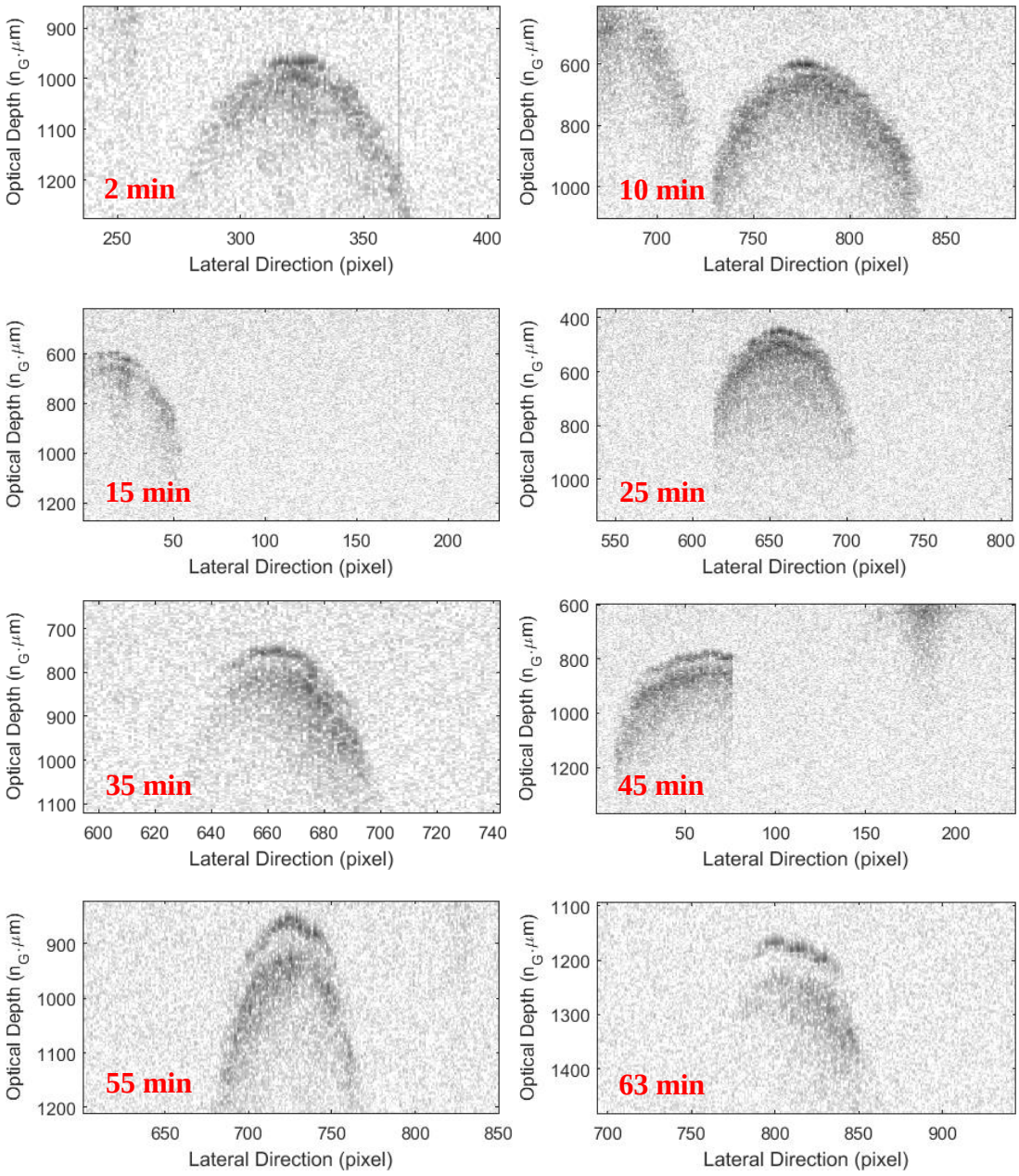

Figure 3.6 B-scan images of film coated pellets at different process time (in minutes). The pellet-covered area are extracted as Region of Interest (ROI) from their corresponding B-scan images (1000 × 2048 pixels).

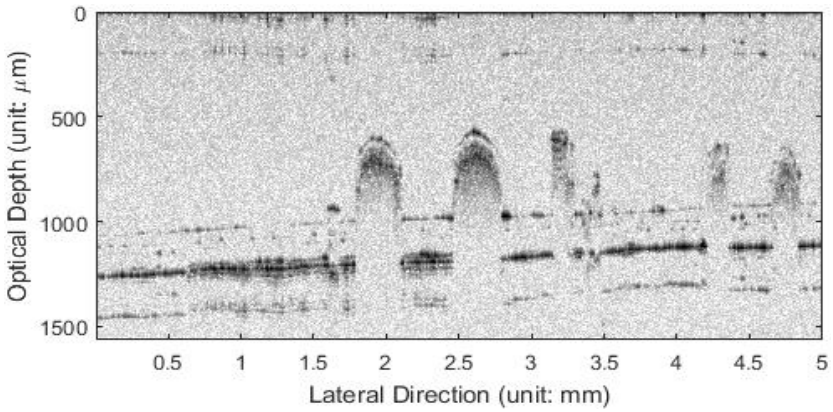

Figure 3.7 B-scan image of the film coated pellets (300–400 μm in diameter) for simulating the in-line measurement. The small pellet samples are mounted on a 20-cm-diameter circle lid, and the lid is rotated by a motor at a rate of one rotation per second.

The validation experiment was performed by analysing samples taken at 5, 15, 30, 45, 55 and 64 minutes. Figure 3.8 shows the selected OCT B-scan images of the samples. The off-line validation measurement was performed on 8 different pellets at each of the time intervals. It can be found that the image quality is better compared with the in-line measurement result. This is due to the fact that motion effects and vibrations exist in the on-site and in-line measurement environment. The coating thickness was measured by averaging 20 A-scans, which were manually selected from the apex area of each image. An assumed RI value of 1.5 was used for all thickness analysis.

Figure 3.9(a) shows the mean coating thickness as a function of process time. The result for the sampled pellets that were investigated in the off-line measurement with the SD-OCT and the particle size analyser was compared with the result from the in-line measurement. It can be noticed that there is a thickness growth trend in both the in-line and off-line measurement results. A good matching between the in-line and off-line results can be also found in 25, 30, 40 and 55 minutes. However, there is an obvious error between 40–50 minutes. In addition, a thickness value of 30 μm was measured from the pellet sample at the end of the coating process, which is below the expected value of about 100 μm. The possible experiment errors may be the settings of the coater's operation parameter during the coating process. The replication experiment results illustrated a similar trend despite the error that occurred around 40 minutes still existed, as shown in Fig. 3.9(b), indicating the application potential of the SD-OCT system.

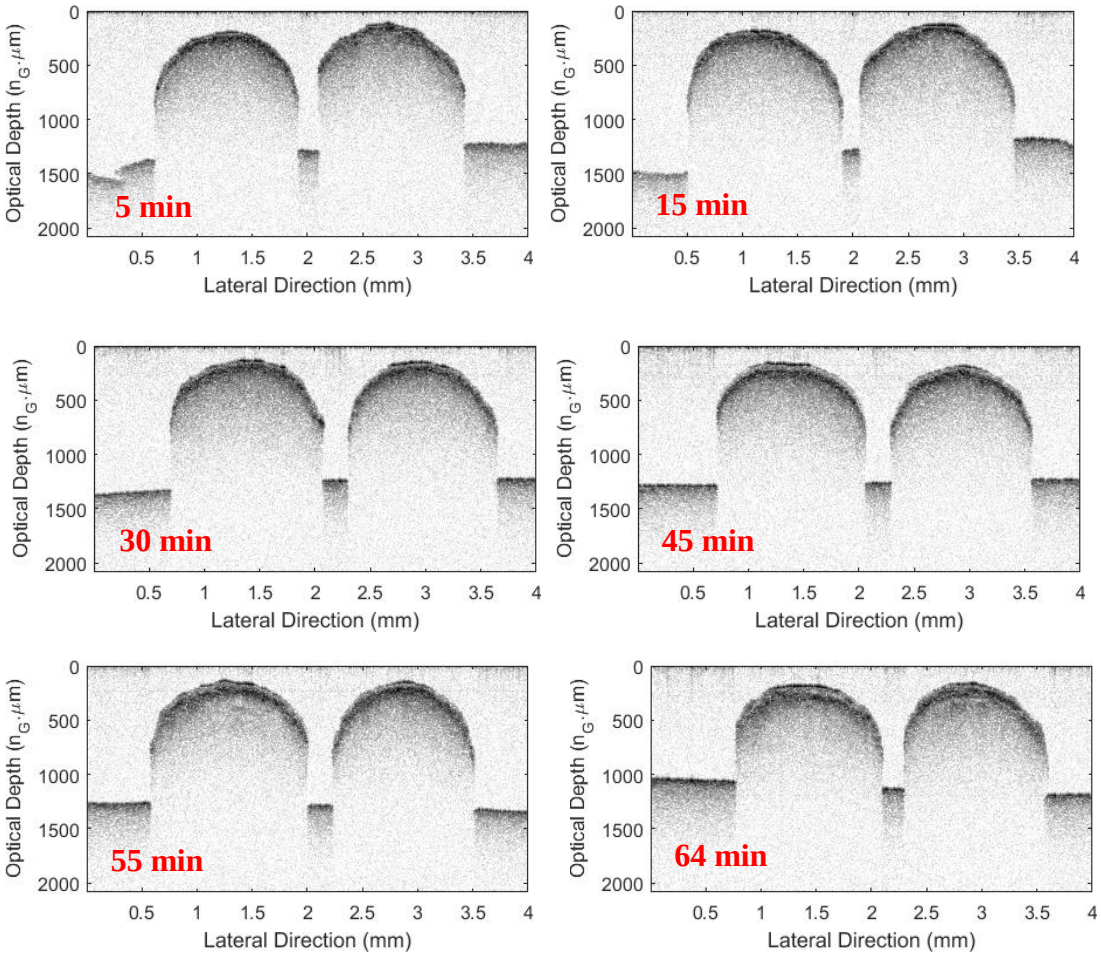

Figure 3.8 B-scan images of film-coated pellets samples at different process times (in minutes) obtained from off-line measurement. Image dimension (in the air) are 4.0 × 2.0 mm^2 (1000 ×512 pixels)

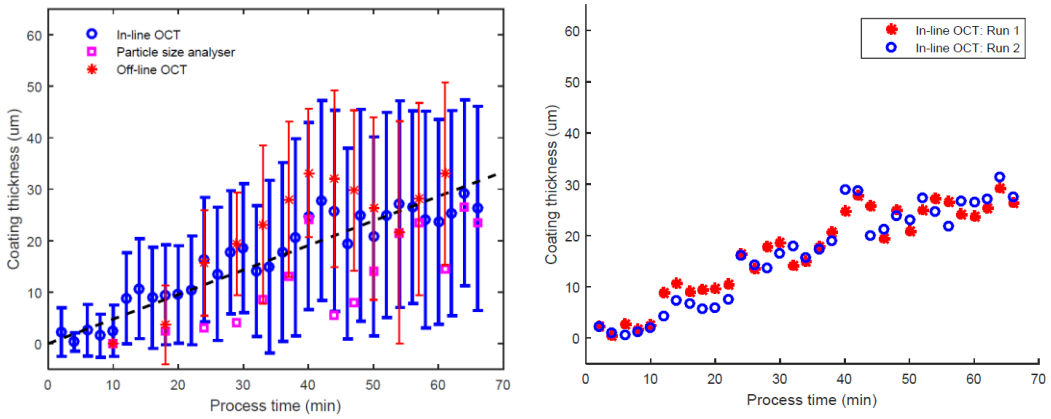

Figure 3.9 The mean coating thickness as the function of process time. (a) Mean thickness measured from the in-line SD-OCT experiment validated by off-line SD-OCT and particle size analyser measurement. (b) Coating thickness comparison of two replication experiments.

3.6 Conclusion

In this chapter, a cost-effective SD-OCT system for characterising pharmaceutical film coatings has been developed. The use of an SLD diode with customised light focusing and collection components has achieved a coupling efficiency of 44%. The cost of the whole system is much lower than the other reported SD-OCT systems in the application, where expensive supercontinuum lasers or SLDs are commonly utilised as a light source. The system is capable of imaging pharmaceutical coatings between 10–100 μm with its achieved resolutions of 9 μm and 25 μm in axial and lateral directions, respectively.

The system is firstly used to investigate the applicability of an infrared SD-OCT (centred at 840 nm) to image 22 pharmaceutical tablets with different common coating formulations. The findings show that while OCT is a promising technology for the characterisation of pharmaceutical coatings, coating transparency for OCT measurements ultimately is underpinned by properties relating to the pigment, coating material and the tablet core as well as the coating process itself. The findings have further identified that when the coating material contains titanium dioxide, either alone or together with other pigments, the measurement becomes adversely affected by scattering, leading to the unclear observation of the coating/core interface that is essential for coating thickness quantification. For coatings without titanium dioxide, coating transparency also cannot be guaranteed.

On the other hand, the SD-OCT was used as a PAT tool for in-line monitoring of the pellet coating process. An adjustable fibre collimator was used in the sample arm as the sensor head that can be directly integrated with the fluid-bed coater. The preliminary study shows that the SD-OCT with an A-scan rate of 43 kHz is capable of imaging the randomly moving pellets (3 kg) in the fluid-bed coater. The in-line measurement result is validated by both the off-line measurement from the SD-OCT and a particle size analyser measurement. The quantified coating thickness as the function of coating process time illustrates a growth, which can be found in both in-line and off-line results. However, the large standard deviation derived from the in-line result demonstrates the difficulty and challenge of such in-line application with pilot-scale pellet samples although it might be significantly affected by the operation error of the fluid bed apparatus during the coating process.

Studies to date have clearly demonstrated the potential of SD-OCT for the off-line and in-line analysis of pharmaceutical coatings. However, the field is currently facing some challenges and limitations: (1) A number of typical coating formulations (in particular cosmetic coatings) cause strong scattering thus limiting the penetration depth of OCT to tens of µm, in some case, making the detection of coating/core interface impossible. To carry out applicability study prior to coating quality analysis is therefore necessary, especially for a tablet/pellet coated with new coating formulation. (2) Window fouling during in-process control may either affect the data quality or, in the worst case, render the data useless as the signal strength of the back-reflections from the sample is not sufficiently high to detect the interfaces between the coating layer and the core material. (3) The integration of the sensor in the process is a critical aspect, which may have a significant effect on the quality of the measurements. This is particularly important for the integration of an OCT probe in a fluid-bed coater, where the particles typically do not have defined and uniform movement. In this case, the sensor needs to be positioned where the pellets/mini-tablets pass the sensor with a low but constant speed. However, (2) and (3) are challenges that are applicable to almost every measurement technology that is used to monitor a product quality attribute. OCT has the advantage compared to most other techniques, in particular Near-infrared (NIR) and Raman spectroscopy, that challenges (2) and (3) can be relatively easily detected. Window fouling will result in a built up of material on the OCT probe causing the disappearance of the tablets in the OCT image. Misalignments of the probe with respect to the samples of interest can be detected by comparing the contrast from the coating interface from in-line data to that from off-line measurements. The majority of OCT systems used for assessing the quality of film-coatings operated at a central wavelength of 700–900 nm in order to improve axial resolution rather than penetration power. The A-scan rate is particularly important for the in-line monitoring of the coating quality. There is great potential to adopt technologies from fields beyond pharmaceutical sciences, which have demonstrated A-scan acquisition rates > 1 MHz [**32**]. Finally, like any other PAT, data quickly builds up, especially operating at acquisition rates up to 1 MHz, leading to the need to address the issue of data management or optimal sampling strategy.

References

[1] G. V. Savage and C. Rhodes, "The sustained release coating of solid dosage forms: a historical review," Drug Development and Industrial Pharmacy, vol. 21, no. 1, pp. 93-118, 1995.

[2] L. A. Felton, *Aqueous polymeric coatings for pharmaceutical dosage forms*. CRC Press, 2016.

[3] M. J. Rathbone, J. Hadgraft, M. S. Roberts, and M. E. Lane, *Modified-release drug delivery technology*. CRC Press, 2008.

[4] S. V. Sastry, J. R. Nyshadham, and J. A. Fix, "Recent technological advances in oral drug delivery–a review," Pharmaceutical Science & Technology Today, vol. 3, no. 4, pp. 138-145, 2000.

[5] F. Siepmann, J. Siepmann, M. Walther, R. MacRae, and R. Bodmeier, "Polymer blends for controlled release coatings," Journal of Controlled Release, vol. 125, no. 1, pp. 1-15, 2008.

[6] P. Pandey and R. Bharadwaj, Predictive Modeling of Pharmaceutical Unit Operations. Woodhead Publishing, 2016.

[7] D. Suzzi, S. Radl, and J. G. Khinast, "Local analysis of the tablet coating process: Impact of operation conditions on film quality," Chemical Engineering Science, vol. 65, no. 21, pp. 5699-5715, 2010.

[8] D. Suzzi, G. Toschkoff, S. Radl, D. Machold, S. D. Fraser, B. J. Glasser, and J. G. Khinast, "DEM simulation of continuous tablet coating: Effects of tablet shape and fill level on inter-tablet coating variability," Chemical Engineering Science, vol. 69, no. 1, pp. 107-121, 2012.

[9] G. Toschkoff and J. G. Khinast, "Mathematical modeling of the coating process," International Journal of Pharmaceutics, vol. 457, no. 2, pp. 407-422, 2013.

[10] W. Chen, S. Y. Chang, S. Kiang, A. Marchut, O. Lyngberg, J. Wang, V. Rao, D. Desai, H. Stamato, and W. Early, "Modeling of pan coating processes: Prediction of tablet content uniformity and determination of critical process parameters," Journal of Pharmaceutical Sciences, vol. 99, no. 7, pp. 3213-3225, 2010.

[11] L. Li, J. Remmelgas, B. G. van Wachem, C. von Corswant, M. Johansson, S. Folestad, and A. Rasmuson, "Residence time distributions of different size particles in the spray zone of a Wurster fluid bed studied using DEM-CFD," Powder Technology, vol. 280, pp. 124-134, 2015.

[12] G. Toschkoff, S. Just, A. Funke, D. Djuric, K. Knop, P. Kleinebudde, G. Scharrer, and J. G. Khinast, "Spray models for discrete element simulations of particle coating processes," *Chemical Engineering Science*, vol. 101, pp. 603-614, 2013.

[13] K. Knop and P. Kleinebudde, "PAT-tools for process control in pharmaceutical film coating applications," International Journal of Pharmaceutics, vol. 457, no. 2, pp. 527-536, 2013.

[14] K. Korasa and F. Vrečer, "Overview of PAT process analysers applicable in monitoring of film coating unit operations for manufacturing of solid oral dosage forms," European Journal of Pharmaceutical Sciences, vol. 111, pp. 278-292, 2018.

[15] J. M. Mauritz, R. S. Morrisby, R. S. Hutton, C. H. Legge, and C. F. Kaminski, "Imaging pharmaceutical tablets with optical coherence tomography," Journal of Pharmaceutical Sciences, vol. 99, no. 1, pp. 385-391, 2010.

[16] S. Zhong, Y. C. Shen, L. Ho, R. K. May, J. A. Zeitler, M. Evans, P. F. Taday, M. Pepper, T. Rades, K. C. Gordon, and R. Müller, "Non-destructive quantification of pharmaceutical tablet coatings using terahertz pulsed imaging and optical coherence tomography," Optics and Lasers in Engineering, vol. 49, no. 3, pp. 361-365, 2011.

[17] Y.C. Shen, "Terahertz pulsed spectroscopy and imaging for pharmaceutical applications: a review," International Journal of Pharmaceutics, vol. 417, no. 1-2, pp. 48-60, 2011.

[18] R. K. May, M. J. Evans, S. Zhong, I. Warr, L. F. Gladden, Y. Shen, and J. A. Zeitler, "Terahertz in-line sensor for direct coating thickness measurement of individual tablets during film coating in real-time," Journal of Pharmaceutical Sciences, vol. 100, no. 4, pp. 1535-1544, 2011.

[19] I.S. Russe, D. Brock, K. Knop, P. Kleinebudde, and J. A. Zeitler, "Validation of terahertz coating thickness measurements using X-ray microtomography," Molecular Pharmaceutics, vol. 9, no. 12, pp. 3551-3559, 2012.

[20] M. Haaser, K. C. Gordon, C. J. Strachan, and T. Rades, "Terahertz pulsed imaging as an advanced characterisation tool for film coatings—A review," International Journal of Pharmaceutics, vol. 457, no. 2, pp. 510-520, 2013.

[21] H. Lin, Y. Dong, Y. Shen, and J. A. Zeitler, "Quantifying pharmaceutical film coating with optical coherence tomography and terahertz pulsed imaging: an evaluation," Journal of Pharmaceutical Sciences, vol. 104, no. 10, pp. 3377-3385, 2015.

[22] H. Lin, Y. Dong, D. Markl, B. M. Williams, Y. Zheng, Y. Shen, and J. A. Zeitler. "Measurement of the intertablet coating uniformity of a pharmaceutical pan coating process with combined terahertz and optical coherence tomography in-line sensing," Journal of Pharmaceutical Sciences, vol. 106, no. 4, pp. 1075-1084, 2017.

[23] D. M. Koller, G. Hannesschläger, M. Leitner, and J. Khinast, "Non-destructive analysis of tablet coatings with optical coherence tomography," European Journal of Pharmaceutical Sciences, vol. 44, no. 1-2, pp. 142-148, 2011.

[24] D. Markl, G. Hannesschläger, S. Sacher, M. Leitner, and J. G. Khinast, "Optical coherence tomography as a novel tool for in-line monitoring of a pharmaceutical film-coating process," European Journal of Pharmaceutical Sciences, vol. 55, pp. 58-67, 2014.

[25] D. Markl, M. Zettl, G. Hannesschläger, S. Sacher, M. Leitner, A. Buchsbaum, and J. G. Khinast, "Calibration-free in-line monitoring of pellet coating processes via optical coherence tomography," Chemical Engineering Science, vol. 125, pp. 200-208, 2015.

[26] D. Markl, G. Hannesschläger, S. Sacher, M. Leitner, J. G. Khinast, and A. Buchsbaum, "Automated pharmaceutical tablet coating layer evaluation of optical coherence tomography images," Measurement Science and Technology, vol. 26, no. 3, p. 035701, 2015.

[27] J. Song, J. Qin, J. Qu, Z. Song, W. Zhang, X. Xue, Y. Shi, T. Zhang, W. Ji, R. Zhang, H. Zhang, "The effects of particle size distribution on the optical properties of titanium dioxide rutile pigments and their applications in cool non-white coatings," Solar Energy Materials and Solar Cells, vol. 130, pp. 42-50, 2014.

[28] R. Levinson, P. Berdahl, and H. Akbari, "Solar spectral optical properties of pigments—Part II: survey of common colorants," Solar Energy Materials and Solar Cells, vol. 89, no. 4, pp. 351-389, 2005.

[29] M. Ruotsalainen, J. Heinämäki, H. Guo, N. Laitinen, and J. Yliruusi, "A novel technique for imaging film coating defects in the film-core interface and surface of coated tablets," European Journal of Pharmaceutics and Biopharmaceutics, vol. 56, no. 3, pp. 381-388, 2003.

[30] N. Pourkavoos and G. E. Peck, "The effect of swelling characteristics of superdisintegrants on the aqueous coating solution penetration into the tablet matrix during the film coating process," Pharmaceutical Research, vol. 10, no. 9, pp. 1363-1371, 1993.

[31] R. Levinson, P. Berdahl, and H. Akbari, "Solar spectral optical properties of pigments—Part I: model for deriving scattering and absorption coefficients from transmittance and reflectance measurements," Solar Energy Materials and Solar Cells, vol. 89, no. 4, pp. 319-349, 2005.

[32] S. Wang, M. Singh, A. L. Lopez, C. Wu, R. Raghunathan, A. Schill, J. Li, K. V. Larin, I. V. Larina, "Direct four-dimensional structural and functional imaging of cardiovascular dynamics in mouse embryos with 15 MHz optical coherence tomography," Optics Letters, vol 40, no. 20, pp. 4791–4794, 2015.

Chapter 4 Ultrahigh-resolution Imaging of Thin Film Coatings

4.1 Introduction

The Optical Coherence Tomography (OCT) techniques that have been developed and studied for the off-line pharmaceutical applications are enumerated in Table 4.1. In terms of resolution performance, Dong and Lin *et al*. reported their Spectral-Domain OCT (SD-OCT) system with a 16 μm × 5.7 μm (lateral × axial) resolution to investigate intra-tablet coating uniformity [**1**]. Markl *et al.* reported their SD-OCT system with an improved resolution of about 10 μm × 4.9 μm for both the off-line and in-line applications with tablet and pellet dosage form. A Full-Field OCT (FF-OCT) system demonstrated by Li *et al*. had a higher resolution of 11 μm × 3.6 μm to evaluate coating structures on small pellet (diameter is approximately 1 mm) [**2**]. To date, the highest axial resolution achieved is 0.9 μm (Zhong *et al*.) by using a broadband halogen lamp as the light source. However, the system used a halogen lamp that renders the system bulky, energy inefficient and difficult to align.

In terms of the used techniques and measured dosage forms from previous work, much research was focused on tablet samples with a single coating layer, with a coating thickness around a few tens of microns or close to 100 μm. Moreover, most of the developed OCT systems were based on the SD-OCT technique. Thus, it shows that there was a lack of the application on the characterisation of even thinner coatings (i.e. the coating thickness of less than 10 μm). On the other hand, very few studies have explored the imaging of small pellets with more complex structures (i.e. multi-layer coating structures). Given the developed SD-OCT systems, the intrinsic features of an SD-OCT modality such as autocorrelation artefact could affect the resultant image quality. Further, an SD-OCT usually uses a large Depth of Focus (DOF) to acquire the entire range of a tomography signal (A-scan), thus limiting the use of a high Numerical Aperture (NA) objective to enhance the lateral resolution. The previous study implied that FF-OCT might be highly suitable to provide high-quality Three-Dimensional (3D) data of small pellets even with a multi-layer microstructure of film coating [**2**]. However, the reported FF-OCT system in the study employed an infrared source centred at 850 nm and a common focus lens with the NA of 0.1, which limits both the axial and lateral resolutions. Also, the determination of coating thickness in the study

was carried out by manually analysing several A-scan signals and adopting empirical refractive index on all layers. This is, in practice, not suitable for a multi-layer pellet, especially the pellets that consist of different coating materials corresponding to different Refractive Index (RI). As for the thickness analysis scheme, partial use of the captured volumetric data may not provide more significant parameter such as intra-pellet coating uniformity.

Phase stepping and shifting methods are the most popular reconstruction strategy for FF-OCT, which are used to extract the OCT signal/image [**4**–**6**]. Several authors reported their FF-OCT systems that employed piezoelectric stage actuator (PZT) to generate oscillation at the reference arm. Three or four-phase-stepped images were acquired with the displacements of the reference mirror and were used then for the reconstruction of OCT images. The requirement of usually more than three interferograms at each phase shifting position limits the operation speed of an FF-OCT system. A number of studies have been reported to increase imaging efficiency with sophisticated hardware based (optical or electrical) implementations. For example, Dubois *et al*. [**7**], proposed an FF-OCT system based on lock-in detection technique, where a photo-elastic birefringence modulator was used to generate a sinusoidal phase shift between the sample and reference waves, four original interferograms can be recorded successively and then demodulated to an OCT image. Akiba *et al*. [**8**], proposed a heterodyne detection technique, where two synchronised Charge-Coupled Device (CCD) cameras were used to simultaneously acquire two quadrature and Direct Current (DC) images to obtain an OCT image. Sato *et al*. [**9**], introduced Wollaston prism to realise optical Hilbert transform, in which the interferograms of four phase shifts were reduced to two acquisitions.

In this chapter, an Ultrahigh-Resolution (UHR) Linnik-typed FF-OCT system is reported. It was operated with an axial resolution of 0.98 μm and a lateral resolution of 1.6 μm achieved by using high-NA (NA: 0.3) microscope objectives and broadband LED source centred at 600 nm with an FWHM of 200 nm. The proposed FF-OCT realises 1) the characterisation of thinner pharmaceutical film coatings; 2) the imaging of multi-layer micropellets (diameter <1 mm). Firstly, a continuous acquisition scheme together with a software-based reconstruction method is presented. The measurement can be continuously operated without employing any components to generate phase information for retrieving tomography images. The FF-OCT was applied to investigate

two applications 1) the applicability of using the FF-OCT to differentiate branded pharmaceutical tablets from the generic suppliers in terms of coating structures, for the first time, was demonstrated. Specifically, thin coating structures of approximately 4 µm could be resolved in GlaxoSmithKline (GSK) Panadol tablets but not present in the generics. To determine the coating thickness, the coating structures were automatically detected by a fast graph-based segmentation algorithm; 2) the proposed FF-OCT was used to capture a fine 3D volumetric datacube from multi-layer micropellets, and a 3D segmentation technique was developed, which enables the coating thickness map with high resolution to be obtained. In order to validate the system, the same pellet sample was measured by X-ray Micro Computed Tomography (XµCT), and the RI corresponding to each coating layer was determined by comparing cross-sectional (B-scan) images of the OCT and XµCT. This may provide a unique capability of determining the RI of a pellet coating layer at its native state nondestructively, while standard spectroscopy methods can only measure the RI of the coating material itself.

Table 4.1 Reported Optical Coherence Tomography (OCT) systems used for off-line measurement of pharmaceutical coatings

Reference	Measurement	Light Source	Central Wavelength/ Bandwidth (nm)	Axial Resolution (um)	Lateral Resolution (um)	Acquisition rate
Juuti *et al*. (2009)	Off-line (SD-OCT)	/ [a]	/	/	5	/
Mauritz *et al*. (2009)	Off-line (SD-OCT)	Spectral radar OCT OCP930SR (Thorlabs)	930/100	6.5	9	15 kHz
		Swept source OCT Microscope OCM1300SS (Thorlabs)	1325/130	12	15	16 kHz
Zhong *et al*. (2010)	Off-line (SD-OCT)	Tungsten Halogen Lamp	700/236	0.9	/	/
Koller *et al*. (2011)	Off-line (SD-OCT)	Supercontinuum Lasers (NKT Photonics)	820/150	<4	4.3	20 kHz
Li *et al*. (2013)	Off-line (FF-OCT)	LED	850/90	3.6	11	120 FPS
Markl *et al*. (2014)	Off-line (SD-OCT)	TELESTO^{TM} OCT (Thorlabs)	1325/150	7.5	/	/
		SLD (Superlum Diode)	830/62	4.9	9.51	27.8 kHz
Markl *et al*. (2015)	Off-line (SD-OCT)	Supercontinuum Lasers (NKT Photonics)	820/150	1.98	13.05	20 kHz
Lin *et al*. (2015)	Off-line (SD-OCT)	SLD (EXALOS)	840/55	5.7	16	/
Dong *et al*. (2017)	Off-line (SD-OCT)	SLD (EXALOS)	844/131	2.4	/	45 kHz
Lin *et al*. (2017)	Off-line (SD-OCT)	SLD (EXALOS)	840/55	5.7	20	/
Markl *et al*. (2018)	Off-line (SD-OCT)	SLD (Superlum Diode)	832/75	4.1	10	59.2 kHz

[a] unmentioned specification in the literature

4.2 Method

4.2.1 Image Reconstruction Algorithm

A 3D datacube can be acquired through single scanning in the sample's axial direction for an FF-OCT modality, where a CCD or Complementary Metal–Oxide–Semiconductor (CMOS) camera is used to record a series of Two-Dimensional (2D) interferograms (x-y plane) to form the 3D datacube. The imaging scheme can be mathematically expressed as Eq. 4.1 when considering time-domain FF-OCT imaging theory.

$$I_{FF-OCT}(x,y,\Delta z) = \int S(\omega)\Bigg(R_{Ref}(x,y) + \sum_{i=1}^{N} R_{Sampl-\mathrm{ith}}(x,y) + 2\sum_{i=1}^{N}\sqrt{R_{Ref}(x,y)R_{Sampl\text{-}\mathrm{ith}}(x,y)}\cos[\phi(x,y,\Delta z)]\Bigg) d\omega \tag{4.1}$$

where $S(\omega)$ represents the intensity spectrum of a Gaussian shaped light source as a function of frequency ω, R_{Ref} is the reflectivity of a reference mirror and $R_{Sampl\text{-}\mathrm{ith}}$ is the reflectivity of the i-th reflector of a sample with N layers. In addition, $\phi(x,y,\Delta z)$ represents the phase changes when translating either the reference arm or the sample arm by a distance Δz. The light echoes from different reflectors within the sample and the positions of the reference mirror give rise to time delay information. The recorded signal intensity consists of three components over the integrated source spectrum, which are DC offset, cross-correlation signal and auto-correlation signal. DC offset is due to the reflectivity from both the two interferometer arms. Cross-correlation signal is generated with the interference between the reference mirror and the sample reflectors at multiple depths. Auto-correlation signal results from the interference between the different sample reflectors, which has been ignored in Eq. 4.1 since it is independent of the moving distance Δz. Eq. 4.1 can be rewritten as the sum of the DC signal and the cross-correlation signal intensities as

$$I_{FF-OCT}(x,y,\Delta z) = I_{DC}(x,y) + I_{Cross}(x,y,\Delta z)\cos\phi(x,y,\Delta z) \tag{4.2}$$

The phase-shift method is a common method of FF-OCT image reconstruction, where phase shifting is implemented by oscillating the reference arm using a PZT. At each scanned depth position, four interferograms and their corresponding phase-shift steps $\ell = 0,1,2,3$ are acquired, which can be written as Eq. 4.3

$$I_{FF-OCT}^{\ell}(x,y,\Delta z) = I_{DC}(x,y) + I_{Cross}(x,y,\Delta z)\cos\left(\phi(x,y,\Delta z) + \frac{\ell\pi}{2}\right) \tag{4.3}$$

A number of *en-face* images can be reconstructed to form a 3D OCT datacube with Eq. 4.4

$$I_{Cross}(x,y,\Delta z) \propto \left[I_{FF-OCT}^{\ell=0} - I_{FF-OCT}^{\ell=2}\right]^2 + \left[I_{FF-OCT}^{\ell=1} - I_{FF-OCT}^{\ell=3}\right]^2 \tag{4.4}$$

In our proposed imaging scheme, a series of 2D interferograms along the axial direction are captured continuously to form a raw 3D datacube by employing a high-precision linear stage to translate the sample at a nanoscale sampling interval. Even though this would require extensive hardware storage, it nevertheless reduces hardware complexity since only a motorised stage is required for the experiment. The image reconstruction task is converted from retrieving a series of *en-face* images to demodulating A-scan signals, which allows the use of postprocessing methods for image reconstruction.

We introduce a normalised mirror signal, denoted as $I_{Mirror}(\Delta z')$, which is generated by measuring the surface of a flat mirror with the same scanning step as the measurement performed on a sample. By convolving the mirror signal with the raw A-scan signals, it effectively functions as a weighted average filter to remove the DC offset while amplifying the cross-correlation signal. This step can be expressed as Eq. 4.5

$$I'_{FF-OCT}(x,y,\Delta z) = I_{FF-OCT}(x,y,\Delta z) \otimes I_{Mirror}(\Delta z') \tag{4.5}$$

where '⊗' represents the convolution operator. Further, by taking Hilbert transform, denoted by $H\{\}$, all the A-scan signals can be demodulated to form the reconstructed OCT datacube, which is written as Eq. 4.6

$$I'_{Cross}(x,y,\Delta z) = \sqrt{\left[I'_{FF-OCT}(x,y,\Delta z)\right]^2 + \left[H\{I'_{FF-OCT}(x,y,\Delta z)\}\right]^2} \tag{4.6}$$

It should be noted that practical signal demodulation is performed using a multithreaded process, where the size of the demodulated signals is one-tenth of the original ones after resampling. Thus, the reconstruction time for a sample volume of 100 × 100 × 1000 pixels takes approximately ten seconds while freeing up over 20 MB of data storage.

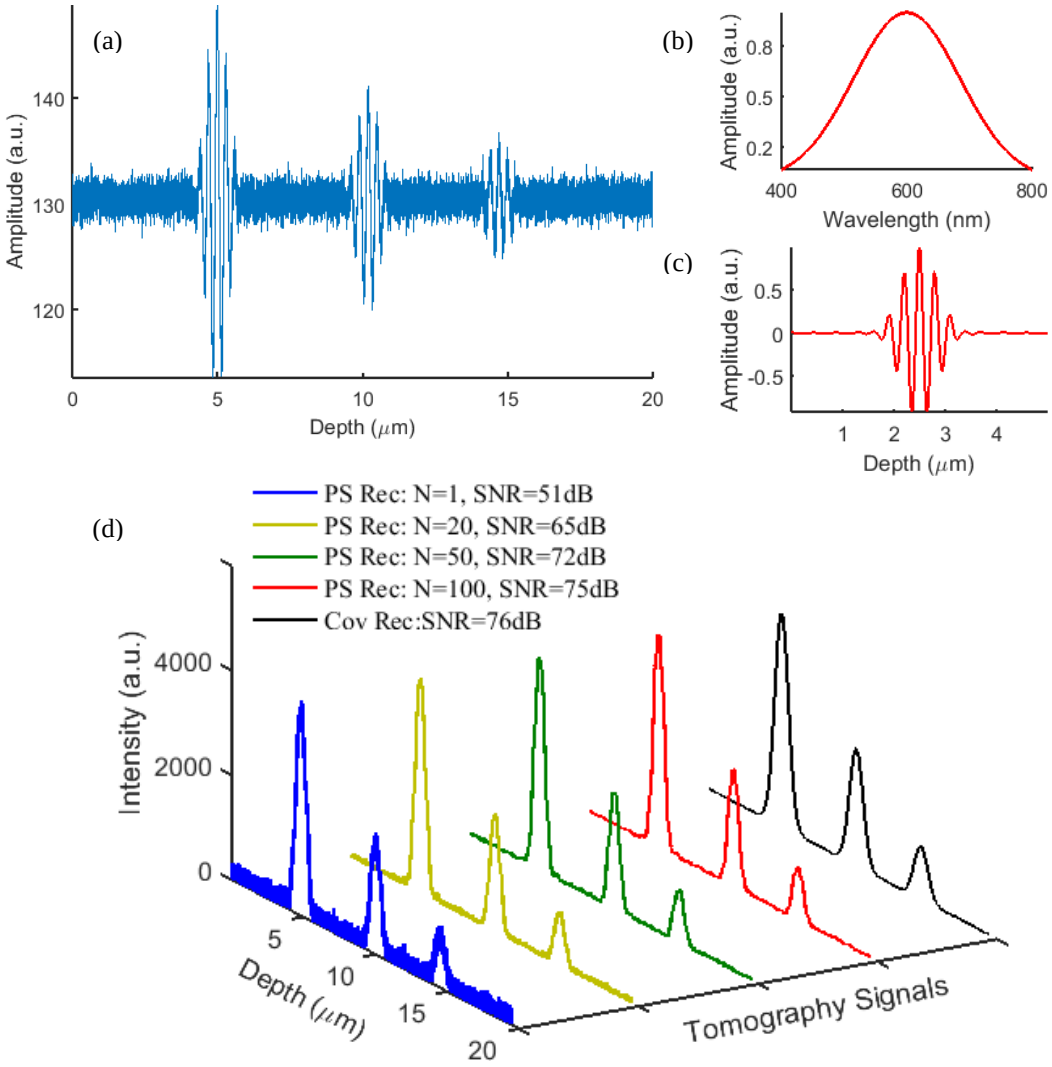

Figure 4.1 Simulation of the proposed Full-Field Optical Coherence Tomography (FF-OCT) image reconstruction scheme. (a) Interferogram of a three-layered object. (b) Light source spectrum with 600-nm central wavelength and 200-nm bandwidth. (c) Interference signal of a simulated mirror sample. (d) Tomography signals (A-scan) based on phase-shift method with N accumulated signals (blue line: N=1; yellow line: N=20; green line: N=50; red line: N=100) and using convolution with Hilbert transform (black line).

As a further illustration, a time-domain interferogram corresponding to a sample with three layers was simulated, and Gaussian noise was applied to the original signal, as shown in Fig. 4.1(a). The simulated source had a Gaussian-shaped spectrum centred at 600 nm with a Full-Width-at-Half-Maximum (FWHM) of 200 nm (see Fig. 4.1(b)), consistent with the light sources typically used in the UHR FF-OCT. Figure 4.1(c)

shows a simulated mirror interferogram after normalisation, where the measured FWHW was 0.8 μm that represents the axial resolution determined by the broadband source. In order to assess the proposed reconstruction method, the depth information of the sample (Fig. 4.1(a)) was reconstructed by using the classic phase-shift method at four shifted phase positions. As shown in Fig. 4.1(d), the solid blue line is the A-scan which uses the single image at each quarter position for reconstruction. The yellow, green, and red solid lines in Fig. 4.1(d) are the reconstructed A-scans that correspond to 20, 50 and 100 accumulated images per phase shift, respectively, in which the increased Signal-to-Noise Ratio (SNR) can be observed. The solid black line in Fig. 4.1(d) shows that A-scan signal reconstructed using the proposed method closely resembles the one using the classic phase-shift method. The FWHM measured from the A-scan signal (solid black line) is approximate 1 μm in close agreement with the theoretically axial resolution (0.8 μm).

4.2.2 3D Segmentation Technique for Multi-layer Micropellet Applications

The aim here is to measure the thickness of each of the coating layers of a multi-layer pellet. In order to do this, the locations of the boundaries of each surface coating need to be obtained, and they can be found from the captured OCT data. To achieve this in the acquired 3D datacube would be an impractical, time consuming and arduous task, particularly given the data size in each dimension. Therefore, the aim is to determine the location of the boundary points of each coating surface automatically. This can be achieved by adopting a graph-search approach that achieves excellent performance in terms of speed and accuracy with OCT data. For efficiency, the 3D volume's *en-face* data is segmented slice-by-slice rather than solving a full-3D surface model, followed by a refinement step. Given the found contours, the thickness of each coating layer can then be measured.

Since the coated pellet samples are circular in *en-face* scans, it is logical to consider the data in polar coordinates rather than Cartesian. An estimate of the centre location of the pellet within the OCT volume is determined by finding the average pixel location, weighted by the intensity values for each *en-face* scan. The mean centre location across scans in the axial direction is then calculated to be the central point (x_c, y_c), which is kept fixed for each *en-face* scan. The polar transform functions can be defined as

$$\theta(x,y)=\tan^{-1}\left(\frac{y-y_c}{x-x_c}\right),\quad r(x,y)=\sqrt{(x-x_c)^2+(y-y_c)^2} \tag{4.7}$$

Letting the OCT intensity values be denoted by the function u, note that $u = I'_{Cross}(x,y,\Delta z)$, we proceed to determine the segmentation of the coating boundaries in each *en-face* slice $u_z(x,y)=u(x,y,z)$. In order to find the pellet coating boundaries of each slice efficiently, a graph-search segmentation approach is adopted. Here, a graph in polar coordinates around the calculated graph centre (x_c,y_c) is defined. The graph nodes are considered to be connected by an edge if they are no more than one step size away in terms of angle θ (1 degree) and radius r (height of one pixel). Going through each of the *en-face* slices, the segmentation is carried out by minimising the costing of traversing the graph with the weighting energy defined as

$$E[u_z(x,y)]=\frac{\partial u_z(x,y)}{\partial\theta}+\beta\frac{\partial u_z(x,y)}{\partial r} \tag{4.8}$$

where $\beta = 0.1$ was chosen empirically. The first contour was found as that corresponding to the minimal cost path through the defined graph, the second contour as that corresponding to the path of second lowest overall cost, without crossing any determined paths, and so on. The result of this step is a series of functions $p_z^{\ell}(\theta), \ell = 1,2,3$, which define the contours on the graph domain. From this, the equations of the surface contours $C^{\ell}(x,y)$ can be determined in Cartesian coordinates canonically.

Since, for efficiency, the segmentations have so far been carried out in each *en-face* scan independently, a fast refinement step that takes into account all directions is carried out. The positions around each defined coating edge surface $C^{\ell}(x,y)$ are isolated, and the likelihood of them is considered, in which they should belong to the coating layer in question based on mean local mean intensity in an expansion-contraction approach. The aim now is to measure the thickness of the ℓth coating layer lying between surfaces C^{ℓ} and $C^{\ell+1}$. For each point (x,y) on the refined surface C^{ℓ}, least squares method is used to find the closest corresponding point lying on the surface $C^{\ell+1}$ and measure the Euclidean distance. That is, the thickness map is calculated for each pellet coating layer.

$$t^{\ell}(x,y)=\min_{(v,w)\in\mathbb{Z}^2}\left\{\sqrt{\left(x-v\right)^2+\left(y-w\right)^2+\left(C^{\ell}(x,y)-C^{\ell+1}(v,w)\right)^2}\right\} \tag{4.9}$$

4.3 Development of An Ultrahigh-resolution FF-OCT

4.3.1 Experimental Setup

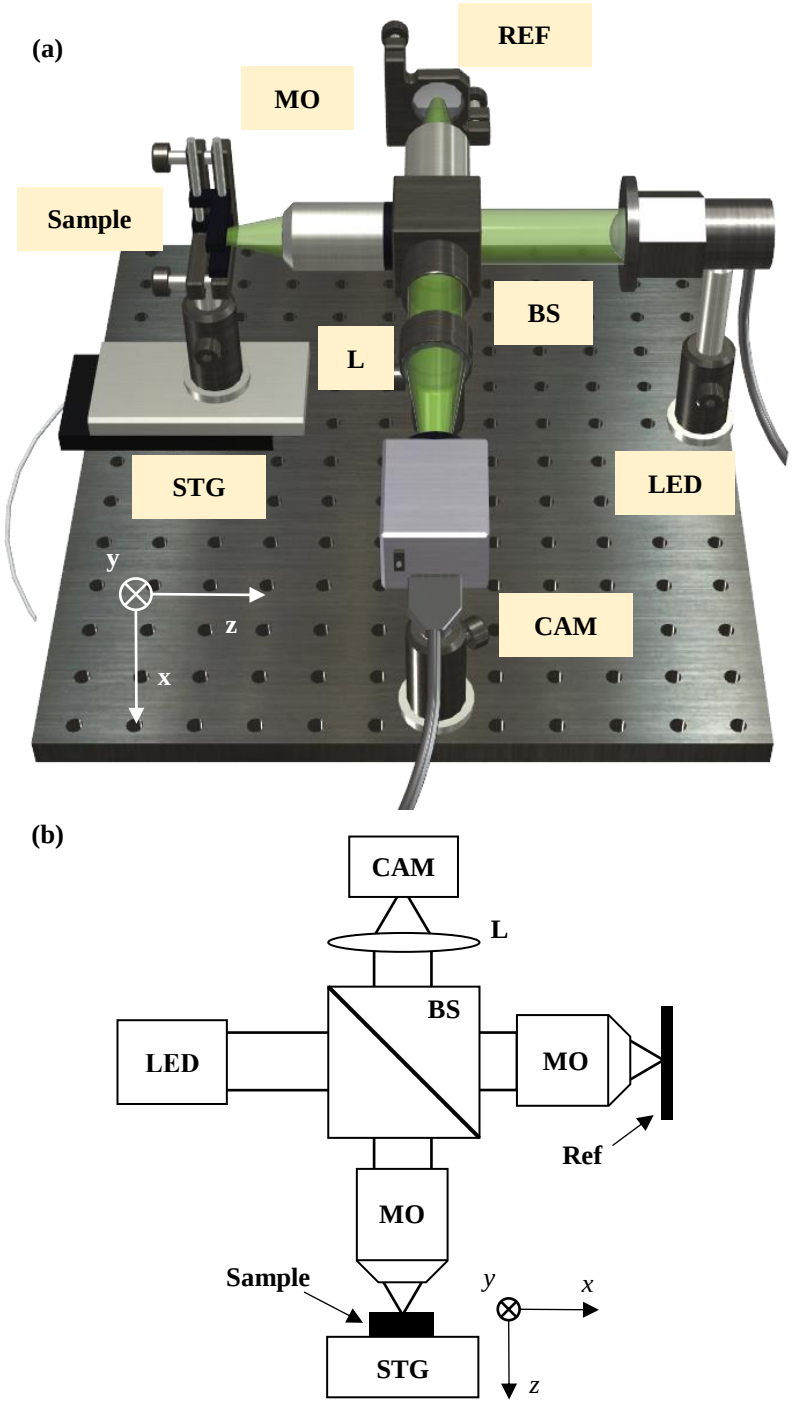

Figure 4.2 The developed Ultrahigh-Resolution (UHR) FF-OCT (a) prototype design and (b) imaging system schematic diagram. LED – broadband Light-Emitting Diode (LED) source; BS – beams splitter; MOs - microscope objectives; Ref – reference mirror; L – plano-convex lens.

Figure 4.2 shows the prototype design (Fig. 4.2(a)) and schematic diagram (Fig. 4.2(b)) of our developed UHR FF-OCT system which was aligned with fewer optical and electrical components as the free of demodulating phases for image reconstruction (detailed discussion in Chapter 4.2.1). The system is driven by a broadband Light-Emitting Diode (LED) source (Thorlabs MBB1L3, wavelength range 470–850 nm). The incident beam is split into the two arms by a non-polarizing 50/50 beamsplitter. There are two nearly identical microscope objectives (10X, 0.3 NA, 16 mm WD, Nikon) operated on both the reference and sample arms, which agrees with a Linnik-typed FF-OCT arrangement. The reflected (mainly from reference arm) light, the backscattered light (mainly from the measured sample) are registered with an sCMOS camera (Zyla 5.5; Andor Technology) after being focused via a plano-convex lens (200-mm focal length). Due to the low temporal coherence of the light source, interference occurs only when the Optical Path Difference (OPD) between the two interferometer arms is within the coherence length. By translating the sample along the z-axis with a high-precision motorised stage (LPS-65, PI MICOS), a stack of original *en-face* images at various scanning depths were acquired that yield a 3D measurement of the sample.

4.3.2 Imaging Performance

A significant advantage of the OCT technique is that it allows the decoupling of axial and lateral resolutions. As the discussion in Chapter 2, the axial resolution of an OCT system is inversely proportional to the FWHM of the light source spectrum (assumed as Gaussian). Although the LED light source used in our FF-OCT system is broadband, the silicon-based detector narrows the effective spectrum due to its spectral responsibility. Therefore, the effective spectrum of the LED source was measured by using a spectrometer (USB 2000+, Ocean Optics). As illustrated in Fig. 4.3(a). the measured central wavelength and the FWHM of the LED source are 610 nm and 190 nm, respectively. Thus, the calculated axial resolution (using Eq. 2.17) is 0.86 μm in air. The axial resolution was measured by imaging a flat mirror. During the measurement, a number of *en-face* images were acquired by axially translating the mirror with a step size of 5 nm, and one of the normalised interferograms was selected to profile the axial response, as the red line shown in Fig. 4.3(b). Its corresponding A-scan signal is reconstructed with the proposed method, the FWHM of which represents the actual axial resolution. As the black line in Fig. 4.2(b), we finally achieved a

resolution of 0.98 µm axially, in which a slight difference with the calculated one is due to convolution.

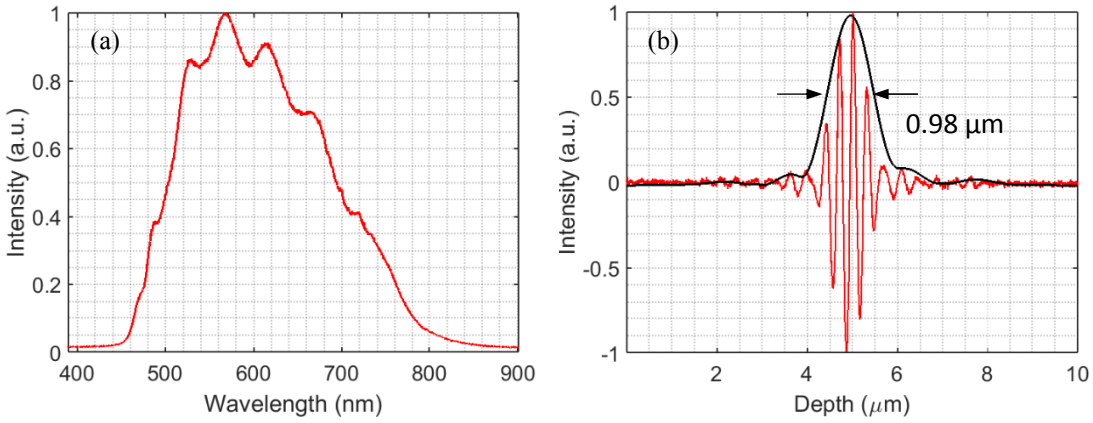

Figure 4.3 Axial resolution of the UHR FF-OCT system. (a) The measured spectrum of the broadband LED light source and the measured central spectral width Δλ are 610 nm and 190 nm, respectively. (b) Measured axial response (black solid line) and its corresponding A-scan signal (red solid line), the Full Width at Half Maximum (FWHM) measured from the signal is 0.98 µm which represents the actual resolution axially.

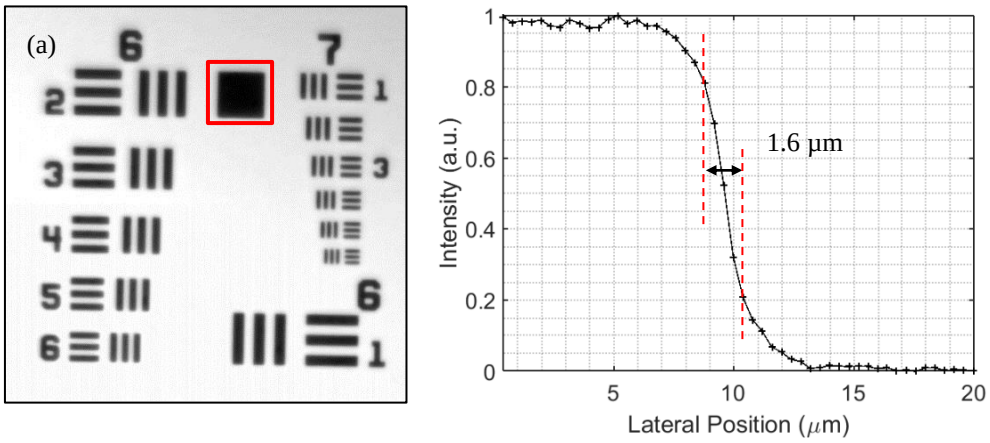

Figure 4.4 Lateral resolution of the UHR FF-OCT system. (a) Standard resolution target USAF 1951. (b) Edge response measured from the square test pattern between group 6 and 7 (enclosed with a red frame in (a)). 20% to 80% width of the edge response represent the actual lateral resolution of 1.6 µm.

The lateral resolution of a diffraction-limited system can be defined as the Point Spread Function (PSF). However, the width of the PSF doesn't track well with human perception and is difficult to measure. The alternative way is to measure the line spread

function (LSF) and the edge response. The LSF is the derivative of the edge response. The width of the LSF can be expressed as the FWHM, and the width of the edge response can be quoted by the 10–90% distance. The distance is usually used to estimate the resolution although it is an underestimation [**10**]. It can be found from the previous study that the 20–80% distance of the edge response has been used as the lateral resolution of an FF-OCT/FF-OCM system [**11**]. The measurement was carried out by using a standard test target USAF 1951, as shown in Fig. 4.4(a). The intensity profile across the square target between groups 6 and 7 (red square in Fig. 4.4(a)) is plotted in Fig. 4.4(b). The actual lateral resolution was measured from the 20% to 80% width of the edge response curve, which is about 1.6 μm.

4.3.3 Defocusing Analysis

In Chapter 2, it has been discussed that Time-Domain OCT (TD-OCT) is free of imaging depth limitation when the attenuation (caused by scattering effects) is disregarded. In FF-OCT, the RI difference between the measured sample and the used objective lens will introduce a shift between nominal focus position and actual focus position. When this shift turns to be larger than the depth of field, the imaging depth is limited, and the image quality is degraded. Figure 4.5 shows the induced shift by the RI mismatch, where the imaging beam goes into a sample with an angle of θ_1, and n_1 represents the RI of the air. The sample has its RI value of n_2 ($n_2 > n_1$). As a result, the incident light is focused on the position (the green circle in Fig. 4.5) with a refraction angle θ_2, which is deeper than the nominal focus point (the red circle in Fig. 4.5). According to Snell's Law, the refraction relationship can be expressed as

$$n_1 \sin\theta_1 = n_2 \sin\theta_2 \tag{4.10}$$

and the NA of the microscope objective lens used in the sample arm can be written as

$$\begin{aligned} NA &= n_1 \sin\theta_1 \\ NA &= n_2 \sin\theta_2 \end{aligned} \tag{4.11}$$

Using x represents the distance between the normal plane of the light and the optical axis and using z represents the distance between the surface of the sample (the blue lines in Fig. 4.5) and the actual focus plane (the red lines in Fig. 4.5), we can derive

$$\tan\theta_2 = \frac{x}{z} \tag{4.12}$$

By translating the sample towards the objective with a depth Δz, the distance from the new normal plane of the light to the previous one correspondingly changes, which is denoted as Δx in Fig. 4.5. In addition, the distance between the sample surface and the actual focus plane after the axial movement is denoted as z'. θ_1 and θ_2, therefore, are satisfied as

$$\begin{aligned} \tan\theta_1 &= \frac{\Delta x}{\Delta z} \\ \tan\theta_2 &= \frac{x+\Delta x}{z'} \end{aligned} \tag{4.13}$$

After making relevant substitutions, it can be derived that

$$z' = z + \Delta z \frac{\tan\theta_1}{\tan\theta_2} \tag{4.14}$$

The actual shift within the sample $\Delta z'$ can be expressed as

$$\Delta z' = z' - z = \Delta z \frac{\tan\theta_1}{\tan\theta_2} \tag{4.15}$$

and the actual focus shift Δf is therefore

$$\Delta f = \Delta z \frac{\tan\theta_1}{\tan\theta_2} - \Delta z \tag{4.16}$$

Given that the sample is displaced with a fixed scanning step Δz from the plane of zero path difference, which is also known as the coherence plane (the solid red line in Fig. 4.5), we can derive a series of focus shifts as the function of the NA of the objective and the RI of the sample by substituting Eq. 4.11 to Eq. 4.16

$$\Delta f(NA, n_1, n_2) = \mathrm{m}\Delta z \left(\frac{\tan\left(\sin^{-1}\frac{NA}{n_1}\right)}{\tan\left(\sin^{-1}\frac{NA}{n_2}\right)} - 1 \right), \ \mathrm{m}=0,1,2 \ldots \mathrm{m} \tag{4.17}$$

In contrast to the focal plane (forward moving to the deeper position of the sample), the plane of zero path difference is shifted backwards, and its corresponding shift distance ΔCoh can be written as

$$\Delta Coh(n_1, n_2) = -m\left(\Delta z \frac{n_1}{n_2}\right), \ \mathrm{m}=0,1,2 \ldots \mathrm{m} \tag{4.18}$$

where the minus sign indicates the direction. Note that the relationship described in Eq. 4.17 and Eq. 4.18 is important in a UHR FF-OCT system, especially for those which

employs high-NA microscope objectives. Only when the $|\Delta f + \Delta Coh|$ is smaller than the DOF, the imaging quality can be guaranteed.

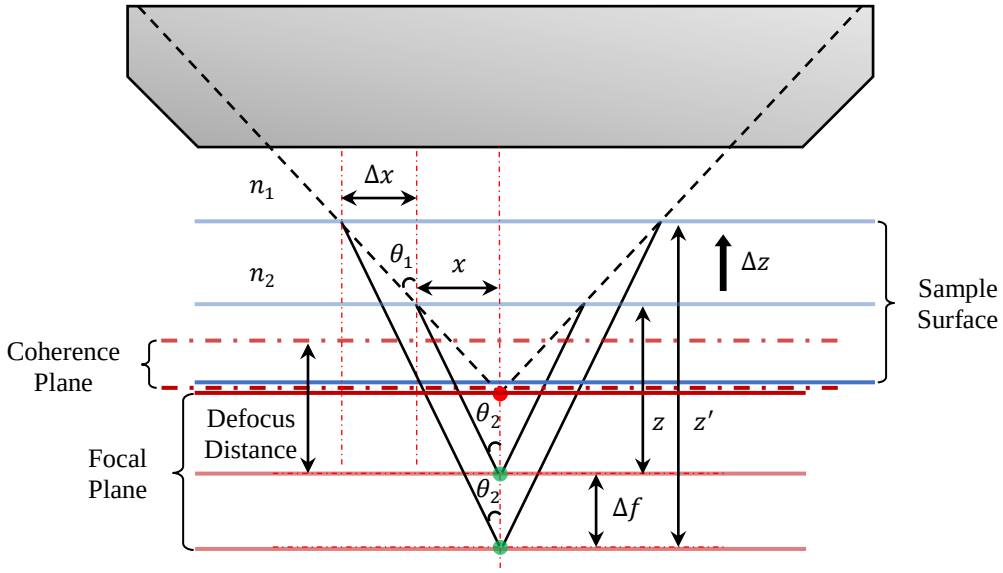

Figure 4.5 FF-OCT defocusing simulation. FF-OCT defocusing phenomenon caused by using a high Numerical Aperture (NA) microscope objective. The geometry demonstrates that the focal plane shift forward and the coherence plane shift backwards when the imaging beam focusing inside the sample which has a Refractive Index (RI) value of n_2 (>1).

4.4 Material

4.4.1 Paracetamol Tablet

Paracetamol is the most common group of drugs known as simple non-opioid analgesics [**12**]. In the UK, many pharmaceutical companies manufacture 500-mg paracetamol tablets, which are sold over the counter. In this study, the coating thickness, of two randomly selected GSK Panadol tablets (denoted by P-S1 and P-S2), two generic paracetamol tablets from Aspar Pharmaceuticals (St Albans, UK) (denoted by A-S1 and A-S2), and Boots Pharmaceuticals (Nottingham, UK) (denoted by B-S1 and B-S2), were measured. It should be noted that all the measured paracetamol tablets are sourced directly from over-the-counter UK pharmacy stores. The main Active Pharmaceutical Ingredient (API) of the three product is 500-mg paracetamol. Opadry white and carnauba wax are used for tablet coating of GSK's Panadol. We anticipate that the coating serves the purpose of protecting the API against light and moisture.

Table 4.2 Paracetamol tablets from different suppliers.

Paracetamol Suppliers	Front Side	Back Side
ASPAR		
Boots		
GSK (branded)		

Table 4.2 lists the photographs taken from different suppliers' paracetamol tablet products on 1 × 1 mm^2 grid background. Aside from minor physical differences, such as shape, marking, there are no visible differences such as colour or embossing thus making product differentiation difficult. As OCT technique has already shown the capability of analysing pharmaceutical film coatings, it can also be extended to the detection of thin coatings (i.e. the coating thickness of fewer than ten microns), which may aid in product differentiation.

4.4.2 Detrol Micropellet

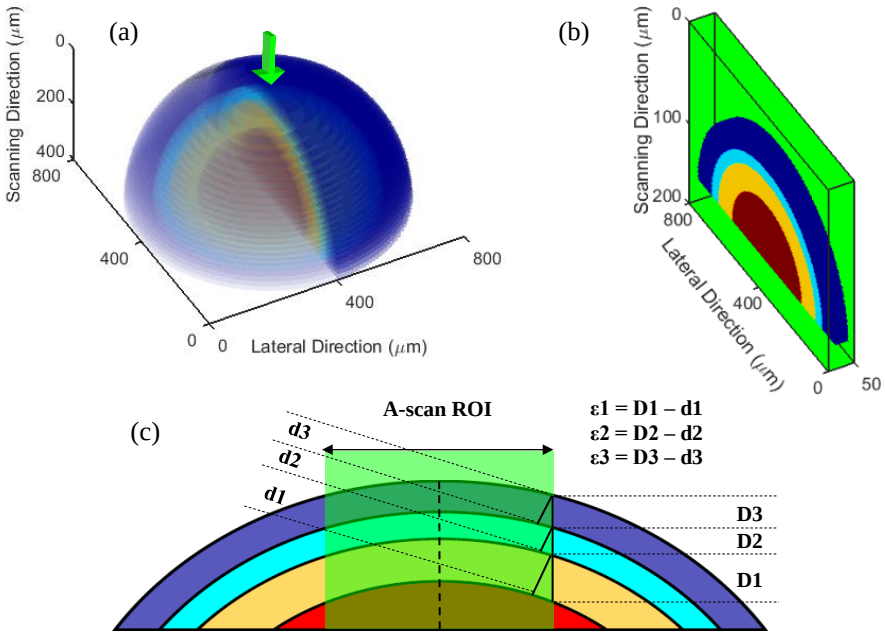

Figure 4.6 Schematic diagram of measured micropellet and Region of Interest (ROI) used for coating thickness analysis. (a) Schematic of micropellet diagram: Blue area – outer coating layer; Cyan area – intermediate coating layer; Yellow area – inner coating layer; Red area – pellet core. (b) Central volume ROI: this ROI is extracted from the central region of the 3D pellet volume as green arrow denoted in (a), a number of B-scan images are then extracted from this ROI for coating structure analysis. (c) A-scan ROI: A-scan signals contained in this region are averaged for calculating mean coating thickness. Given that thicknesses of the three coatings are 20 (outer), 10 (intermediate) and 25 μm (inner), thickness errors resulted from the selected ROI, ε1 (outer), ε2 (intermediate) and ε3 (inner), are calculated as 0.15, 0.08 and 0.23 μm, respectively.

Micropellets are pharmaceutical dosage form with a size smaller than 1 mm and are of great interest in the pharmaceutical industry. Not only do they offer flexibility in dosage form design such as pellet-filled capsules and multiple-unit pellet system tablets, but they can also be used to improve the safety and efficacy of bioactive agents [**13**]. Depending on the required dissolution profile, the API can be contained in the pellet core, or directly coated onto a core bead typically made of sugar or polymer excipients. The use of enteric coating or complex layer structures on pellets provides a mechanism to direct and extend the release profile in order to achieve full therapeutic efficiency

[**14**]. Achieving a prescribed coating amount or thickness (normally from tens to hundreds of microns) and uniformity on the dosage forms is therefore of paramount importance [**15**].

Figure 4.6(a) shows the schematic diagram of a simulated pellet based on the physical dimension of the pellet. In particular, the pellet has a diameter of approximately 800 μm covering an effective imaging area of 840 × 840 pixels (i.e. 1.05 μm/pixel). Three film coating layers, yellow, cyan and blue, represent the core, inner, intermediate and outer coatings, respectively, and red represents the pellet core. In order to analyse the coating structures, we extract several B-scan images from a Region of Interest (ROI), which was selected from the central volume of the OCT datacube (denoted with the green arrow in Fig. 4.6 (a)). Figure 4.6(b) shows the schematic of the volumetric ROI with its dimension of 50 μm × 800 μm × 200 μm. Moreover, in each selected B-scan image, we averaged 100 neighbouring A-scan signals from an A-scan ROI near to the apex of the pellet surface for the analysis of coating thickness, as the schematic shown in Fig. 4.6(c). Given that the thicknesses of the outer, intermediate and inner coatings are 20 μm, 10 μm and 25 μm, the thickness errors that could be introduced by a surface curvature of the A-scan ROI are calculated as 0.15 μm for the inner coating layer, 0.08 μm for the intermediate coating layer and 0.23 μm for the outer coating layer, respectively. Nonetheless, this is still within an acceptable range (i.e. less than 1% thickness error for each coating).

4.5 Film Coating Imaging of Paracetamol Tablets

FF-OCT Measurement

Measurements on the tablet samples were performed using the proposed UHR OCT system with a scanning distance of 100 µm in air. It should be noted that even though B-scan images at the centre of the tablets are shown, the system can, in principle, achieve an illumination area of approximately 1-mm diameter. A 3D datacube (size: 10 µm × 750 µm × 100 µm) consisting of 8 raw B-scan data were acquired for each measured tablet. To set a narrow rectangular imaging area, a frame rate of 1000 fps was achieved by the camera and the total acquisition time for the volumetric data was approximately 10 s.

Result and Discussion

Figure 4.7 shows the representative B-scan images over the depth range of up to 60 µm for an estimated coating RI value of 1.5 when assuming polyvinyl alcohol (PVA) as the coating polymer. From the B-scan images of the generic suppliers shown in Figs. 4.7(a–d), there are no resolvable coating structures as opposed to a thin coating layer in the B-scan images of the branded Panadol tablets, shown in Figs. 4.7(e) and 4.7(f). The corresponding A-scan waveforms (shown in Fig. 4.8) confirm a weak air/coating interface for branded Panadol but not for generic products. The first peak, in this case, represents the air/coating interface followed by a major peak for the coating/tablet core interface. The high lateral resolution of the system can additionally resolve particulates adsorbed to the tablet surface on generics, which are notably absent on the branded product, thus, implying branded products have a smoother surface finish. These observable physical differences, therefore, suggest the presence of a thin coating layer could be used as an indicator to discriminate branded Panadol tablet from generics.

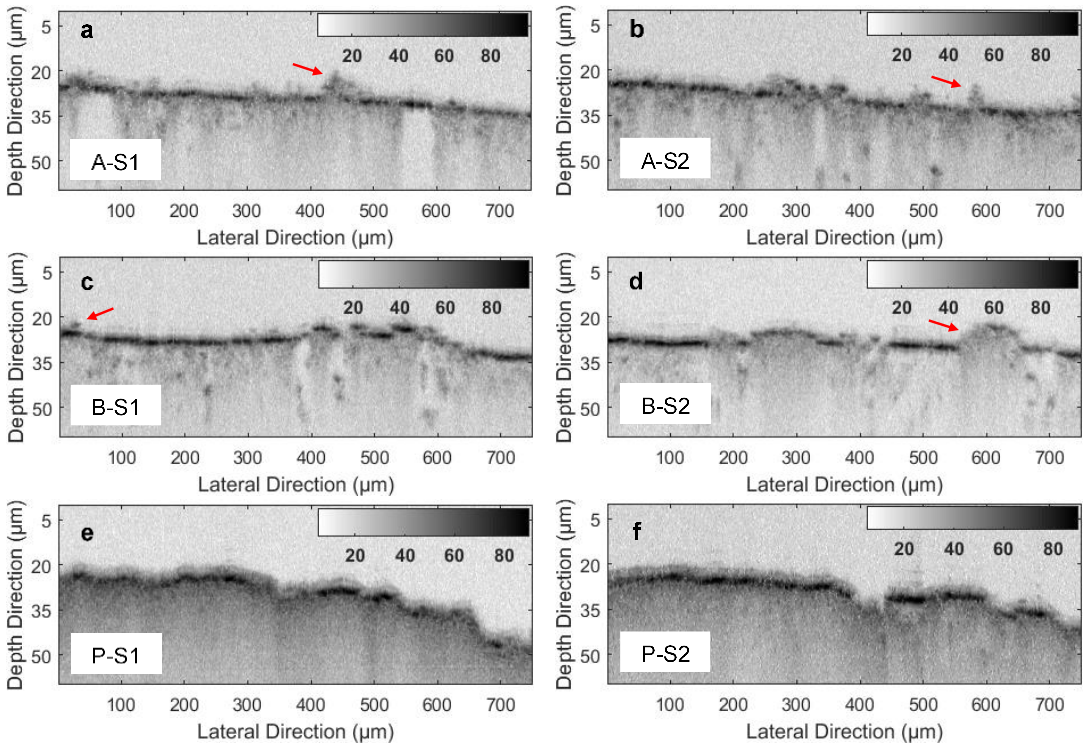

Figure 4.7 Differentiation between generic paracetamol tablet and Panadol tablet using the UHR FF-OCT cross-sectional (B-scan) image. (a) & (b) B-scan images of two ASPAR paracetamol tablets (A-S1 and A-S2). (c) & (d) B-scan images of two Boots paracetamol tablets (B-S1 and B-S2). Red arrows point out the particulates on the sample surface. (e) & (f) B-scan images of two GlaxoSmithKline (GSK) Panadol tablets (G-S1 and G-S2), where a thin ghostly layer can be resolved.

It can be found that the B-scan images (Fig. 4.7) taken from the Panadol tablets show one very weak RI change along the surface, followed by a rather stronger one. The corresponding A-scan waveforms (Fig. 4.8) of going into the tablets confirm the weak air/coating interface as a comparison to the non-coating results from the generic tablets. We speculate that the first peak represents the beginning of the coating, although we currently do not understand why this contrast at the proposed air/coating interface is relatively weak as we would have expected a stronger RI change at this interface. The A-scan waveform, either from the generic or branded tablet, demonstrate a similar decay within the tablet core. In addition to scattering encountered, this is also due to the absorption of the imaging beam in accordance with Beer-Lambert law. In contrast, there is no significant decay within the region between the first two peaks in the A-scan waveforms of the Panadol tablets, thus supporting the observed coating structure. As

for the imaged coating, a possible reason is that the ingredient/s of the coating material may make it translucent to the imaging beam. In the published study [**16**], it has been found that coating semi-transparent for OCT measurement is very much dependent on the pigment type, coating formulation and tablet core properties, as well as the coating process. The coating can become marginally visible to OCT if the coating material only contains talc and pigment. Note that a similar result on coating was also reported previously by Mauritz *et al*. [**17**], and further study is still needed to fully explore the underlying mechanism.

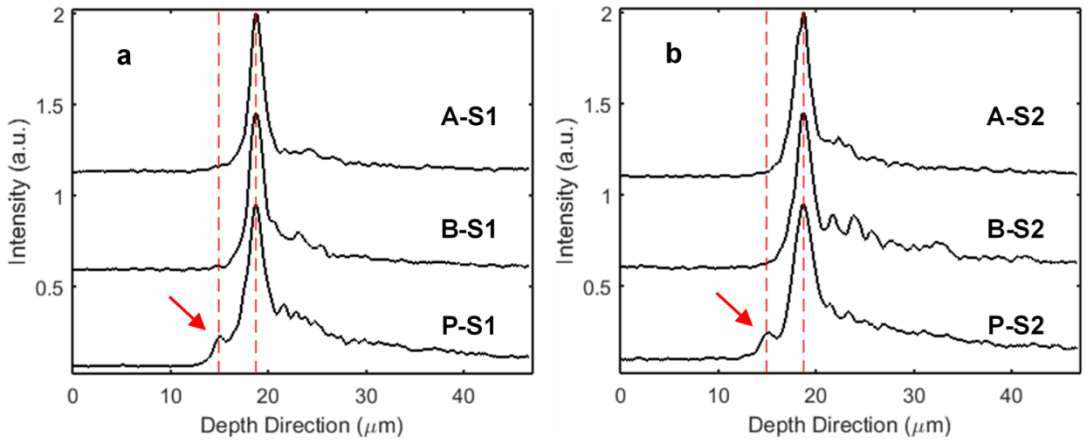

Figure 4.8 Representative A-scan signals taken from the B-scan images in Figure 4.7. (a) A-scans including measured generic paracetamol samples (A-S1 and B-S1) and GSK's Panadol sample (P-S1). (b) A-scans including measured generic paracetamol samples (A-S2 and B-S2) and GSK's Panadol sample (P-S2). The red dotted lines mark the characteristic peaks, and the distance between them provides coating thickness information.

Coating Thickness Analysis

As a more thorough illustration of determining tablet coating thickness, it is aimed at finding the boundaries using an automated image segmentation approach. If the analysis is restricted to a single example, methods such as Otsu thresholding could be used. However, such approaches are not reliable for OCT segmentation due to their lack of robustness to noise or variation of contrast within and between images. Thus, a fast graph-based image segmentation algorithm is designed to automatically obtain the coating thickness from B-scan images of the Panadol tablets. Here, to detect the weak signal from the air/coating interface, a suitable parametric energy function is determined to describe the edges of the tablet and coating material, taking scattering

into account. This energy function calculates a trade-off between gradients and intensity, determined by parameters α_i and β. The function is given by

$$E[u(x)] = \beta\sum_{i=1}^{3} a_i - a_1\frac{\partial u(x)}{\partial x_1} - a_2\frac{\partial u(x)}{\partial x_2} - a_3 u(x), \quad x = (x_1, x_2, x_3)^T \tag{4.19}$$

where $u(\boldsymbol{x})$ denotes the spatial intensity function, x_1 denotes the depth direction, x_2 and x_3 denote the lateral directions. Two collections of parameters were used to determine the different boundaries; it is found $(\alpha_1, \alpha_2, \alpha_3, \beta) = (10^{-2}, 10^{-2}, 1, 1)$ were suitable for finding the tablet-coating interface due to the strong scattering signal found there, and $(\alpha_1, \alpha_2, \alpha_3, \beta) = (-1, -4 \times 10^{-1}, -10^{-2}, 0)$ for the outer surface of the tablet coating. The image was pre-smoothed with a median filter of window pixel size $7 \times 7 \approx 0.07 \times 5.6$ µm. The energy function then was minimised using a graph-search approach with dynamic programming using a 7×7 search region in order to obtain contours across the image which best fit the air/coating and coating/tablet core interfaces. Using this method and the estimated RI value of 1.5, mean coating thicknesses of 4.6 µm and 3.5 µm, respectively, were calculated from the B-scans (shown in Fig. 4.9) of the two tablets (PS-1 and PS-2). This is in close agreement with the estimated thickness of approximate 4 µm by using A-scan signal based method [**18**].

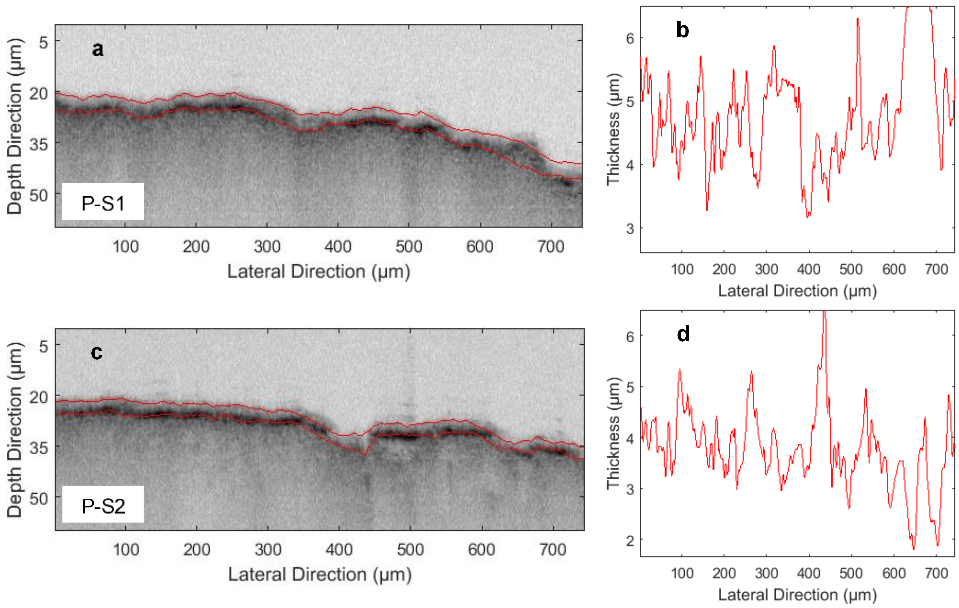

Figure 4.9 Coating thickness analysis using segmentation on the B-scan images of the GSK's Panadol tablet samples, P-S1 (a) and P-S2 (c). The detected air/coating and coating/tablet core interfaces are highlighted in red. (b) and (d) are their corresponding coating thickness distribution histograms.

4.6 Film Coating Imaging of Detrol Micropellets

FF-OCT Measurement

The measurement was performed with the proposed UHR FF-OCT with a depth scanning step of 5 nm, and the total travel distance of the stage was 200 µm. The achieved frame rate of the system was 100 fps, which enables a data acquisition time of 3D imaging in 7 minutes. The original 3D data was then reconstructed to the 3D OCT datacube by using the proposed reconstruction method. After resampling, the size of the OCT datacube involves 840 × 840 × 200 pixels, which corresponds to a practical dimension of 800 × 800 × 200 μm^3.

XµCT Measurement

The XµCT measurement was performed on a Skyscan 1172 (control software1172 XµCT Control Program v1.5; Bruker, Kontich, Belgium). Reconstruction was performed by utilising the program NRecon (Bruker; v1.6.9.8) on a single PC with graphics processing unit-accelerated reconstruction (Windows 7 64-bit workstation, 2 Intel Xeon X5647 with 4 core each, 48 GB RAM, NVIDIA Quadro 4000 with 256 cores), yielding 3D data with an isotropic voxel size of 0.95 µm. The data acquisition time was 1.5 hours, and the image reconstruction took 0.5 hours for 125 slices of 1208 × 1208 pixels.

Result and Discussion

Figure 4.10 shows two B-scan images extracted from the volumetric ROIs on the OCT and XµCT datacubes, where the B-scan image corresponding to the OCT result (see Fig. 4.10(a)) is displayed in the decibel over the imaging scan range of 200 µm in air, and the XµCT B-scan image (see Fig. 4.10(b)) covers an imaging depth up to 120 µm in air. XµCT modality is based on differential absorption of X-ray by different coating material to enable distinction between different inner structures of the pellet sample. In contrast, OCT is based on detection of backscattering signals from different coating materials and pellet core to enable cross-sectional imaging, which is contributed by refractive index mismatch between different coating layers and between coating to pellet core. In order to obtain the inner structures at the same position within the pellet sample by the FF-OCT and XµCT, the axial scan distance of the FF-OCT has to be

longer than the XµCT due to the refraction of different coating materials. Nevertheless, the imaging speed of the FF-OCT modality (approximately 7 minutes) is still much faster than the XµCT (1.5 hours).

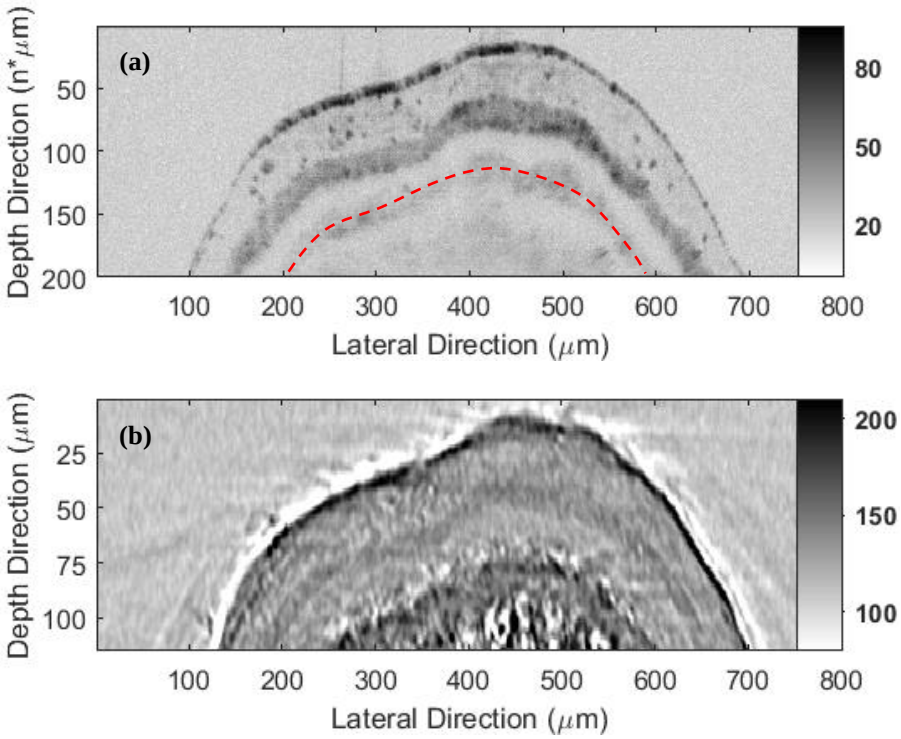

Figure 4.10 Coating microstructure of the micropellet sample. The same pellet is imaged and characterised by (a) FF-OCT B-scan image with decibel unit and (b) X-ray Micro Computed Tomography (XµCT) B-scan image with 8-bit grey scale.

In both the FF-OCT and XµCT B-scan images, black corresponds to the strongest reflection/backscattering signal and white corresponds to the weakest. It has been demonstrated from Fig. 4.10 that approximately identical inner structures are featured in both the FF-OCT and XµCT results. Sharp signal intensity changes firstly occur from the air/pellet interface, and the weakened signals below the outermost interface characterise the outer coating layer. In contrast, the intermediate coating (the middle black region in Figs. 4.10(a) and 4.10(b)) shows a denser and thinner coating structure, in which the intensity of the reflected/backscattered signals is increased. Obvious intensity change can again be noticed from the interface of the intermediate/inner coatings, indicating that the inner coating layer is optically rarer than the intermediate one. In addition, the increase in signal intensity within the inner coating layer may be due to the dispersion of the coating material (as highlighted from the areas above the

red dotted lines in Fig. 4.10(a)). As for the pellet core, the OCT results can only provide an outline of the pellet core since the imaging beam has propagated within the pellet to be close to its maximum detection depth. Note that, this is because of the UHR FF-OCT with a high lateral resolution achieved by the high-NA objective (NA: 0.3), which results in defocusing at deeper positions of the measured sample (see section 4.3.3). It can be compensated by introducing more electrical components to adjust the reference arm to allow the imaging plane to be within the narrow DOF range.

In the previous work [**2**], the coating thickness of a pellet sample with two layers was determined by assuming the same RI (n) in all image analysis. However, the differences in n values cannot be ignored when investigating a pellet with more complex coating structures, such as the sample used in this work, where the thinner intermediate coating layer has an obviously higher n value than the other layers. It is essential to estimate the n value for each coating layer. This can be achieved by introducing the XµCT measurement result, and the n value of each layer can be estimated as

$$n = \frac{d_{OCT}}{d_{X\,\mu CT}} \tag{4.20}$$

where d_{OCT} is the mean thickness measured from the OCT result, $d_{X\mu CT}$ is the mean thickness measured from the XµCT result. Figure 4.11(a) shows an averaged OCT A-scan signal in decibel, while Fig. 4.11 (b) shows an averaged XµCT A-scan signal. They are obtained from the aforementioned A-scan ROI in their corresponding OCT (Fig. 4.10 (a)) and XµCT (Fig. 4.10 (b)) B-scan images. It should be pointed out that the masked areas in Fig. 4.11 (a) and 4.11 (b) represent the pellet core part which is excluded from the analysis due to the significantly attenuated signal in FF-OCT result lead by the imaging depth limit.

The thickness of the outer coating layer (denoted by a blue doughnut in Figs. 4.11(a) and 4.11(b)) was measured as 44 µm from the OCT result and 23.6 µm from the XµCT result. The RI value of the outer coating (n_1) was then calculated as 1.86 accordingly. For the intermediate coating layer, denoted by a cyan doughnut in Figs. 4.11(a) and 4.11(b), the coating thickness measured from the OCT result was 18.2 µm while the thickness of 9.5 µm was measured from the XµCT result. As a result, the RI value of the intermediate coating layer (n_2) was calculated as 1.92. In addition, the measured inner coating (denoted by a yellow ring in Figs. 4.11(a) and 4.11(b)) thickness was 45.9

µm from the OCT A-scan signal and 25.1 µm from the XµCT A-scan signal, which corresponds to a calculated value of 1.83 as the RI of the inner coating layer (n_3). Note that, this represents the non-destructive determination of the RI values of the pellet coatings at its native state (i.e. intact coatings of pellets), while the spectroscopy method can only be used to measure the RI of coating materials.

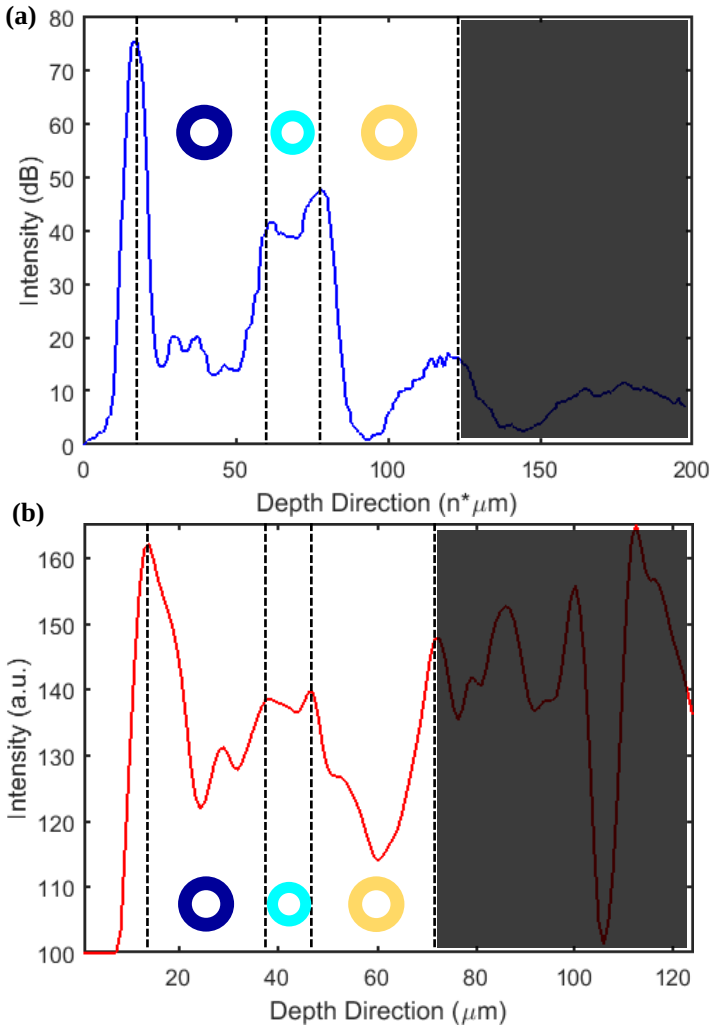

Figure 4.11 Averaged A-scan signals of the UHR FF-OCT and the XµCT. (a) UHR FF-OCT A-scan signal and (b) XµCT A-scan signal are extracted from the A-scan ROIs in the FF-OCT B-scan image (Fig. 4.10(a)) and the XµCT B-scan image (Fig. 4.10(b)). The blue, cyan and yellow rings denote the outer, middle and inner coating layers, respectively. The masked areas represent the pellet core part which is excluded from the analysis.

To determine coating thickness, previous studies employed A-scan based analysis. We firstly adopt this standard way to obtain a set of thickness results, where a number of

averaged A-scan signals within the volumetric ROI were used. Figure 4.12 shows the measured coating thickness of each coating layer and makes a comparison with the XµCT results. The number of 1, 2 and 3 in the *x* axis respectively represents the outer, intermediate and inner coating layers. Specifically, the outer layer has a mean thickness of approximately 22.2 µm determined from the OCT results, while the thickness of 21.3 µm is obtained from the XµCT one. For the thinner intermediate layer, the mean thickness of 11.2 µm corresponds to the OCT result, and 9.6-µm thickness is determined from the XµCT result. For the inner coating layer, mean thickness of 28.1 µm and 28.9 µm are respectively measured from the OCT and XµCT results. We conclude that the UHR FF-OCT result has a good agreement with those from XµCT.

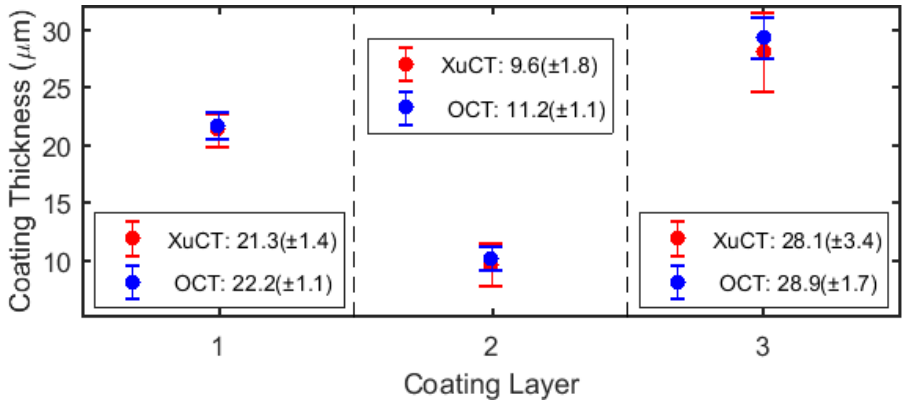

Figure 4.12 Comparison of the coating thickness measured from the UHR FF-OCT and the XµCT result. The number of 1, 2, and 3 in the *x* axis represents the outer, middle and inner coating layers, respectively.

Figures 4.13(a–e) displays a series of reconstructed *en-face* images taken by the UHR FF-OCT at increasing depths. The dark and white areas in turn appear, indicating that different coating layers with changes in RI can be clearly observed. The red arrows in Figs. 4.13(a–e) highlighted the typical areas, where the three coating layers and the pellet core start to appear. The coating thickness could then be estimated as 21 µm for the outer coating layer, 11 µm for the intermediate coating layer and 29 µm for the inner coating layer. This provides a cross-validation with the result derived from the A-scan signal based analysis. As a comparison, Figs. 4.13(f–j) show a set of XµCT *en-face* images at the same positions as the OCT ones. Note that, black corresponds to denser coating structures in the same grey scale order as the OCT. Again, a good agreement can be found between them.

The B-scan images and the *en-face* images taken by the UHR FF-OCT system are capable of resolving the fine internal structures of the micropellet. The traditional coating thickness analysis (A-scan signal based) method can provide partial (around the apex region) thickness information of a measured pellet sample [**2**]. However, a more significant aspect, such as intra-pellet coating uniformity, has not been presented along with an FF-OCT technique. To achieve this, the proposed 3D image segmentation technique is used to define 2D coating thickness maps. Considering that the inner coating layer is blurred due to the defocusing effect at deeper positions, the 3D thickness analysis was carried out at the first two coating layers. Figure 4.14(a) shows the segmented contours of the first two layers, where a part of data has been removed for display. Three interfaces are marked with the colour blue, cyan and yellow, which is corresponding to the air/pellet interface, the outer/intermediate coating interface and the intermediate/inner coating interface, respectively. The coating thickness maps are then generated, as shown in Figs. 4.14(b) and 4.14(c), a false colour scale is used to map the thickness variation encompassing a range from 0 to 25 µm. The thickness of the outer coating layer can be seen to vary mainly from 15 to 22 µm, and the thickness of the intermediate coating layer varies from 8 to 12 µm. To obtain the eventual thickness, the coating thickness maps are summarised as histograms of a number of pixels versus pixel thickness in Figs. 4.14(d) and 4.14(e). Note that, all the results in Fig. 4.14 have taken into account the derived RI value of each coating layer. The mean thickness of the outer coating layer is calculated as 18.6 µm with a thickness standard deviation of ± 2.6 µm and the mean thickness of the intermediated coating layer is calculated as 11.1 µm with a standard deviation of ± 1.9 µm.

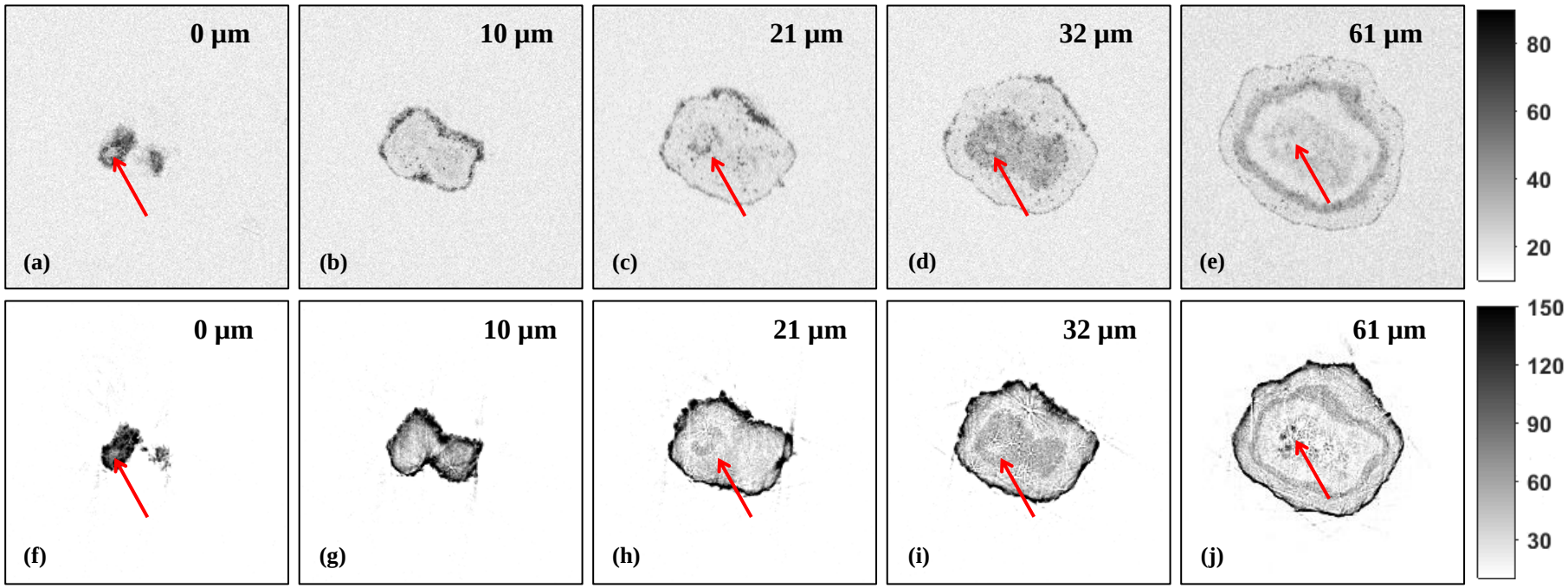

Figure 4.13 *En-face* images extracted from the UHR FF-OCT and the XµCT measurement at the same depth position for comparison. (a)–(e): *En-face* images of OCT displayed in decibel. (f)–(j): *En-face* images of XµCT displayed 8-bit grayscale. The red arrows in the figure highlight the area where the three pellet coatings, as well as the pellet core, start to appear, and the coating thickness can be determined by the difference between their corresponding depth positions.

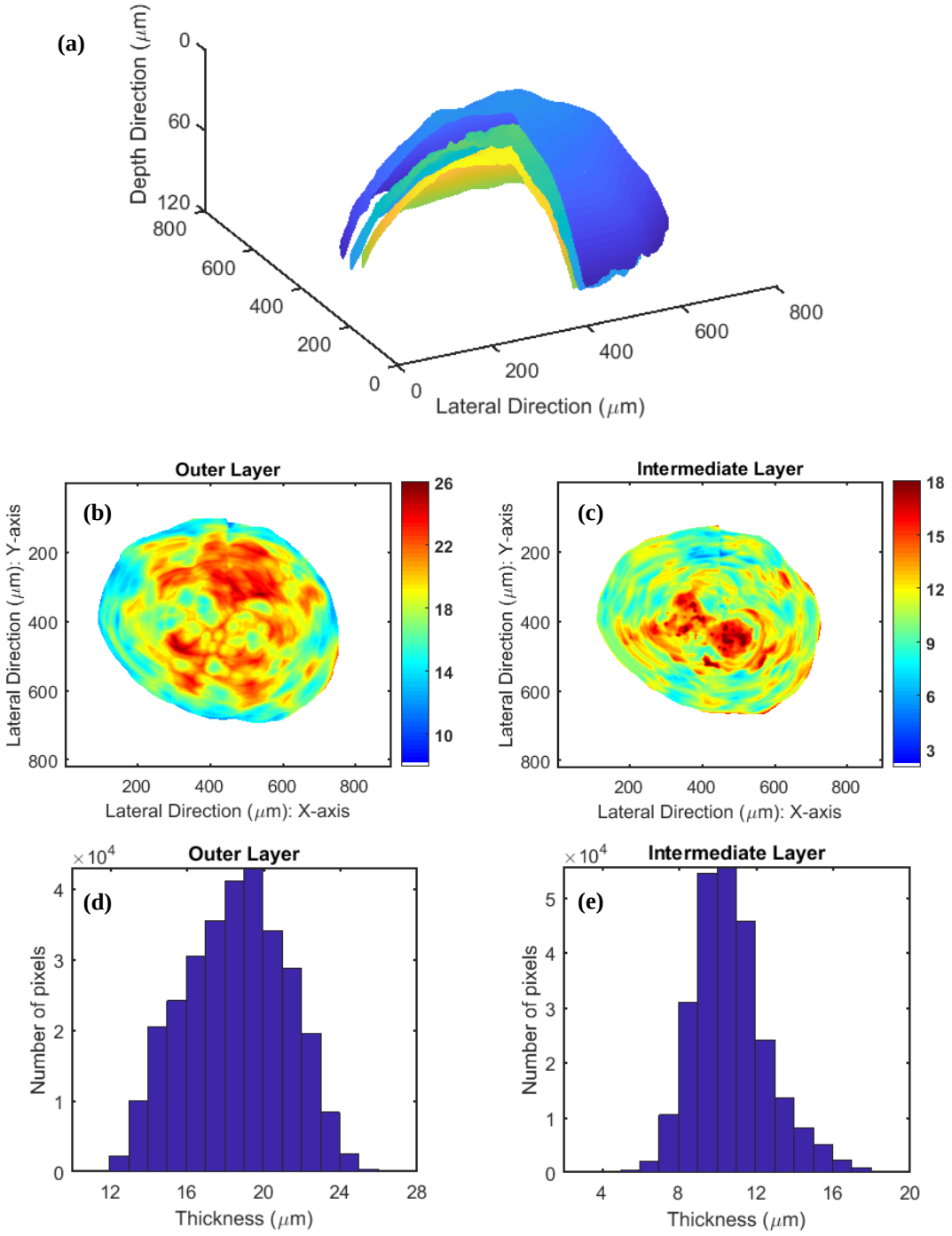

Figure 4.14 Coating thickness variation analysis based on the proposed Three-Dimensional (3D) segmentation method. (a) Segmented pellet result focusing on the first two coating layers. The blue, cyan and yellow colour represent the air/pellet interface, the outer/intermediate coating interface and the intermediate/inner coating interface, respectively. (b) and (c) Two-Dimensional (2D) thickness maps of the outer and intermediate coatings, where the colour scale is in μm. (d) and (e) Coating thickness distribution histograms corresponding to the outer and intermediate coating layers.

4.7 Conclusion

To summarise, in this chapter, an FF-OCT system with an ultrahigh resolution (i.e. 1 µm axially and 1.6 µm laterally) has been developed to characterise the thin film coating applied in GSK's Panadol tablet products and multi-layer micropellets (diameter is approximately 800 µm). In contrast to the standard time-domain FF-OCT systems where measurements were carried out using phase stepping or phase shifting methods, a continuous measurement approach is proposed. The research has shown that the measurement can continuously operate without employing any components to generate phase information for retrieving OCT images. The whole system configuration is therefore similar to the compact arrangement of "vertical scanning interferometer" widely used for measuring surface profiles with demonstrated flexibility in industrial environments. The achieved axial resolution of about 1 µm enables the high-quality B-scan imaging, and the high lateral resolution of 1.6 µm allows high-quality *en-face* images to be captured simultaneously.

Consequently, a thin coating structure with the thickness of approximately 4 µm was resolved from GSK's Panadol tablets, thus, allowing us to differentiate GSK's branded Panadol tablets from other generic paracetamol products. The proposed system also characterised the micropellet with multi-layer coating structures. By introducing the 3D image segmentation technique, the coating thickness map and the coating thickness distribution can be obtained automatically. This, as an analysis software integrated with the proposed UHR FF-OCT system, provides, therefore, a complete solution for the study of the pharmaceutical micropellets even with multiple coating layers.

References

[1] Y. Dong, H. Lin, V. Abolghasemi, L. Gan, J. A. Zeitler, and Y.-C. Shen, "Investigating intra-tablet coating uniformity with spectral-domain optical coherence tomography," Journal of Pharmaceutical Sciences, vol. 106, no. 2, pp. 546-553, 2017.

[2] C. Li, J. A. Zeitler, Y. Dong, and Y.-C. Shen, "Non-destructive evaluation of polymer coating structures on pharmaceutical pellets using full-field optical coherence tomography," Journal of Pharmaceutical Sciences, vol. 103, no. 1, pp. 161-166, 2014.

[3] A. Dubois, and A. C. Boccara. Full-Field Optical Coherence Tomography. In: Drexler W, Fujimoto JG, editors. Optical Coherence Tomography. Berlin, Heidelberg: Springer; 2008. p. 565–91.

[4] O. Sasaki, H. Okazaki, and M. Sakai, "Sinusoidal phase modulating interferometer using the integrating-bucket method," Applied Optics, vol. 26, no. 6, pp. 1089-1093, 1987.

[5] A. Dubois, K. Grieve, G. Moneron, R. Lecaque, L. Vabre, and C. Boccara, "Ultrahigh-resolution full-field optical coherence tomography," Applied Optics, vol. 43, no. 14, pp. 2874-2883, 2004.

[6] E. Bordenave, E. Abraham, G. Jonusauskas, N. Tsurumachi, J. Oberle, C. Rulliere, P. E. Minot, M. Lassegues, and J. S. Bazeille, "Wide-field optical coherence tomography: imaging of biological tissues," Applied Optics, vol. 41, no. 10, pp. 2059-2064, 2002.

[7] A. Dubois, L. Vabre, A.-C. Boccara, and E. Beaurepaire, "High-resolution full-field optical coherence tomography with a Linnik microscope," Applied Optics, vol. 41, no. 4, pp. 805-812, 2002.

[8] M. Akiba, K. Chan, and N. Tanno, "Full-field optical coherence tomography by two-dimensional heterodyne detection with a pair of CCD cameras," Optics Letters, vol. 28, no. 10, pp. 816-818, 2003.

[9] M. Sato, T. Nagata, T. Niizuma, L. Neagu, R. Dabu, and Y. Watanabe, "Quadrature fringes wide-field optical coherence tomography and its applications to biological tissues," Optics Communications, vol. 271, no. 2, pp. 573-580, 2007.

[10] S. W. Smith, "The Scientist and Engineer's Guide to Digital Signal Processing", 2nd ed. California Technical Publishing, San Diego, CA, 1999.

[11] T. Anna, T.W. Chang, C.M. Lai, A. Chiou, and W.C. Kuo, "A Feasibility Study of Broadband White Light Emitting Diode (WLED) Based Full-Field Optical Coherence Microscopy (FF-OCM) Using Derivative-Based Algorithm". IEEE Photonics Journal, vol. 9, no. 2, pp.1-13, 2017.

[12] L. F. Prescott, "Paracetamol: past, present, and future," (in eng), American Journal of Therapeutics, vol. 7, no. 2, pp. 143-147, 2000.

[13] S. Abdul, A. V. Chandewar, and S. B. Jaiswal, "A flexible technology for modified-release drugs: multiple-unit pellet system (MUPS)," Journal of Controlled Release, vol. 147, no. 1, pp. 2-16, 2010.

[14] M. Nitz and O. P. Taranto, "Film coating of theophylline pellets in a pulsed fluid bed coater," Chemical Engineering and Processing: Process Intensification, vol. 47, no. 8, pp. 1412-1419, 2008.

[15] N. Haddish-Berhane, S. H. Jeong, K. Haghighi, and K. Park, "Modeling film-coat non-uniformity in polymer coated pellets: A stochastic approach," International Journal of Pharmaceutics, vol. 323, no. 1, pp. 64-71, 2006.

[16] H. Lin, Y. Dong, D. Markl, Z.J. Zhang, Y.C. Shen, J.A. Zeitler, "Pharmaceutical film coating catalogue for spectral-domain optical coherence tomography", Journal of Pharmaceutical Sciences, Vol 106, no. 10, pp. 3171-76, 2017.

[17] J. M. Mauritz, R. S. Morrisby, R. S. Hutton, C. H. Legge, and C. F. Kaminski, "Imaging pharmaceutical tablets with optical coherence tomography," Journal of Pharmaceutical Sciences, vol. 99, no. 1, pp. 385-391, 2010.

[18] H. Lin, Y. Dong, Y. Shen, and J. A. Zeitler, "Quantifying pharmaceutical film coating with optical coherence tomography and terahertz pulsed imaging: an evaluation," Journal of Pharmaceutical Sciences, vol. 104, no. 10, pp. 3377-3385, 2015.

Chapter 5 An Alternative Method to Evaluate Cleaning Effectiveness of Washing Product

5.1 Introduction

Optical Coherence Tomography (OCT) as a non-destructive and non-contact optical technology that is capable of acquiring depth-resolved information of the measured sample. OCT has been gaining interest in several potential non-destructive detection fields. Examples of demonstrated studies span from the pharmaceutical applications to art diagnostics [**1,2**], polymer detection [**3,4**], subsurface defect detection [**5,6**], automotive paints analysis [**7,8**], and the investigation of silicon integrated circuits [**9**]. The Full-Field OCT (FF-OCT) technique enables Three-Dimensional (3D) visualisation and interpretation of a sample with layered structures. Depending on the measured sample, FF-OCT can help to understand the variability scientifically when changing user-interested elements. In comparison to conventional flying-spot OCT systems where 3D imaging was obtained by raster scanning over the sample in both *x*- and *y*- lateral directions, time-domain FF-OCT is naturally suitable to obtain high lateral and axial resolution 3D datacube with a single *z*-direction scan, due to focus position being scanned simultaneously with probed depth and efficient use of low-cost broadband spatially incoherence light source, respectively.

The ability to measure and monitor the removal of semi-solid fats or oils from substrates is important for the assessment of the effectiveness of the current surfactant systems for stain removal. Colourimetry, the science of colour measurement, has been widely employed for wash studies to quantify colour and to derive colour differences from the soiled samples before and after washing [**10–12**]. The technique is based on the tristimulus theory of colour vision, which states that the human eye possesses receptors for three primary colours, and all colours can be regarded as mixtures of these primaries [**13**]. The colours of the tested fabric can be measured by using a spectrophotometer and recorded numerically in terms of colour formulae such as the CIE $L^*a^*b^*$ (known as CIELAB) colour space. This colourimetric method is easy to use, but it requires the stains or soils to be coloured for the level of removal to be measured. As a result, the ΔE^* (delta E) values (defined as the difference between two colours) corresponding to washed and unwashed samples, as well as washed and unsoiled samples, represent the criteria for the stain removal efficiency. Although the chosen dyes are soluble in the

stains or soil which are investigated, the colourimetry method is however still an indirect method of measuring stain removal as it effectively measures dye removal. The colourimetry method does not provide depth-resolved information of the sample either.

Another type of cleaning product in the detergent industry is the stain remover which is used to remove oily and sooty smears from hard surfaces such as floors, sinks, stovetops and kitchen countertops. In this field, stain removal is usually assessed with biological or chemical methods. The Adenosine Triphosphate (ATP) bioluminescence method has been used to assess the soilability of a hard surface sample. The method is based on the detection of ATP using the firefly luciferase enzyme and luciferin cofactor. Hydrolysis of ATP by luciferase produces a yellow-green light, which can be detected by using a luminometer and recorded as a relative light unit. A positive luminescence reaction, i.e. the detection of light generated by ATP, indicates the presence of contamination of the surface [**14**]. In addition to the chemistry method, several surface profilometry techniques, such as Atomic Force Microscopy (AFM) (contact/non-contact) and Scanning Electron Microscope (SEM) (non-contact), have also been used in measure the soilability or the cleanliness of a hard surface, where the detected topography image can provide the information of the soil dimension and the soil distribution [**14,15**].

In this study, 1) it is demonstrated for the first time that FF-OCT is able to resolve the removal of oily and fatty stains in cotton fabrics, which subjects to cleaning processes. To do this, the proposed Ultrahigh-Resolution (UHR) FF-OCT is used to acquire a series of OCT images of the measured fabric samples, which have undergone a controlled staining and cleaning processes, at the 1-μm and 1.6-μm axial and lateral resolutions, respectively, in order to provide sub-surface information to evaluate the cleaning effect. The technique results were verified by the current gold standard method of colourimetry, but it has also shown to work without the dyeing of some stains required by colourimetry; 2) By taking advantage of the achieved high lateral resolution, the proposed FF-OCT was also shown that it is applicable to be used as a non-contact and non-destructive surface profilometry tool to evaluate the soilability from the kitchen countertops treated with different-level greasy soils.

5.2 Material

5.2.1 Clean, Washed and Soiled Cotton Fabrics

In this study, all the cotton fabric samples were selected and provided by Unilever Port Sunlight Centre (Port Sunlight, UK). The white cotton fabric sample is typically woven fabric which is usually used as the substrate for evaluating the cleaning efficacy of detergent. The samples were classed into two groups according to the stains used in the substrate, and the soiled samples were dyed in order to visualise the oily stains. As listed in Table 5.1, the clean fabric substrate is labelled as CN-11 in group A and CN-17 in group B. The soiled sample in group A was stained by 50% beef fat and 50% lard with a red dye (CS-63S), while the soiled sample in group B was stained by used frying fat with a blue dye (CS-46B). The washed samples were washed with a detergent formulation at 20 and 40^{o}C for 30 minutes.

Table 5.1 Measured cotton fabric samples

	Photo	Clean/Soiled	Tag
Sample Group A		Clean	CN-11
	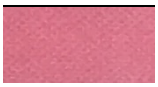	Washed at 40 ^{o}C	CS-63S@40
		Washed at 20 ^{o}C	CS-63S@20
		Soiled by 50% beef fat + 50% lard	CS-63S
Sample Group B		Clean	CN-17
		Washed at 40 ^{o}C	CS-46B@40
		Washed at 20 ^{o}C	CS-46B@20
		Soiled by used frying fat	CS-46B

5.2.2 Kitchen Countertops Treated with Different-level Soils

Table 5.2 lists the soiled kitchen countertop information, where the soil material was the kitchen stain, including bacon fat, lard, soot/carbon black. The soil with different levels was applied in the countertop substrate (labelled as substrate, fully soiled, ¾ soiled and ½ soiled).

Table 5.2 Measured hard surface samples

Substrate	Photo	Stain	Soiled Level	Experiment Label
Kitchen countertop		Kitchen grease	Substrate	Substrate
			Full	Fully Soiled
			3/4	¾ Soiled
			1/2	½ Soiled

5.3 Sub-surface Imaging of Soiled Cotton Fabric Samples

Colourimetric Measurement

Standard colourimetric measurement was performed and quantified into CIELAB colour space using a spectrophotometer (Color i7 X-rite) [**10**–**12**]. Stains removal can be then evaluated in terms of Euclidean distance, ΔE^*, taken as the difference of the measured L^*, a^*, and b^* values between clean and washed samples. L^* represents the lightness, while a^* represents the green to the red elements and b^* represents the blue to the yellow elements. Therefore, the lower is ΔE^*, the more effective is the washing. The Stain Removal Index (SRI) is calculated as 100 minus ΔE^*, where 100 represents white (clean sample). Thus, a higher SRI represents a cleaner fabric that is closer to white.

FF-OCT Measurement

Colourimetry provides a simple, fast measurement of discriminating between clean, soiled and washed cotton fabric samples. However, it requires the sample to be dyed prior to measurement, i.e. red and blue colours applied in the study. Further, the colourimetry technique cannot reveal the information on the effects of cleaning along with the sample depth. Here, we investigate the feasibility of using OCT cross-sectional (B-scan) images to discriminate between the cleaning effect of the washed and unwashed fabrics. Figure 5.1 shows the high-resolution microscopic images with the FF-OCT focused on the sample surface, where woven fabric structure and micron-sized fibres can be seen. The woven fabric samples in the two groups are made up of interlaced yarns, and the diameter of the yarn is approximately 150 µm. Since tested samples have been soiled or washed, a Region-of-Interest (ROI) (shade/green region shown in Fig. 5.1) was selected along the weft yarn direction of the sample, which consists of 160 × 1000 pixels corresponding to an imaging area of 100 × 1000 μm^2. This allows a fine scanning up to 200 µm in the air with a 5-nm scan step under a fast frame rate of 200 frames per second (fps). The resultant 3D datacube was reconstructed using the proposed method.

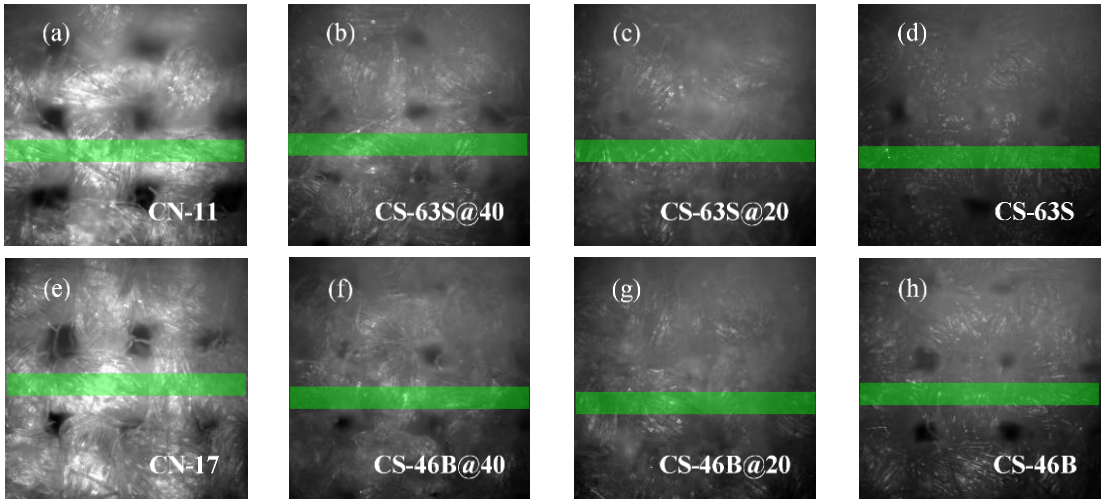

Figure 5.1 Microscopic images corresponding to the fabric samples in each group taken from the sample arm of the Full-Field Optical Coherence Tomography (FF-OCT). The Region-of-Interest (ROI) where the depth-resolved scanning was performed is highlighted with shade/green.

Results and Discussion

Figures 5.2(a–e) and 5(g–k) show the representative B-scan images of the measured fabric samples in each group whilst Figs. 5.2(f) and 5.2(l) show their corresponding A-scan waveforms. The clean samples (CN-11/CN-17) exhibit structural layering with the strongest signal when compared to others. In contrast, for the soiled samples (CS-63S/CS-46B), nearly all the detected signals came from the sample surface, and the intensities of subsequent reflections are significantly reduced. After washing the soiled sample (CS-63S/CS-46B) under 20^{o}C (CS-63S/CS-46B@20), a small amount of soil is removed, and micron-sized fibres can be resolved at the sub-surface level with increased intensity. It is well-known that when cleaning is performed at an elevated temperature, increased soil removal can be achieved. This, therefore, explains why the measurements from the 40^{o}C-washed sample (CS-63S/CS-46B@40) demonstrate an increased signal intensity when compared against the same samples but washed at 20^{o}C. In summary, both the B-scan images and the A-scan waveforms suggest that the number of sub-surface structures is a good indicator of the cleaning effect: the higher the number, the cleaner the sample (or the less the remaining soils in a sample).

As shown in Fig. 5.2, both the clean and the soiled samples show a limited penetration depth of less than 70 µm, accounting for approximately 50% of the entire fabric thickness. This is mainly determined by the strong scattering of the fabric sample where

there is a significant number of pores or air gaps between the interlocked fibres and fibrils that act as strong scatters. On the other hand, these air gaps also provide optical pathways for some light to reach the 'scatter' below the surface. The strong scattering from the air/fabric structures leads to relatively large detectable OCT signals even from deeper fabric interfaces. For the soiled samples, firstly, scattering losses are reduced because of the reduced Refractive Index (RI) mismatch between the stain and fabric (as compared with air/fabric). This in principle should lead to larger penetration depth. However, this reduced scattering will also lead to reduced OCT signal, making it more difficult to be detected by the FF-OCT particularly for the scattered light from deeper structures. Secondly, the stains may absorb the light or block the optical pathway, thus making the light more difficult to reach the deeper fabric interface and/or the scattered light more difficult to reach the OCT device. Consequently, no significant sub-surface features can be observed in the acquired B-scan images. In addition, due to the relatively high-NA microscope objective and specific design details of the experimental setup (no dynamic focus correction), there is an additional mechanism that will limit the penetration depth. As a material with a RI value $n \neq 1$ is imaged into the interferometric probe depth moves up compared to the expected location ($n = 1$) whereas the focus position moves down. The result is the image of the depth location being interferometrically probed becomes blurred, when this blurring becomes comparable to or larger than the spatial coherence of the illuminating light, the interferometric signal will be attenuated. Future method developments of statically optimising focus position or dynamic focus correction would be expected to increase the penetration depths, particularly for heavily soiled or wet samples.

In order to further understand the underlying mechanisms of the observed correlation between the measured OCT signal and the fabric cleanliness, additional measurements were performed on wetted fabric samples. By wetting the clean fabric sample sufficiently, the pores and air gaps within the fabric samples will be filled with water, leading to decreased RI mismatch thus reduced scattering (air/fabric versus water/fabric). As shown in Figs. 5.2(e) and 5.2(k), the obtained B-scan images are indeed similar to strongly soiled fabric samples, suggesting that the scattering plays an important role in the observed correlation between the measured OCT signals and the cleanliness of the sample. Of course, some stains may absorb the light or block the optical pathway and its impact on the measured OCT signal should also be considered.

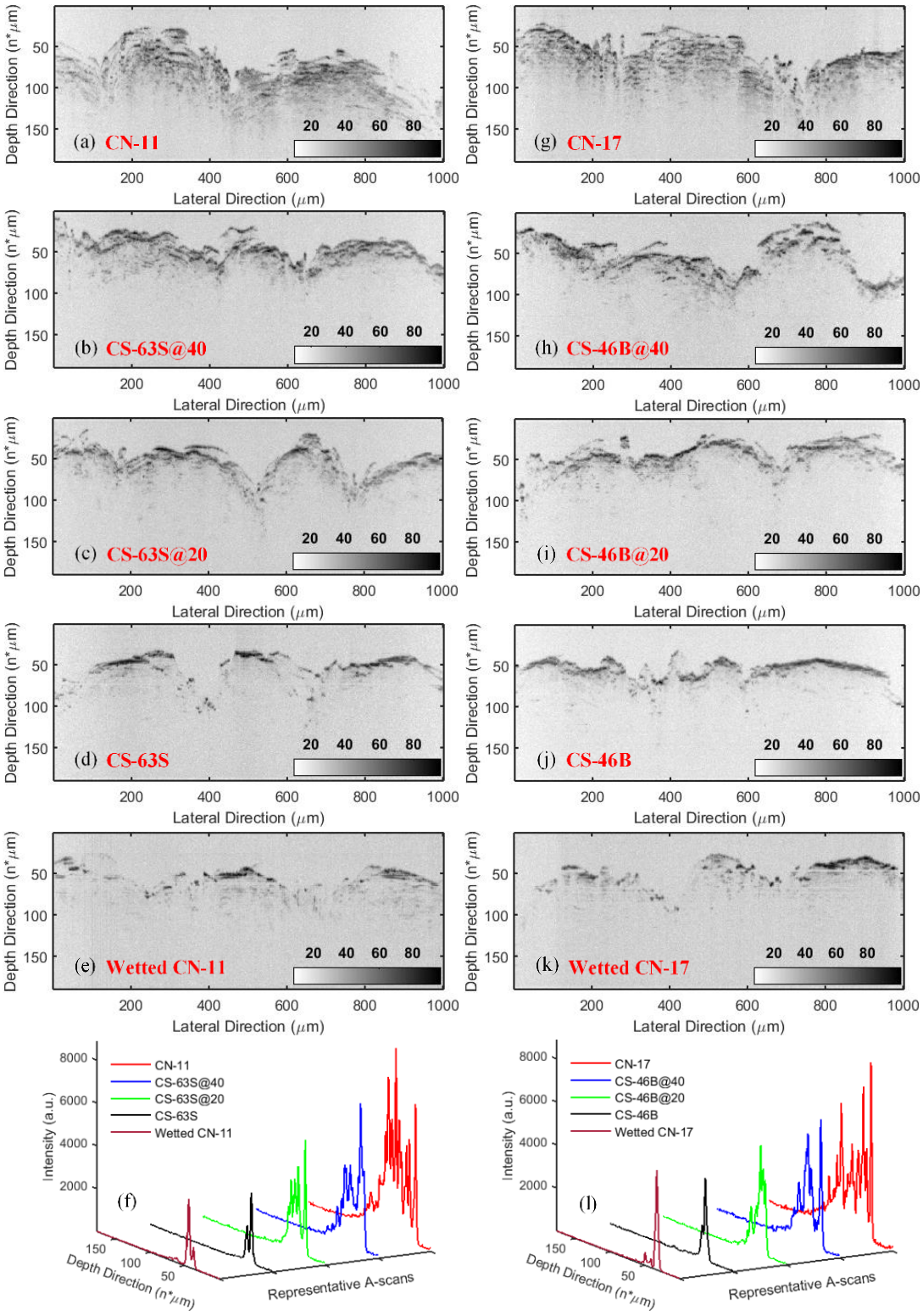

Figure 5.2 Sub-surface imaging of the cotton fabric samples in the two groups showing OCT measurements with cross-sectional (B-scan) images and tomography signals (A-scan).

In order to investigate the feasibility of using OCT measurement to assess the cleaning effect, we propose here a method based on the analysis of the volume taken up by the detectable sub-surface fibres. In particular, the volume can be obtained with the following steps

1) Threshold setting for isolating imaged fibres from the background;
2) Labelling surface area through A-scan signal based analysis;
3) Calculating the volume of the fibres detected below the surface area.

Firstly, the segmentation threshold was determined from the reconstructed 3D datacubes of clean, soiled and washed samples, respectively, where Otsu's method was used [**16**]. As a result, the area which only includes imaged fibres was isolated. Secondly, the fabric surface region was marked in each 3D image by finding the first peak positions of the A-scan signals involved in the analysed 3D datacube. Consequently, the volume occupied by the detectable fibres beneath the marked surface was calculated with known lateral and axial pixel size.

Figure 5.3 shows the fibre covered area and the marked surface area with red of the imaged fabric samples in the groups A and B. It can be seen that there are a high number of micron-size fibres detected beneath the surface of the clean sample. In contrast, signals that reflected from the sub-surface fibres of the soiled sample are noticeably weaker. With an increase in washing condition, sub-surface fibres became increasingly noticeable. This is compared against the SRI which is estimated based on measured L^*, a^* and b^* values (see Table 5.3). Moreover, Figure 5.4 shows a good correlation between the volume and the SRI, where the y- axis represents measured volume results occupied by the detectable sub-surface fibres from the soiled and the washed samples in the two groups while the x- axis represents the calculated SRI values of them based on the colourimetric measurement. Note that each FF-OCT quantification result is derived based on the fine 3D scan (5-nm scan step) covering a volume of 100 × 1000 × 200 μm^3 and each SRI result is derived based on 5 colourimetric measurements. thus demonstrating that the FF-OCT system could be a suitable alternative for inspecting the cleanliness of the fabric sample.

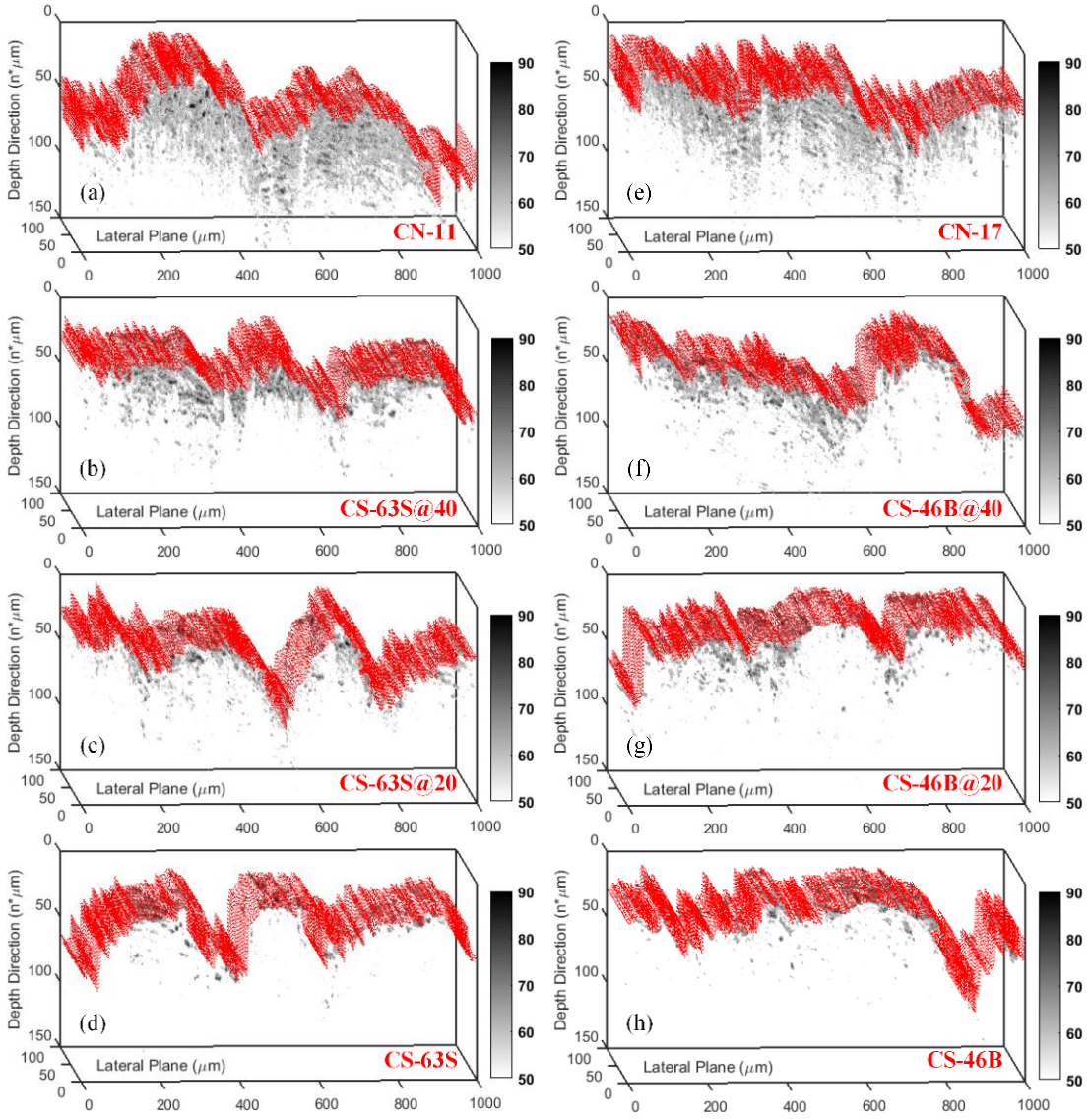

Figure 5.3 Marked surface area (red) and detectable sub-surface fibres of the imaged fabric samples in the two groups. (a–d) and (e–h) are the results corresponding to the samples in group A and group B, respectively.

Table 5.3 Colourimetric measurement result and Stain Removal Index (SRI) of the cotton fabric samples after washing with a detergent formulation at 20 and 40 ℃

	Fabric Sample	*L**		*a**		*b**		Δ*E**	SRI
		$\bar{x}^a$	SD[b]	$\bar{x}$	SD	$\bar{x}$	SD		
Group A	CN-11	95.47	0.04	-0.30	0.01	2.68	0.04	/	100
	CS-63S@40	72.45	0.43	38.43	0.73	7.55	0.25	45.32	54.68
	CS-63S@20	66.64	0.89	47.38	1.44	12.50	0.79	56.58	43.42
Group B	CN-17	95.39	0.01	-0.34	0.01	2.92	0.04	/	100
	CS-46B@40	70.34	0.24	6.81	0.10	-20.28	0.38	34.88	65.12
	CS-46B@20	68.35	0.39	8.21	0.30	-24.72	0.56	39.60	60.40

[a] Mean value of 5 measurements

[b] Standard Deviation

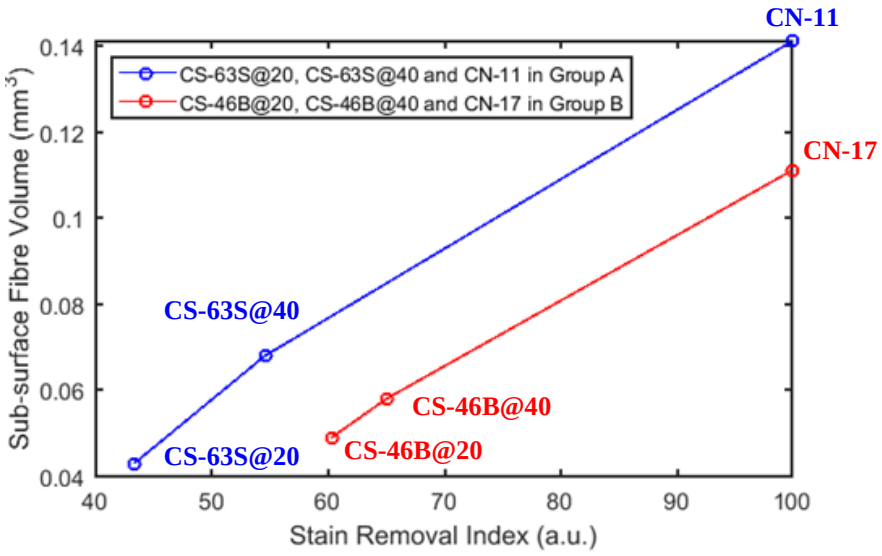

Figure 5.4 Cleaning effects demonstrated by detectable sub-surface fibre volume related to the FF-OCT measurements and Stain Removal Index (SRI) related to the colourimetric measurements.

To further show that the OCT-based method does not require dyeing the sample, Figure 5.5 shows the B-scan images of the fabric samples treated with the same soils but without any pigment applied, where there are no obvious differences compared to the B-scan images of the soiled dyed samples. This suggests that the proposed FF-OCT method can be used to measure the stain removal of fabric sample without the need of dying process.

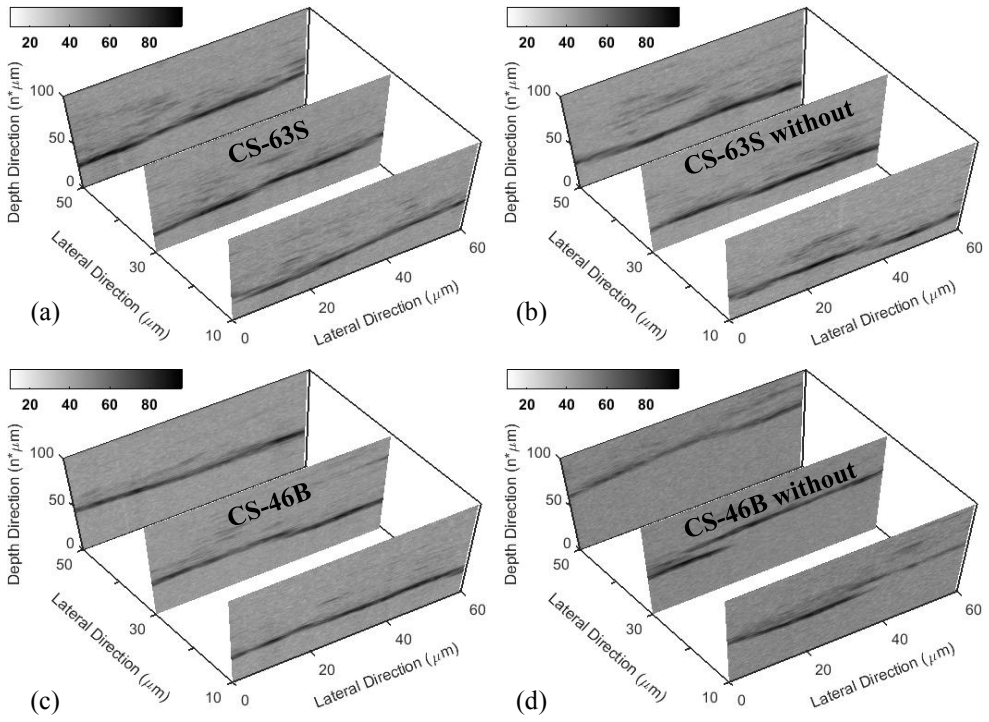

Figure 5.5 Comparison measurement between the soiled samples with and without dyeing. (a) and (b) are the B-scan images of the soiled sample CS-63S and its corresponding non-dye sample. (c) and (d) are the B-scan images of the soiled sample CS-46B and its corresponding non-dye sample. Each measurement is performed to obtain Three-Dimensional (3D) data with a size of $60 \times 60 \times 100$ μm^3, and the B-scan images are extracted from the reconstructed 3D datacubes.

In current wash studies, white fabric is usually used as the substrate for assessing the effectiveness of detergent. The fabric is stained with soil and the effectiveness of the detergent is measured by how closely the after-wash colour gets back to the white colour of the fabric. For naturally coloured stains such as tomato and curry sauce, the removal of them from the white fabric is highly visible. However, for other stains such as sunflower oil and butter stains, these may not be clearly visible on the white fabric although present on the fabric. In order to visualise the required stains, pigments or dyes are used for example violet dyes is used to visualise beef fat or vegetable oil on white fabric. Even though the chosen dyes are soluble in the stains or the soils that are investigated, it is generally difficult to confirm if the dyes do not become separated from, and behave independently to, the stains during the cleaning process. The assessment of the effectiveness of detergent by means of colour difference is, therefore,

an indirect method of assessment since what is being directly measured is effectively the removal of the dyes, not necessarily the actual staining agent.

The proposed FF-OCT method, even though is not ideal in taking over stain removal measurement in its current form because of the number of ingredients and stains used in a typical stain removal study. It can nevertheless be used as a complementary method of measuring stain removal. It is envisaged that once several ingredients and formulations against several stains are screened, the proposed FF-OCT method can be used to confirm the findings on a smaller selection of stains and formulation as it is a direct method of measuring stain removal rather than an indirect (colourimetry) method. This potentially opens up a method of measuring real-life stains without the need for pigmentation or dyes currently applied.

5.4 Topographic Imaging of Soiled Hard Surface Samples

Surface Measurement

A 3D surface measurement was performed with the proposed UHR FF-OCT system. Contributed by the achieved high lateral resolution of about 1.6 µm, micron-sized soil particles (i.e. 2–10 µm) that adhered on the sample surface can be resolved. Note that, the use of the high-NA objective leads to a small illumination spot of about 1 mm in diameter. The acquired volumetric data from each measured sample consists of 80 × 400 × 200 pixels, which corresponds to a practical volume of 200 × 1000 × 100 μm^3. The surface topography image can be then generated through the analysis of A-scan signals, in which the peak position, the zero Optical Path Difference (OPD) position, searched from each A-scan signal represents the surface location at that point. The air/soil interface and the air/substrate interface have strong reflection because of the changed RI from the air to a denser medium. In this study, all the samples were illuminated with the same incident power of approximately 1 mW.

Result and Discussion

In order to investigate the feasibility of using the FF-OCT to image the soiled countertop samples, 5 ROI regions selected from a specially treated sample (including the substrate, soiled and cleaned areas) were measured, as shown in Figure 5.6.

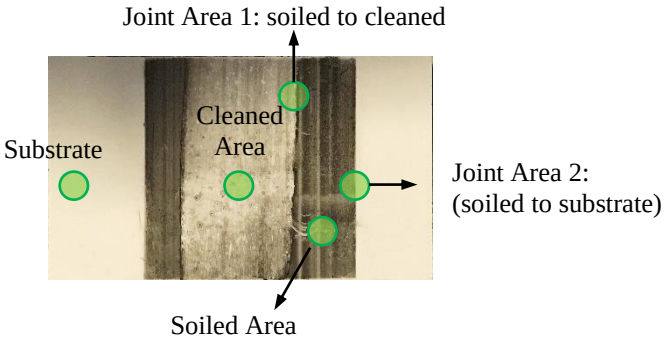

Figure 5.6 Photograph of a specially treated countertop as the measurement sample. 5 ROIs are denoted with the green circles in each typical region.

Figure 5.7 shows the high-resolution microscopic images that were taken from the five ROI regions with the FF-OCT, where each image covers a region including 1000 × 1000 pixels (approximately 0.6 × 0.6 mm^2). The image taken from the soiled region (Fig. 5.7(a)) shows the lowest reflection/backscattering signal intensity when

comparing with the cleaned (Fig. 5.7(b)) and substrate (Fig. 5.7(c)) ones. The image taken from the cleaned region (Fig. 5.7(b)) shows an increased signal intensity, but it is still weaker than the substrate region (Fig. 5.7(c)). There is a clear boundary between the soiled/cleaned area (Fig. 5.7(d)) as well as the soiled/substrate area (Fig. 5.7(e)). The histogram illustrated in Fig. 5.7(f) was generated from the soiled, cleaned and substrate ROIs, which can be used for discrimination. Specifically, mean intensity (16-bits grey scale) of the three regions are respectively calculated as 14614, 35775 and 45710, corresponding to the soiled, cleaned and substrate regions. However, such microscopic image cannot provide any information on the soil dimension and the distribution on the hard surface.

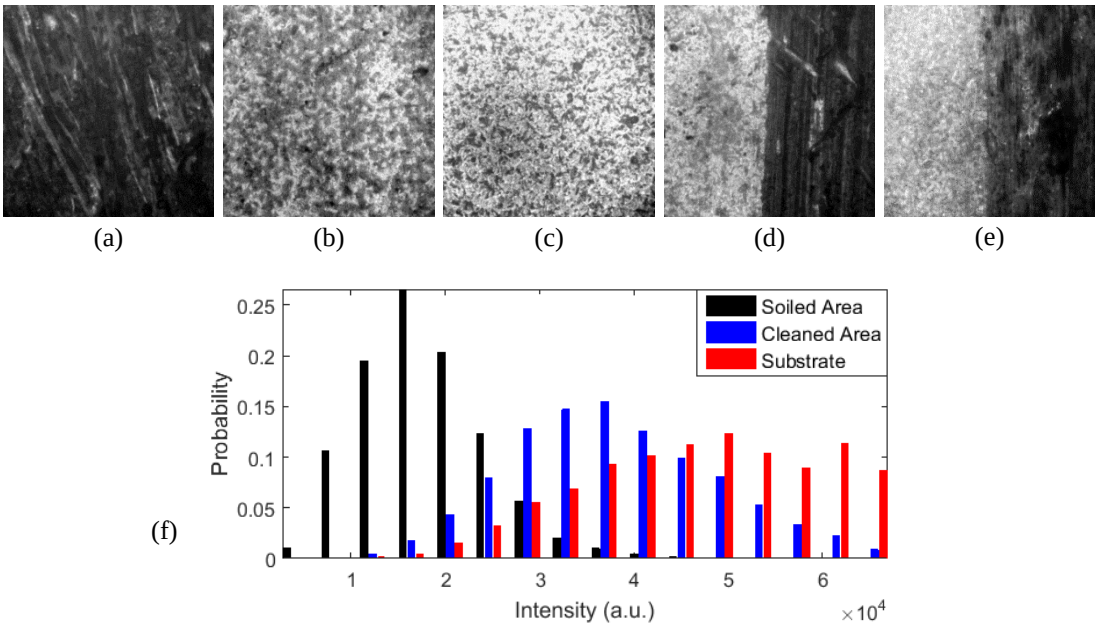

Figure 5.7 Microscopic images of the specially treated countertop sample. (a–e) snapshots are taken from soiled, cleaned, substrate, cleaned/soiled joint area and substrate/soiled joint area, respectively. (f) histogram comparison between soiled, cleaned and substrate area.

Also, we performed rapid OCT measurements for each ROI region. The imaging area was selected as a single long line, which covered 1600 pixels (approximately 1 mm), and the scanning distance was set to 100 µm. As shown in Fig. 5.8(a), the B-scan image taken from the soiled ROI demonstrated that the soil material might absorb a part of the incident light and lead to a weak reflection signal from the surface. In contrast to the soiled one, the B-scan image taken from the cleaned ROI showed a higher signal intensity from the surface, indicating that a number of soils were removed (as shown in

Fig. 5.8(b)). There may be the residual soils that result in the relatively weaker signal intensity when comparing with the B-scan image taken from the substrate ROI (as shown in Fig. 5.8(c)). The differences can also be observed from their corresponding A-scan waveforms (Fig. 5.8(d)). In addition, the B-scan images that were taken from the two joint ROIs (Fig. 5.9) show the differences between the soiled and cleaned as well as the soiled and substrate regions.

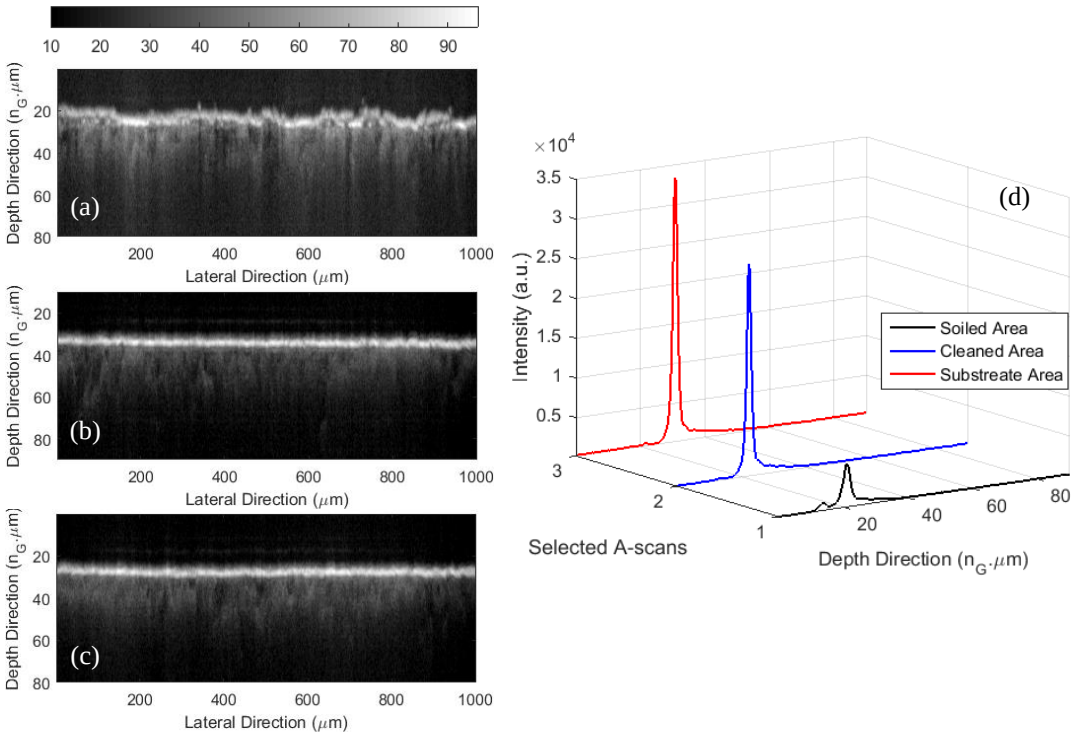

Figure 5.8 B-scan images and A-scan signals measured from the specially treated countertop sample. (a–c) B-scan images taken from the soiled, cleaned, substrate areas, respectively. (d) Representative A-scan signals extracted from their corresponding B-scan images, black line for the soiled ROI, blue line for cleaned ROI and red line for the substrate ROI.

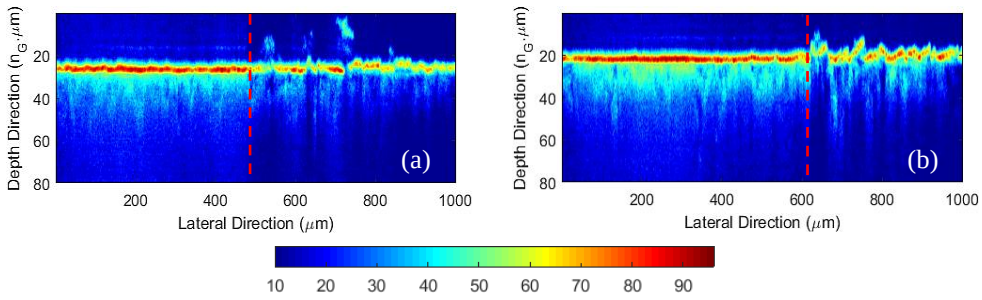

Figure 5.9 B-scan images measured from the joint ROI regions in the specially treated countertop sample. (a) B-scan image taken from the cleaned/soiled joint area. (b) B-scan taken from the substrate/soiled joint area.

Although the analysis based on the B-scan images can be used to differentiate differences between the cleaned and soiled samples, it cannot still characterise the studied soil. In this section, the FF-OCT was implemented to carry out surface profilometry measurement to investigate the sample surface soilability. As shown in Fig. 5.10, the 3D topography images visualise the soil dimension and distribution, where the colour represents the reflection intensity from the surface. The result of the substrate sample, as shown in Fig. 5.10(a), demonstrates a uniform surface with high reflection, and very few points have the obvious height information which may be the adhered dust. The result of the fully soiled sample, as shown in Fig. 5.10(b), shows that a great number of soil particles with the surface heights from 2 μm to 15 μm distribute randomly on the surface, and it corresponds to a weak surface reflection. We can also notice that the distributed soil on the 3/4 soiled sample (see Fig. 5.10(c)) are less than the fully soiled one, and the differences can also be observed from the increased surface reflection. In contrast to the 3/4 soiled sample, there are fewer soils distributed on the 1/2 soiled one (see Fig. 5.10(d)).

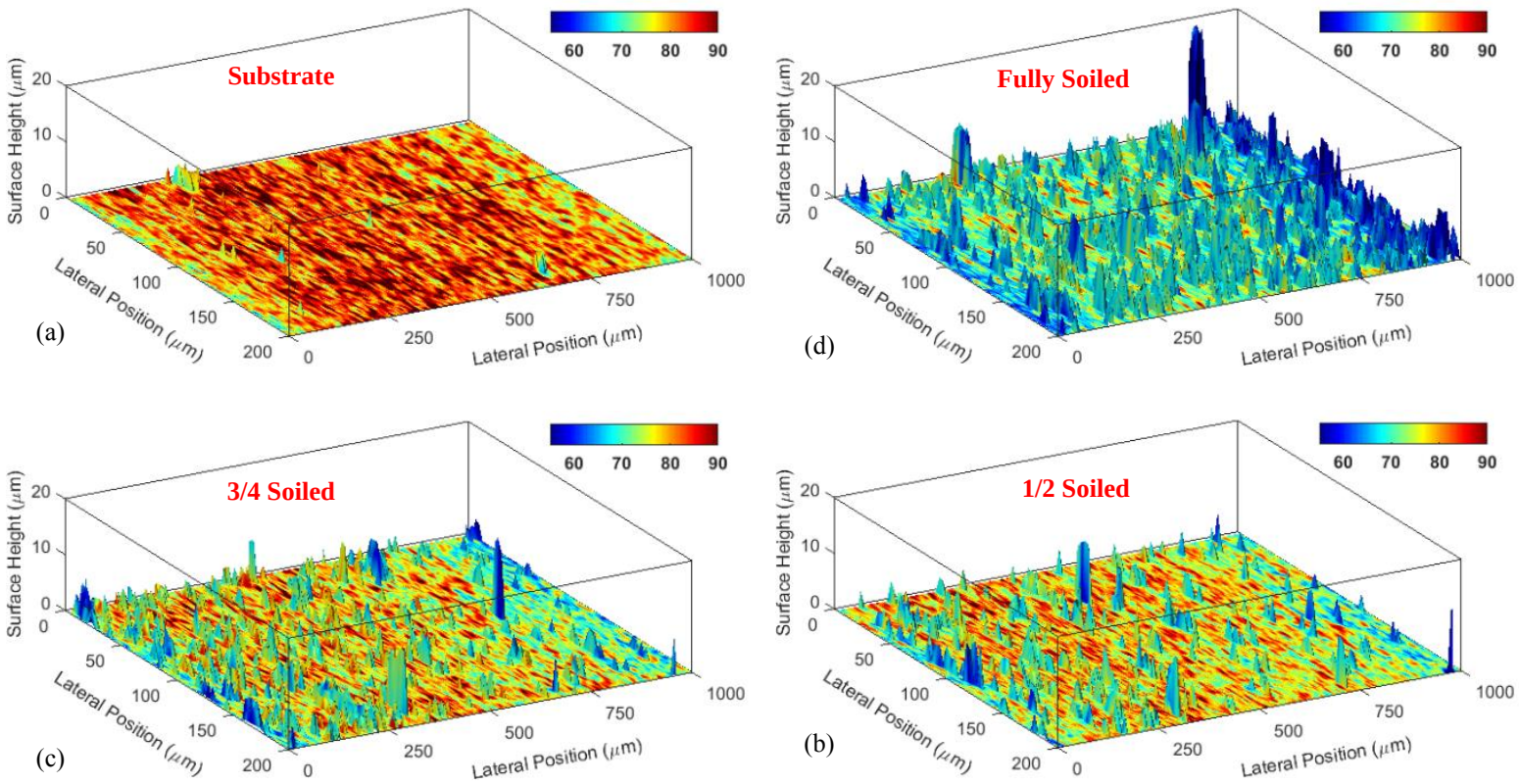

Figure 5.10 OCT topography images measured from the countertop samples treated with different-level soils. (a) Topography image of the substrate sample (b) Topography image of the fully soiled sample. (c) Topography image of the 3/4 soiled sample. (d) Topography image of the 1/2 soiled sample. The colour bar with the dB unit represents the surface reflection, in which blue is weakest and red is strongest.

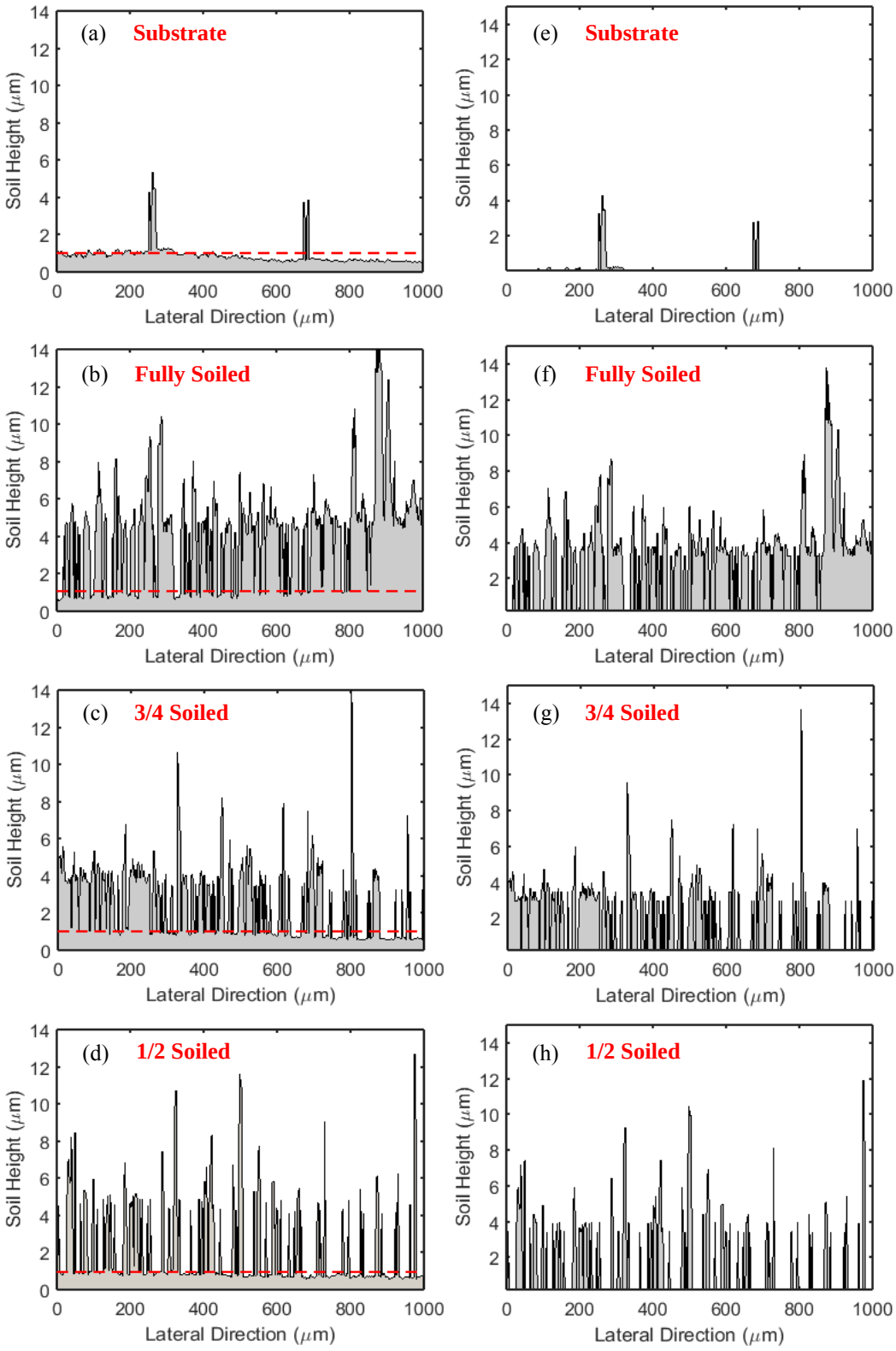

Figure 5.11 Soil height and distribution map. (a–d) Averaged surface and soil height, where the red dotted lines are the marked substrate regions. (e–h) The isolated soil-covered area after removing the substrate part.

As a further illustration, the soilability of the measured samples was quantified by analysing the soil coverage area. Figures 5.11(a–d) show the averaged soil height for each sample along the *x* direction (length of 1000 µm) of the *x*-*y* plane, where the red dotted lines represent the countertop substrate as the baseline for isolating the region with soils. Note that, the baseline was manually selected at a constant height position, which could introduce a small error caused by the neglect of the roughness of the substrate. The soil coverage area can be then calculated with the known axial (0.5 µm) and lateral (2.5 µm) pixel sizes after dropping the substrate area (below the marked line), as shown in Figs. 5.11(e–h). They are 81.25 μm^2 for the substrate sample, 1085 μm^2 for the fully soiled sample, 731.25 μm^2 for the 3/4 soiled sample and 508.75 μm^2 for the 1/2 soiled sample. Additionally, Figure 5.12 illustrates the quantified soilability index (the orange bars) by normalising the soil coverage area with an assumed 100% soiled area which is corresponding to 1250 μm^2. It can be found that the result agrees with the known tendency of the different soil levels (the blue bars).

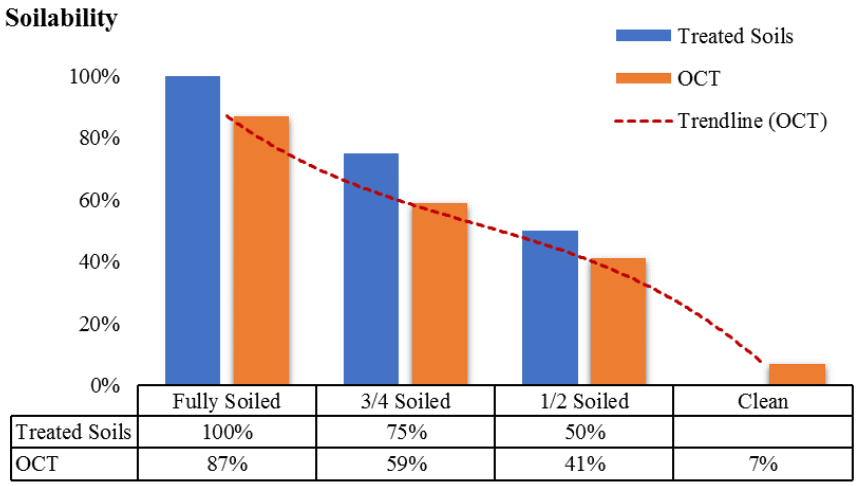

	Fully Soiled	3/4 Soiled	1/2 Soiled	Clean
Treated Soils	100%	75%	50%	
OCT	87%	59%	41%	7%

Figure 5.12 Soilablity assessment result compared with the known soil level. The quantified value has been normalised with an assumed 100% soiled area as 1250 μm^2 (0.5 µm × 2.5 µm × 1000).

5.5 Conclusion

To summarise, in this chapter, 1) the proposed UHR FF-OCT has been used to differentiate clean, soiled and washed cotton fabrics. By the achieved axial and lateral resolutions of 1 µm and 1.6 µm, respectively, the micron-sized fibres/fibrils consisting of the cotton fabric can be resolved. The fibres which can be detected from the sub-surface area enables the assessment of the cleaning effects. A stain removal quantification method has been developed based on the analysis of the reconstructed 3D datacube. The volume of the detectable sub-surface fibre in turn can be used to evaluate the stain removal. The FF-OCT system can provide insightful information for evaluating the fabric substrate used in the testing of detergent products without the need for dyeing the soil material; 2) the proposed UHR FF-OCT has been used to evaluate the soilability from the soiled hard surface sample by profilometry measurement. The obtained topography images visualise the differences that exist in the soil height and distribution between the measured kitchen countertop samples treated with different levels of greasy soils. The soilability can be quantified by calculating the soil coverage area. The proposed FF-OCT has demonstrated several advantages including non-contact, non-destructive, single-axis scanning and a lower cost than AFM and SEM. Thus, it could be an alternative way to assess the efficacy of hard surface cleaning products.

References

[1] H. Liang, M. G. Cid, R. G. Cucu, G. M. Dobre, A. G. Podoleanu, J. Pedro, and D. Saunders, "En-face optical coherence tomography-a novel application of non-invasive imaging to art conservation," Optics Express, vol. 13, no. 16, pp. 6133-6144, 2005.

[2] H. Liang, R. Lange, H. Howard, and J. Spooner, "Non-invasive investigations of a wall painting using optical coherence tomography and hyperspectral imaging," in O3A: Optics for Arts, Architecture, and Archaeology III, 2011, vol. 8084, p. 80840F: International Society for Optics and Photonics.

[3] J. P. Dunkers, R. S. Parnas, C. G. Zimba, R. C. Peterson, K. M. Flynn, J. G. Fujimoto, and B. E. Bouma, "Optical coherence tomography of glass reinforced polymer composites," Composites Part A: Applied Science and Manufacturing, vol. 30, no. 2, pp. 139-145, 1999.

[4] J. P. Dunkers, F. R. Phelan, D. P. Sanders, M. J. Everett, W. H. Green, D. L. Hunston, and R. S. Parnas, "The application of optical coherence tomography to problems in polymer matrix composites," Optics and Lasers in Engineering, vol. 35, no. 3, pp. 135-147, 2001.

[5] M. D. Duncan, M. Bashkansky, and J. Reintjes, "Subsurface defect detection in materials using optical coherence tomography," Optics Express, vol. 2, no. 13, pp. 540-545, 1998.

[6] M. Bashkansky, M. D. Duncan, M. Kahn, D. Lewis, and J. Reintjes, "Subsurface defect detection in ceramics by high-speed high-resolution optical coherent tomography," Optics Letters, vol. 22, no. 1, pp. 61-63, 1997.

[7] J. Zhang, B. M. Williams, S. Lawman, D. Atkinson, Z. Zhang, Y. Shen, and Y. Zheng, "Non-destructive analysis of flake properties in automotive paints with full-field optical coherence tomography and 3D segmentation," Optics Express, vol. 25, no. 16, pp. 18614-18628, 2017.

[8] Y. Dong, S. Lawman, Y. Zheng, D. Williams, J. Zhang, and Y. Shen, "Nondestructive analysis of automotive paints with spectral domain optical coherence tomography," Applied Optics, vol. 55, no. 13, pp. 3695-3700, 2016.

[9] K. A. Serrels, M. K. Renner, and D. T. Reid, "Optical coherence tomography for non-destructive investigation of silicon integrated-circuits," Microelectronic Engineering, vol. 87, no. 9, pp. 1785-1791, 2010.

[10] G. van Dalen, A. Don, J. Veldt, E. Krijnen, and M. Gribnau, "Colour analysis of inhomogeneous stains on textile using flatbed scanning and image analysis," in Conference on Colour in Graphics, Imaging, and Vision, 2008, vol. 2008, no. 1, pp. 53-57: Society for Imaging Science and Technology.

[11] E. Ilec, B. Simončič, and A. Hladnik, "Evaluation of surfactant detergency using statistical analysis," Textile Research Journal, vol. 79, no. 4, pp. 318-325, 2009.

[12] S. Shivaji Biranje, A. Nathany, N. Mehra, and R. Adivarekar, "Optimisation of detergent ingredients for stain removal using statistical modelling," Journal of Surfactants and Detergents, vol. 18, no. 6, pp. 949-956, 2015.

[13] A. K. R. Choudhury, "Colour-difference assessment," in Principles of Colour and Appearance Measurement, M. L. Gulrajani, eds. (Elsevier, 2014)

[14] R. Kuisma, E. Pesonen-Leinonen, I. Redsven, H. R. Kymäläinen, I. Saarikoski, A. M. Sjöberg, and M. Hautala, "Utilization of profilometry, SEM, AFM and contact angle measurements in describing surfaces of plastic floor coverings and explaining their cleanability," Surface Science, vol. 584, no. 1, pp. 119-125, 2005.

[15] K. A. Whitehead, D. Rogers, J. Colligon, C. Wright, and J. Verran, "Use of the atomic force microscope to determine the effect of substratum surface topography on the ease of bacterial removal," Colloids and Surfaces B: Biointerfaces, vol. 51, no. 1, pp. 44-53, 2006.

[16] N. Otsu, "A threshold selection method from gray-level histograms," IEEE Trans. Syst. Man Cybern. vol. 9, no. 1, pp. 62–66, 1979.

Chapter 6 Compressive Imaging Technique for New-gen OCT

6.1 Introduction

Optical coherence tomography (OCT) has been used widely in medical diagnosis and has illustrated the potential in several novel applications such as the studies carried out in the above chapters of the thesis. Given a Spectral-Domain OCT (SD-OCT), due to the Fourier domain detection configuration, it has superior sensitivity and imaging speed compared to conventional Time-Domain OCT (TD-OCT). Nevertheless, when large imaging depth, as well as better axial resolution, is required, the camera used in SD-OCT has to capture spectra at a large sampling rate. This is because conventional image reconstruction algorithm for SD-OCT requires spectral-domain sampling beyond Nyquist rate to achieve a certain imaging depth. Such CCD or CMOS cameras and associated electronics are usually expensive and limit the imaging speed. Given a Full-Field OCT (FF-OCT) system, it has shown its capability to obtain high-resolution Three-Dimensional (3D) image with only a single axial scan. However, high-quality 3D FF-OCT imaging requires a finer axial scan, which may lead to a slow measurement time due to the limited frame rate of the used camera as well as storage burden due to the large 3D dataset. It can be overcome by using expensive CCD or CMOS camera and upgrading the storage space, but such a solution come at a cost. A possible technology trend to the next-gen OCT is the combination of compressive sensing technique (CS) and OCT imaging technique since the achievable sampling performance with CS technique is governed by the signal sparsity rather than the Nyquist-rate relied on the sampling device.

CS technique provides a novel signal sampling and reconstruction strategy, where sparse signals can be recovered from a small number of measurements [**1**]. Such an approach offers a promising solution for imaging in the infrared (IR) or terahertz (THz) frequencies as only a single detector, rather than a sensor array is required [**2**]. More significantly, compressive imaging can dramatically decrease the measurement time as compared with the conventional raster scanning modality, since fewer signal samples are required to reconstruct an image [**3**].

Let x represent the vector version of an image with N pixels. Suppose that x has a K-sparse representation $\hat{x}$ under a sparsity basis Ψ (i.e. the discrete cosine transforms or wavelet). The CS sampling process can be described as [**1**]

$$y = \Phi x = \Phi \Psi x \tag{6.1}$$

where y is the $M \times 1$ measured signal vector, Φ is a $M \times N$ ($M \ll N$) measurement matrix. The original signal x then can be obtained by solving an optimisation problem of ℓ_0 norm as

$$\min_x \left\| x \right\|_0 \ s.t.\ Ax = y \tag{6.2}$$

satisfying

$$y = \Phi \Psi x \tag{6.3}$$

where $A = \Phi\Psi$. In addition, if A satisfies the Restricted Isometry Property (RIP) [**1**], the x can be reconstructed reliably. The RIP holds if the measurement matrix Φ is incoherent with the sparsity basis Ψ [**4,5**]. Typical choices of measurement matrices include the Gaussian random matrix, the Bernoulli matrix, Toeplitz matrix and partial Hadamard matrix [**6–8**] etc. In a practical compressive imaging system, the measurement matrix is implemented using a Spatial Light Modulator (SLM) to vary the amplitude of light waves based on either the mechanical or the electro-optical method.

It can be found that a number of studies have been carried out for developing the compressive SD-OCT [**9–11**], where a tomography signal (A-scan) (x in Eq. 6.1) can be reconstructed from the compressively acquired interferograms (y in Eq. 6.1) by using a measurement matrix (Φ in Eq. 6.1) which contains the spectral information of the used light source. However, there is still a challenge to realise compressive imaging with an FF-OCT modality (i.e. more suitable for 3D imaging), where the compressive sampling from *en-face* plane may be required.

In this study, a block Toeplitz matrix is proposed as the measurement matrix for compressive imaging. When comparing with other measurement matrices, it takes advantage of memory efficiency while it shows a close reconstruction performance to those entirely random matrices. The compressive imaging ability is demonstrated firstly in the visible band by implementing the measurement matrix as a mechanical SLM. A 10-second video containing approximately 100 Two-Dimensional (2D) images (total

size: 96 pixels × 96 pixels × 100 frames) are acquired using a single-pixel photodiode and saved as 120000 One-Dimensional (1D) compressive signals (compression rate: 13%). In addition to the study in the visible band, the applicability of using the SLM to profile the THz imaging beam is investigated. In this study, THz Quantum Cascade Lasers (THz-QCLs), for the first time, is used as the radiation source in a compressive imaging system. The SLM is mounted on a linear, motorised translation stage, which allows the SLM to be moved along a 150-mm THz beam propagation path to record therefore a 3D THz beam profile. These pilot study results are envisaged to contribute to the development of a compressive FF-OCT system since the compressive sampling at the 2D image plane has been achieved by the proposed SLM.

6.2 Method

6.2.1 Novel SLM Spinning Disk Design

Figure 6.1 shows the schematic diagram of the proposed SLM which was fabricated as a spinning disk. The SLM disk is made of a 0.28-mm-thick stainless plate with a diameter of 200 mm. A number of round holes, which is designed from block Toeplitz matrix with 2-mm diameter each, are chemically etched on the disk. Each of the sampling holes is 100% transparent to the light while the stainless steel is 100% opaque to the light. The area enclosed by the red square in Fig. 6.1 is the zoom-in window that represents one of the effective sampling areas with a size of 32 mm × 32 mm.

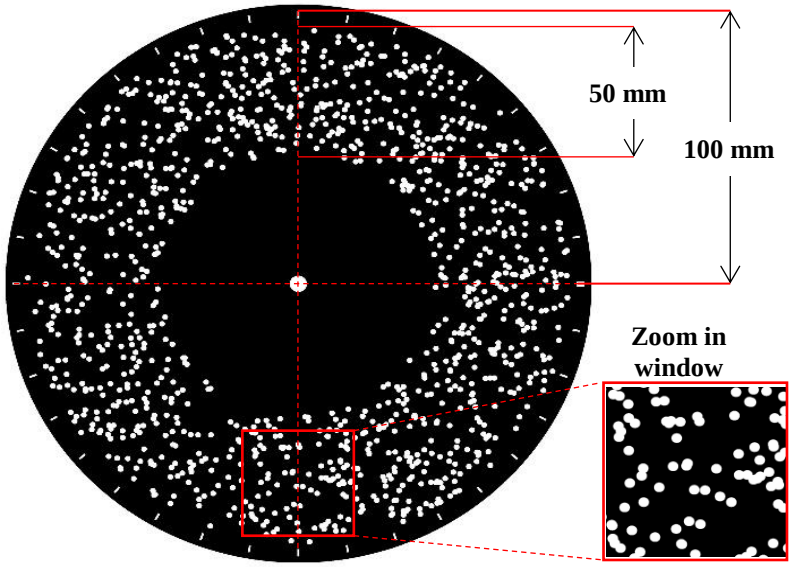

Figure 6.1 Schematic diagram of the Spatial Light Modulator (SLM) spinning disk.

In the previous studies [**12,13**], Printed Circuit Boards (PCBs) have been used as an SLMs. The PCB substrate material is mostly opaque to infrared radiation and it also absorbs strongly THz radiations particularly at higher THz frequencies. In addition, the absorption and the dispersion caused by the PCB substrate may not be uniform across the whole substrate, and this will affect the encoding accuracy, thus degrading the reconstructed image quality. In particular, the THz radiation spans a frequency range from 300 GHz to 10 THz (wavelength is from 1 mm down to 30 μm) [**14**]. Thus, when the sampling pattern size of an SLM is close to the wavelength of the emitted THz radiation, the scattering and the diffraction effects are no longer negligible. Preliminary

simulation and measurement result shows that the proposed SLM disk effectively reduces the diffraction and the scattering effects in comparison with those reported SLMs whereby the square sampling pattern with the sharp corner was used.

6.2.2 Performance as Measurement Matrix

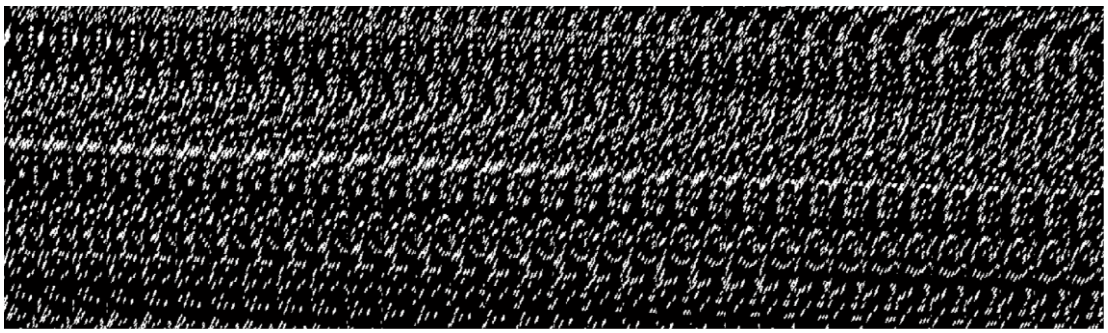

Figure 6.2 Compressive Sensing (CS) measurement matrix design based on the block Toeplitz-structured matrix.

(a) (b) (c) (d)

Figure 6.3 Reconstruction performance test. (a) Original image of the letter 'T'. (b) Reconstructed image with a random matrix. (c) Reconstructed image with a partial Hadamard matrix. (d) Reconstructed image using the Toeplitz-structured matrix.

Figure 6.2 illustrates the partial measurement matrix (Φ in Eq. 6.1) generated from the digitalised SLM disk, where the elements in each row is generated by reshaping all the round patterns of a sampling mask (i.e. zoom-in window in Fig. 6.1) into a row vector (i.e. vectorization), and each row is corresponding to one measurement of the sample (x in Eq. 6.1). This measurement matrix could be approximated as a block Toeplitz matrix. Haupt *et al*. [**15**] and Sebert *et al*. [**16**] have shown that a Toeplitz-structured matrix is memory-efficient with fast implementation. By making a comparison between different CS measurement matrices, we found that the digitalised SLM shows a good performance in image reconstruction, as shown in Fig. 6.3. In this test, the same parameters were set (including the image size, the sampling rate and the reconstruction

algorithm). Specifically, the image size was set to 64 × 64 pixels, and each pixel represents a 0.5 × 0.5 mm^2 sampling grid. The size of each measurement matrix was set to 1200 × 4096, and each of the rows corresponds to one measurement vector. Thus, the compression rate was calculated as approximately 30%. The reconstruction algorithm used in this test is the Minimum Mean Square Error (MMSE) linear estimation [**17**].

Table 6.1 Image quality evaluation between different Compressive Sensing (CS) matrix as Spatial Light Modulator (SLM)

CS Measurement Matrix as SLM	PSNR [a]	SSIM [b]	FSIM [c]
Random matrix	19.15	0.93	0.56
Partial Hadamard matrix	19.12	0.94	0.56
Block Toeplitz-structured matrix	19.00	0.93	0.57

[a] Peak Signal-to-Noise Ratio (PSNR)

[b] Structural Similarity (SSIM)

[c] Feature Similarity (FSIM)

Table 6.1 shows the comparison of the reconstructed images obtaining by using the digitalised SLMs of a random matrix based SLM (64 × 64 pixels, each pixel 0.5 mm × 0.5 mm), a partial Hadamard matrix based SLM (64 × 64 pixels, each pixel 0.5 mm × 0.5 mm) and the proposed SLM. The image reconstruction quality is evaluated by: 1) Peak Signal-to-Noise Ratio (PSNR); 2) Structural Similarity (SSIM); 3) Feature Similarity (FSIM) [**18,19**]. As a result, the reconstruction quality achieved by using the proposed SLM (block Toeplitz-structured matrix) is very close to the result produced by the random matrix based SLM and the partial Hadamard matrix based SLM.

6.2.3 Spatial Sampling Performance

In terms of the spatial sampling performance, the similarity corresponding to two consecutive measurements with a 0.5-degree rotation angle (720 measurements per circle) of the SLM disk is approximately 0.5. Figures 6.4(a) and 6.4(b) show the performance of mechanical SLMs based on square sampling holes and round sampling holes, respectively. To measure a sample with a line-shaped edge or an arc-shaped edge, the minimum sampling pattern related to a square-hole-based SLM is limited by the dimension of the square holes. In contrast, the achievable sampling with a circular-hole-

based SLM could be smaller than the diameter of the circular holes. As shown in Fig. 6.4, the diameter of a circular sampling hole, *D*, is twice of the width of a square sampling hole, *d* (i.e. *D=2d*). Given a line-shaped pattern and an arc-shaped pattern, the achievable sampling dimension, *L*, is equal to the width of the square sampling hole. However, the same sampling performance can be achieved with the larger circular sampling hole for both the two situations.

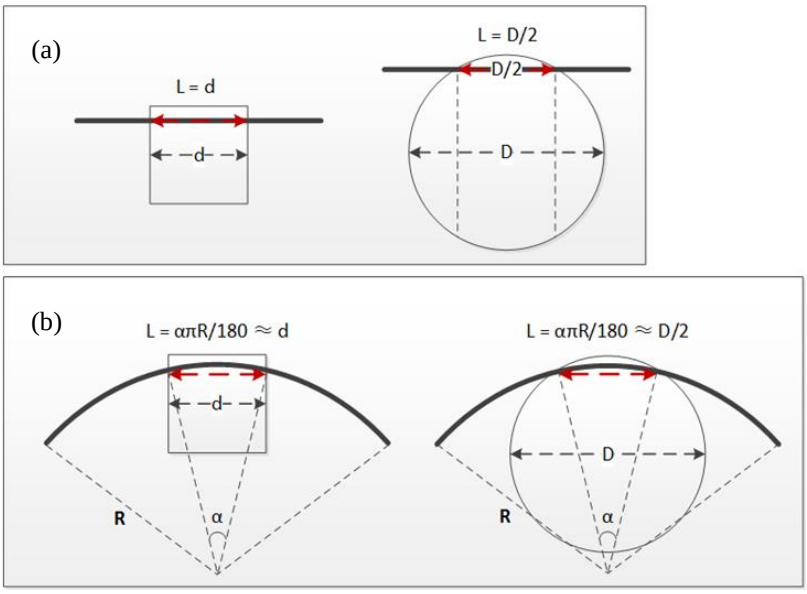

Figure 6.4 Sampling performance comparison between square-hole-based SLM and circular-hole-based SLM.

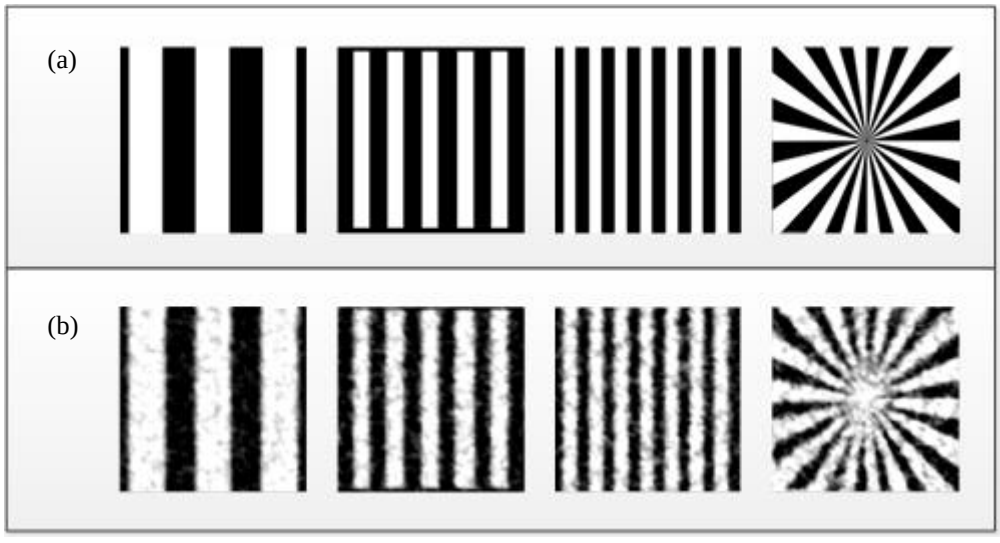

Figure 6.5 Spatial resolution test by using a series of resolution patterns. (a) Original images of the resolution patterns, 6-mm, 3-mm and 2-mm stripe patterns and a star pattern (left to right). (b) Reconstructed images.

In order to test the achievable spatial resolution of the proposed SLM, the imaging simulation was carried out with a series of resolution patterns. As shown in Fig. 6.5(a), the widths of the white stripes of the patterns are 6 mm, 3 mm and 2 mm, respectively, and a star pattern is also used for the study. Figure 6.5(b) shows the reconstructed images, in which each of the images has 128 × 128 pixels, and they were reconstructed based on 2000 compressive sampling, corresponding to a compression rate of 12%. As a result, a spatial resolution of better than 2 mm is achieved by using the digitalised SLM. This is significant, especially for infrared and THz imaging, where the use of the 2-mm sampling hole is desirable since it allows infrared and THz radiation with longer wavelengths to pass through.

6.2.4 Optical Transmission Performance

In order to estimate the optical transmission performance of the proposed SLM, a series of simulations were carried out, taking into consideration of increased wavelengths from 0.01 mm (30 THz) to 1 mm (0.3 THz). The upper left image in Fig. 6.6(a) shows one of the sampling areas on the digitalised SLM consisting of a number of 2-mm circular sampling holes, in which the holes are entirely transparent to visible and infrared imaging beam. However, when using longer-wavelength THz radiation for imaging, the transmission ability of the SLM will be affected due to diffraction effects, particularly when the wavelength of THz radiation is close to the size of the 2-mm sampling holes. Figure 6.6(a) illustrates the transmission effects at 30 THz, 3.0 THz, and 0.3 THz respectively, and Figure 6.6(b) shows the diffraction simulation result when 0.3-THz imaging beam passes through one of the 2-mm sampling holes. The result indicates that THz radiation (wavelength up to 1.0 mm) can still pass through the sampling holes with acceptable performance degradation. The image grid in the simulation had 512 × 512 pixels, corresponding to a real-world imaging area of 32 mm × 32 mm.

As a further illustration, we simulated the compressive THz imaging based on the optically degraded SLM (Fig. 6.6(a)). In the simulation, a cruciform pattern was used, as shown in the far left of Fig. 6.6(c). The size of the original image has 128 × 128 pixels, corresponding to a 32 mm × 32 mm imaging area, and each stripe represents 2-mm width (8 pixels) and 10-mm length (40 pixels). The other images in Fig. 6.6(c), from left to right, are the reconstructed images simulated at a frequency of 30 THz, 10

THz, 3.0 THz, 1.0 THz and 0.3 THz, respectively. We can find that the reconstructed cruciform patterns become blurred along with the increase in THz wavelengths. Nevertheless, the pattern can still be recognized even at 0.3 THz. In the simulation, the compression rate was set to 12% (2000 measurements) and the reconstructed algorithm was the MMSE [**17**]. We can, therefore, conclude that the proposed SLM is capable of compressive imaging from visible to THz frequencies.

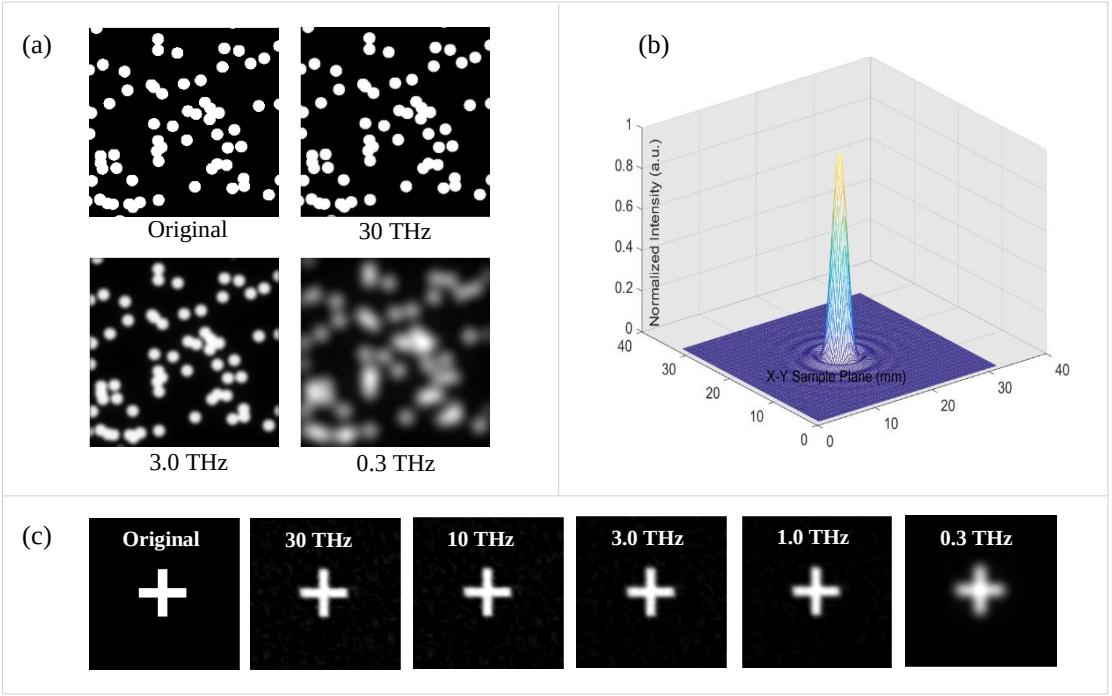

Figure 6.6 Optical transmission performance and terahertz (THz) compressive imaging simulation. (a) Simulated SLM optical transmission performance at various THz frequencies. (b) Simulated diffraction effects of the 0.3-THz imaging beam. (c) Simulated THz compressive imaging results in the frequency range from 0.3 THz to 30 THz.

6.3 Compressive Imaging with Visible Light Source

Setup of Visible-band Compressive Imaging System

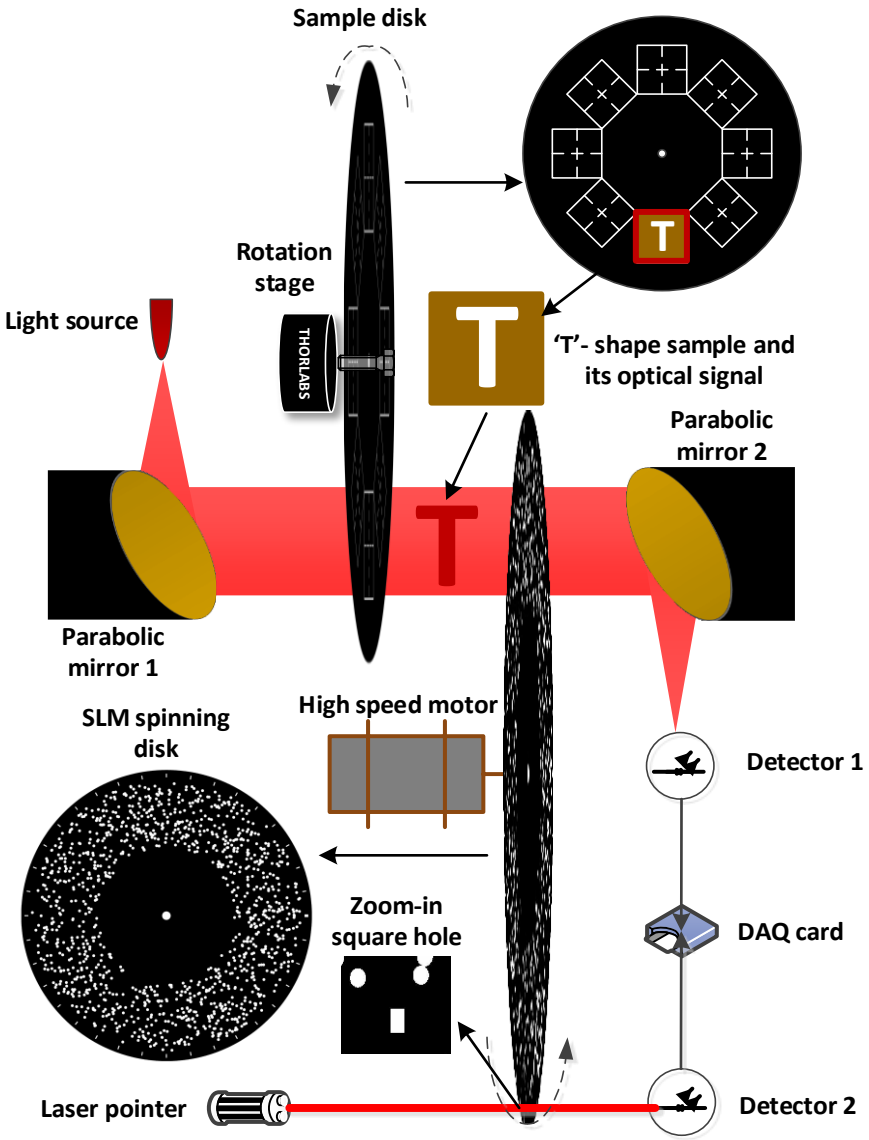

Figure 6.7 Schematic diagram of the compressive imaging system with a visible light source.

Figure 6.7 shows the schematic diagram of the visible-band compressive imaging system. The visible light from a LED source was collimated using a parabolic mirror. After transmitting through the sample and the SLM disk, the beam containing the optical information of the sample was then focused onto the detector by using another parabolic mirror. During the imaging process, the SLM disk was rotated continuously and automatically, driven by an electric motor (Gearbox: PLG 42S, Motor: BG 40×25, Controller: BGE 40, Dunkermotoren). In order to synchronise the motor position with

the data acquisition, a pair of laser diode and photodiode was used. The light beam from the laser diode propagates through the rectangle holes on the edge of the SLM disk which provides a precise mechanism for synchronisation. In the system, we can obtain one image per rotation thus the frame rate here is determined by the rotation speed of the SLM disk. Specifically, the rotation speed of the electric motor used in the system is 600 rotations per minute, providing a maximum image acquisition rate of about 10 frames per second (fps).

A motorised rotation stage (CR1-Z7, Thorlabs) was used to move a "sample disk". Eight sample holders were fabricated on the sample disk, and each holder has a size of 32 mm × 32 mm. As an example, Figure 6.7 shows a 'T' shape sample (the white represents 100% light transmission), and it is mounted on one of the sample holders. It should be pointed out that the diagram only demonstrates the case where a rotation stage is used to change the measured samples. We could also use a motorised translation stage to change the measured samples.

Unlike the compressive imaging of a single-frame signal, a multi-frame imaging task, such as 3D imaging, increases the computational burden on the reconstruction of multiple images or an image sequence. We, therefore, utilised the MMSE method as the reconstruction algorithm after balancing the image quality and time cost [**17**]. This is subsequently combined with a paralleled processing approach to make full use of the CPU. The PC we used for the study has a quad-core CPU with 32 Gbyte RAM. The processing software was developed based on MATLAB 2015a. Additional algorithms for the compressive imaging include 1) Gaussian pyramid for resampling the digitalised SLM disk; 2) Spline interpolation for obtaining the measurement signal from acquired raw signal [**20**]; 3) Wiener filter for denoise of reconstructed image [**21**]. Based on the imaging scheme, 100-frame image signals can be compressively sampled with a frame rate of 10 fps and reconstructed in 11.57 seconds.

Result and Discussion

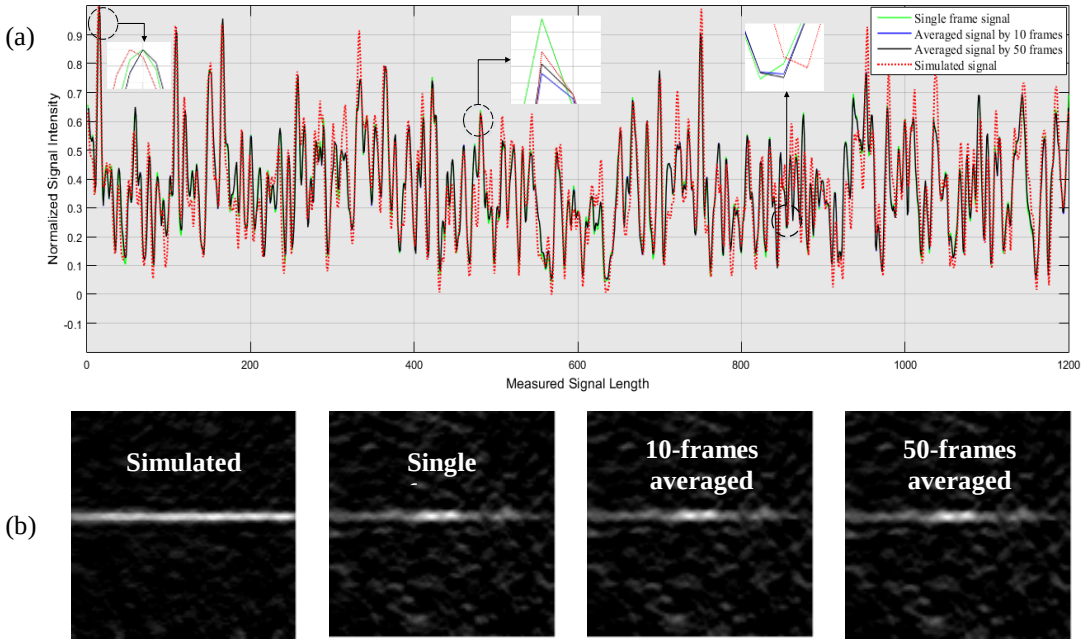

Figure 6.8 Compressive imaging of a narrow stripe sample with 1-mm width. (a) Comparison between the compressive signals with and without average processing. (b) Reconstructed images.

Figure 6.8(a) shows the measured signals for a sample (1-mm-wide cut-through stripe) which was fabricated on a 32 mm × 32 mm copper plate. The green line in Fig. 6.8(a) is the measured single-frame signal, while the blue and the black lines are the averaged signal of 10-frame and 50-frame signals, respectively. In addition, the red dashed line represents the simulated signal. It is evident that averaging over a multi-frame signal can improve Signal-to-Noise Ratio (SNR) (illustrated in the three zoom-in windows in Fig. 6.8(a)). Figure 6.8(b) shows the reconstructed images from their corresponding compressive signals. Each image with 96 × 96 pixels was reconstructed from 1200 measurements (i.e. a compression rate of 13%).

In order to quantify the spatial resolution, Figure 6.8(b) shows the reconstructed images using simulated and measured signals of the sample (1-mm stripe pattern). Each image has 96 × 96 pixels covering the real-world imaging area of 32 mm × 32 mm, and each pixel is therefore corresponding to 0.33 mm × 0.33 mm. As shown in Fig. 6.9, the Full Width at Half Maximum (FWHM) of the 1-mm-wide strip pattern was measured to be 1.0 mm and 1.1 mm for the reconstructed images from the simulated signal and the

measured signal, respectively, when taking into consideration of Line Spread Function (LSF). The achieved spatial resolution can be then determined as 1.1 mm.

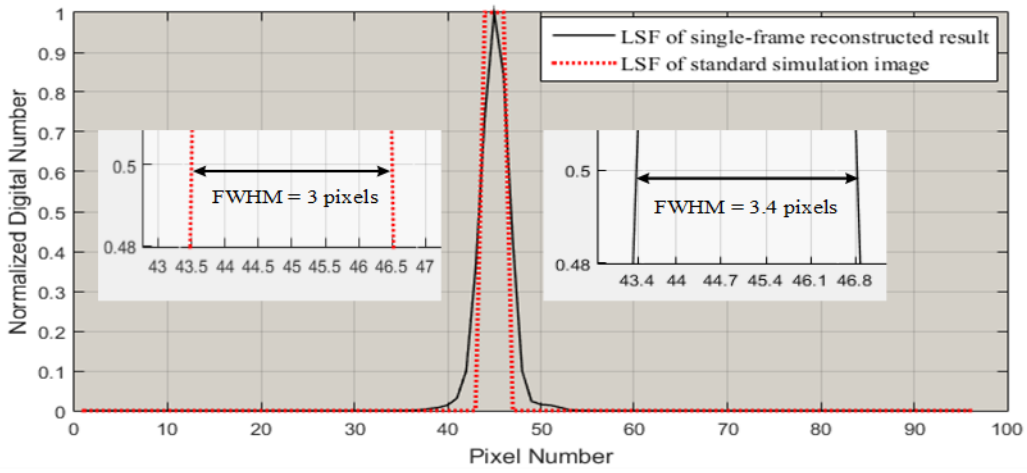

Figure 6.9 Measurement of the spatial resolution.

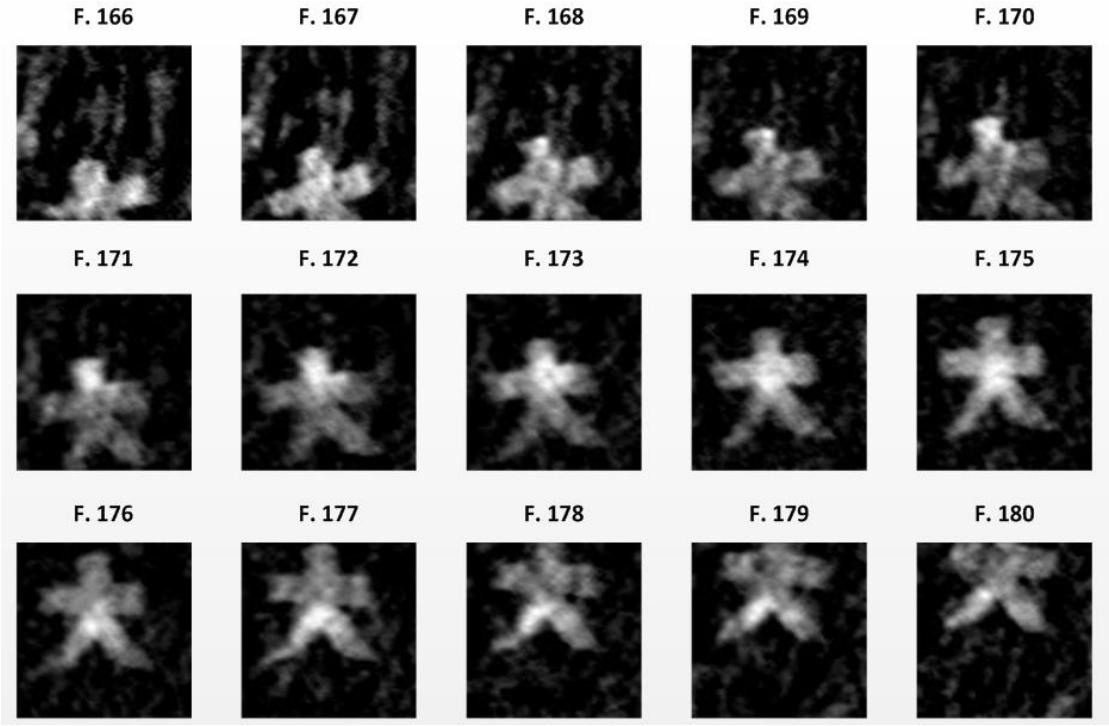

Figure 6.10 Video-rate compressive imaging for a moving sample '大'.

In contrast to image a static sample, rapid imaging technology is highly desirable for time-critical application. In order to demonstrate the imaging capability of the proposed SLM disk in video rate (> 8fps), we designed the samples from alphanumeric and Chinese characters (i.e. 'A', 'M', '5', '7', '大', '化', '中', '国'). The test samples were fabricated with copper tape, and the area occupied by the character is 100% transparent

to the visible imaging beam. These samples were fixed on the aforementioned sample disk which was mounted on a motorised rotation stage (CR1-Z7, Thorlabs). Each reconstructed image has 96 × 96 pixels, and the image was reconstructed based on 1200 measurements (i.e. 13% compression rate). When the sample '大' was moving across the sampling window, it was imaged in real time. As an example, Figure 6.10 shows 15 images extracted from the video which was recorded at a frame rate of approximately 10 fps.

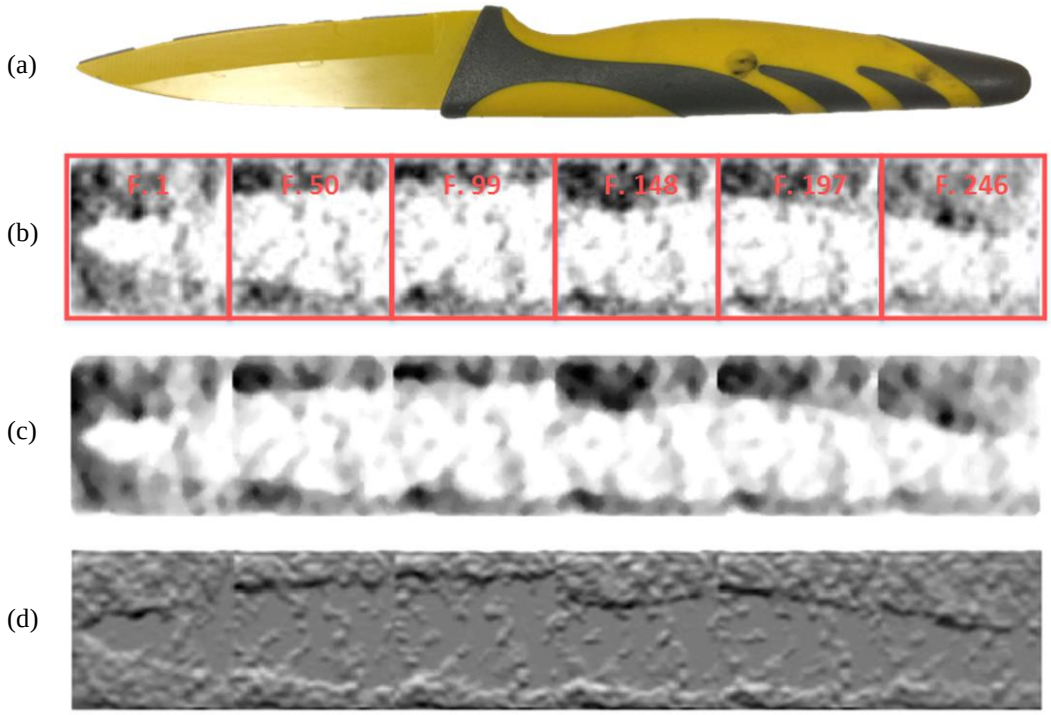

Figure 6.11 Video-rate compressive imaging on a 190-mm steel knife. (a) Photograph of the measured steel knife. (b) Reconstructed image corresponding to the frame image of interest. (c) Mosaic image to generate the whole shape of the imaged knife. (d) Edge-sharpened image for better recognition.

As a further illustration, we compressively imaged a 190-mm-long steel knife (see Fig. 6.11(a)) which is opaque to the visible imaging beam. The effective imaging area in the test is 32 mm × 32 mm. The knife was mounted on a motorised translation stage (M-521 Stage, Physik Instrumente). The stage was moving at a speed of 6.6 mm/s. As a result, 301 compressed image signals were acquired in 30 seconds at the frame rate of 10 fps. By dividing these images into a number of "shots" (49-frame images per shot) [**22–24**], we can extract therefore the keyframes automatically. A complete knife image

was then generated by combining these keyframes (Fig. 6.11(b)). Further image processing was carried out to enhance the quality and the visual effects of the image. Figure 6.11(c) shows the enhanced image by using a 5×5 median filter and grey scale inversion method [**25**], while Fig. 6.11(d) shows the edge-sharpened image by using the Sobel operator [**26**]. It should be pointed out that the space of saving the video of the moving knife is about 0.68 MB contributed by the compressive imaging. This can be compared with non-compression storage of 5.29 MB.

6.4 Compressive Imaging with Terahertz Light Source

Terahertz Quantum Cascade Lasers (QCLs)

THz imaging has relied for decades on the use of THz Time-Domain Spectroscopy (THz-TDS) systems. These systems employ large, and expensive femtosecond lasers which shine an ultrafast pulse into a photoconductive switch. The end-result is the emission of a broadband THz signal usually from 100 GHz up to a few THz. The main limitations with this approach are that the highest spectral resolution is not better than 5 GHz, and the magnitude of the intensity at frequencies 1–5 THz is on the order of μW. An alternative source which has emerged in 2002 is the THz-QCLs, which can be used for high-power, narrowband imaging [**27–29**]. It is based on the intra-band laser concept where lasing occurs due to electron energy loss in the conduction band. The active region is comprised of ~100 thin layers of GaAs and AlGaAs. These materials are grown using molecular beam epitaxy. Peak power of the radiation emitted from QCLs has been recorded at 1.01 W. Furthermore, it is possible to tune the emission frequency of the QCL by changing the voltage across it. The benefits of employing THz-QCLs for THz imaging compared to photoconductive switches is the increased lasing power at frequencies above 3 THz, a narrowband signal at a certain frequency which can be tuned, higher spectral resolution, and the avoidance of large, and expensive femtosecond lasers. Nowadays, the QCL remains the only high-power, coherent, compact source of THz radiation.

However, THz imaging is limited to single-pixel detectors which have a slow response time (1–100 ms). The technology for THz detectors is not much developed compared to the digital cameras (visible light) detectors, where an array of detectors is formed to take a large number of measurements within a very short period of time [**30**,**31**]. The standard methods for THz imaging make use of the raster scanning method, where the sample position is changed and scanning is performed pixel by pixel, obtaining M^2 measurements (M) for a $N \times N$ image, i.e. $M = N^2$. This approach is proven to successfully acquire an adequate image, but it requires a significant amount of time. Although different approaches such as attempts to build an array of detectors have been developed with an effort to improve the scanning speed, such multi-pixel detectors have significantly lower sensitivity than single-pixel devices, thus negating a major

advantage of QCLs. In addition, the complexity of the detectors and the cost could be high.

The solution to the slow image acquisition rate is to adopt an advanced signal processing technique, which is CS. It is a sub-Nyquist signal sampling technique that allows us to reconstruct a signal from a small number of random linear measurements. CS has linked and developed with THz imaging techniques for near a decade, and relevant systems built based on THz-TDS has been proposed in many papers. Nevertheless, to the best of the author's knowledge, no THz system with QCLs employing CS technique has been reported.

Setup of THz Compressive Imaging System

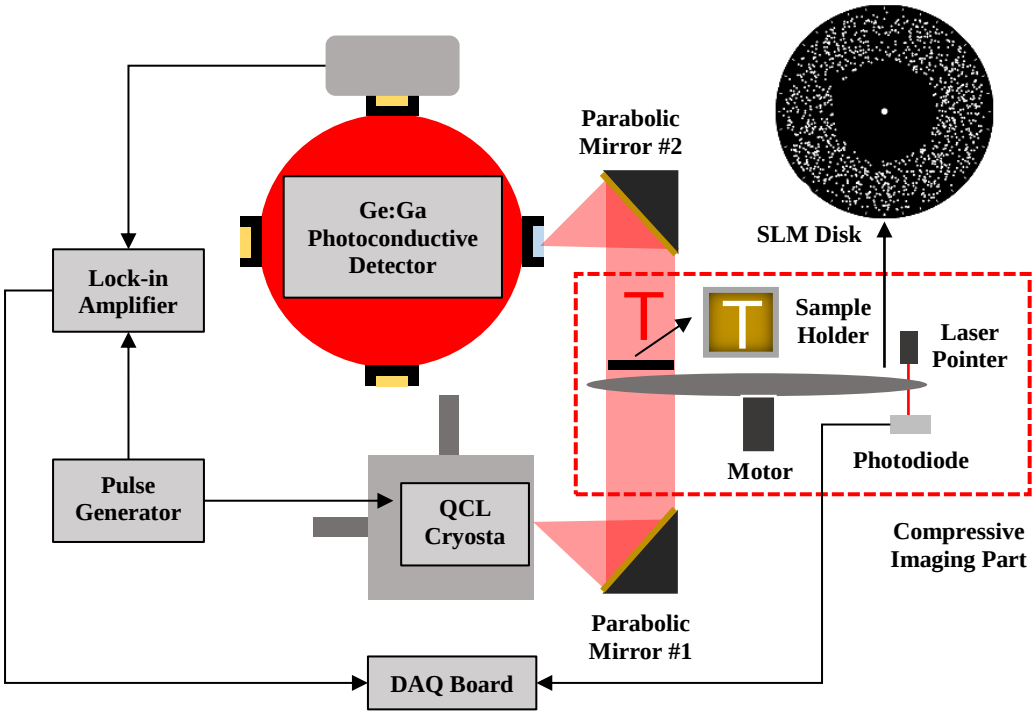

Figure 6.12 Schematic diagram of THz compressive imaging system with Quantum Cascade Lasers (QCLs).

Figure 6.12 shows the schematic diagram of the proposed THz compressive imaging system with QCLs source. A pulse generator was used to provide a 4-kHz Alternating Current (AC) signal with a 20% duty cycle to drive a QCLs device and trigger a lock-in amplifier. A parabolic mirror collimated the THz radiation emitted from the QCLs. After transmitting through the SLM disk and a fixed sample, the modulated THz beam containing the optical information of the sample was then focused onto a Gallium doped

Germanium (Ge:Ga) photoconductive detector by using another parabolic mirror. The measured THz signal was amplified via the Lock-in Amplifier (LIA) and recorded by a data acquisition board (NI USB-6212). Additionally, the SLM disk was rotated continuously and automatically, driven by an electric motor (Gearbox: PLG 42S, Motor: BG 40×25, Controller: BGE 40, Dunkermotoren). In order to synchronise the motor position with the data acquisition, a pair of laser diode and photodiode was used. The light beam from the laser diode propagates through a rectangle hole on the edge of the SLM disk which provides a precise mechanism for synchronisation. The whole system was developed by collaboration with the THz group in the University of Leeds, in which the QCL source and the signal detection unit were provided and aligned by the research group.

The QCLs was operating under the temperature of 25 K and providing the imaging beam at 2.7 THz. The detector has a response bandwidth of 4 kHz, theoretically allowing a data acquisition rate of 4,000 points per second. The practical acquisition rate was determined by the LIA setting. In this experiment, we set the LIA with 1-ms time constant which enables 1,000 measurements per second. Accordingly, the rotation speed of the motor was set to approximately one rotation per second (corresponding to the frame rate of 1 fps). This allows us to use 1,000 measurement points per rotation to reconstruct a good-quality image of 64 × 64 pixels (corresponding to 25% compression rate). Theoretically, this performance is equivalent to meet 5-fps compressive imaging but with a low compression rate.

In order to make the compressive imaging unit more stable, a compact and portable platform was designed and fabricated by 3D printing technique. As shown in Fig. 6.13, the blue area represents the 3D-printed platform by using plastic material, the size of which is 200 mm × 125 mm × 6 mm. Four holders on the platform are used to fix the sample holder, the SLM disk, the laser pointer and the photodiode (synchronisation unit), respectively. The whole compressive imaging unit can be moved along the propagation path of the THz imaging beam by using a translation stage. By combining with the above-mentioned imaging scheme, this compressive imaging unit can be well suited to many practical applications such as beam profiling and assistant tool for THz system alignment.

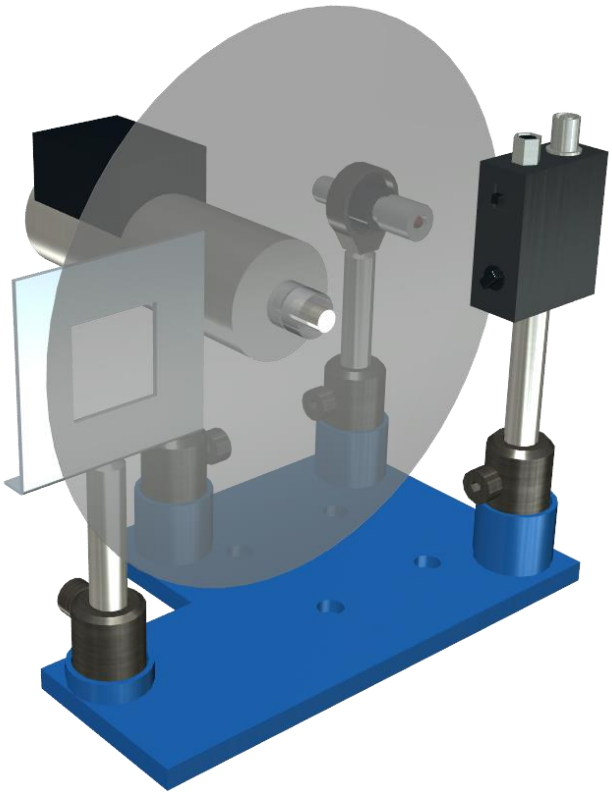

Figure 6.13 Compact and portable compressive imaging platform based on 3D printing technique. Blue area represents the printed platform with its size of 200 mm × 125 mm × 6 mm.

Result and Discussion

Several alphabet patterns and stripe patterns were fabricated on the copper sheet as samples. Note that, the line width of these patterns is 2 mm and the dimension of the sample is 20 mm × 20 mm. The area occupied by the patterns is transparent to the THz imaging beam. Figure 6.14(a) shows the simulated image of the THz compressive imaging with a 5% compression rate, where the image with 64 × 64 pixels each was reconstructed by 200 measurements. Figure 6.14(b) shows the images that were reconstructed from practical measurements with 5-fps imaging rate. We can only partially recognise the measured patterns, which may be due to the non-uniform THz imaging beam pattern.

A repeatable measurement was carried out with a lower compression rate. Figure 6.15(a) shows the simulated images of the high-quality THz compressive imaging result with a 25% compression rate, where each of the images was reconstructed by 1000 measurements. Figure 6.15(b) shows the images corresponding to the practical

measurement result under a slow imaging rate of 1 fps. It can be found that the sample with 2-mm stripe patterns is able to be resolved. However, the image quality is still affected by the non-uniform illumination of the sample area.

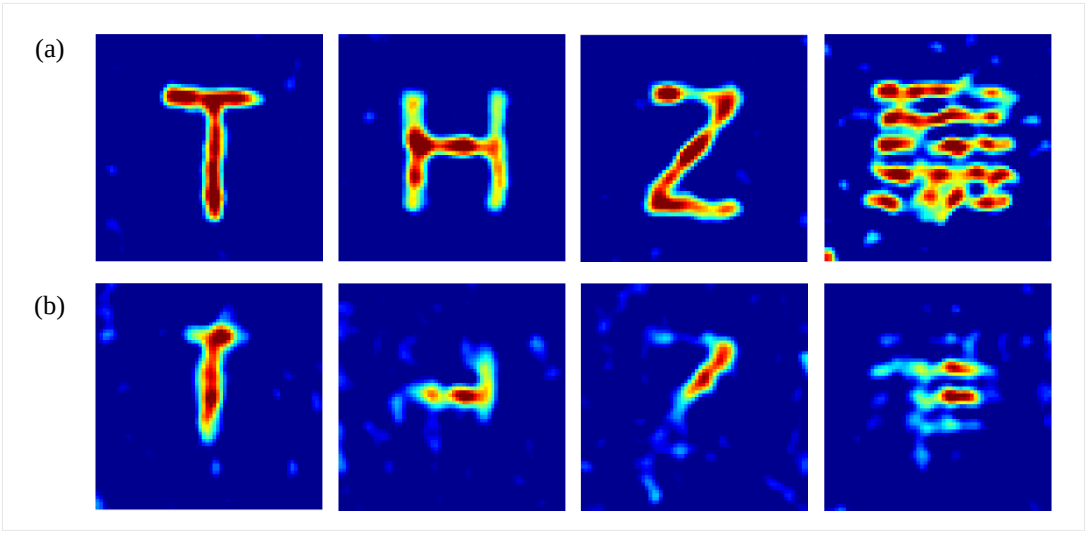

Figure 6.14 THz compressive imaging with alphabet pattern and stripe samples with 5% compression rate. (a) Simulated THz compressive imaging result. (b) Practical THz compressive imaging result.

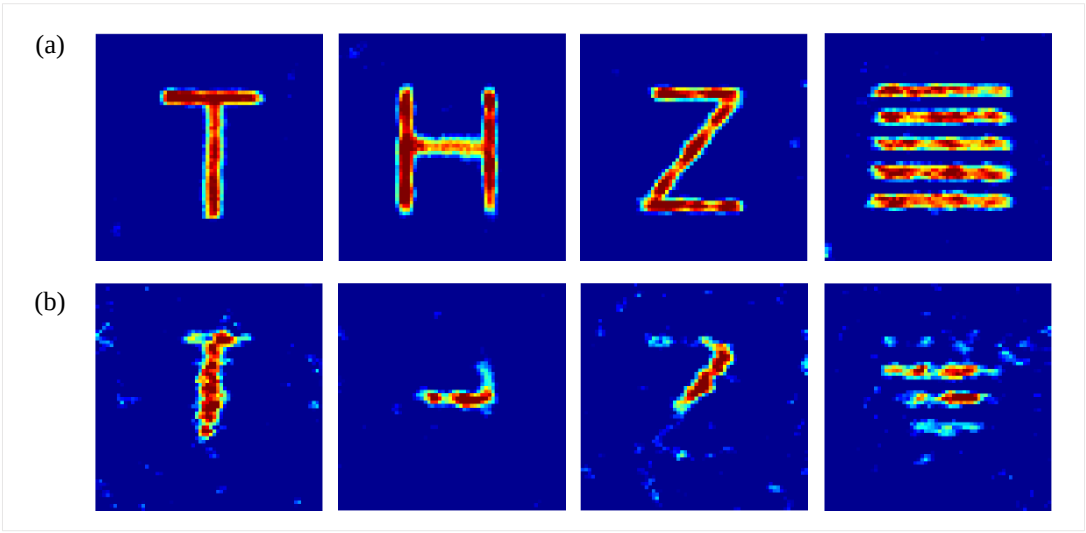

Figure 6.15 THz compressive imaging with alphabet pattern and stripe samples with 25% compression rate. (a) Simulated THz compressive imaging result. (b) Practical THz compressive imaging result.

In order to characterise the THz imaging beam emitted from the QCLs source, a beam profile of the collimated THz beam was obtained by compressive imaging. This was realised by removing the sample and taking a series of ‘images’ of the empty sample

area along with the THz beam propagation direction, which also yields 3D beam profiling. Figure 6.16 (a) shows that the pattern of the THz imaging beam is annular, with an outer diameter of approximately 30 mm. As shown in Fig. 6.16(a), the z- axis represents the position (in mm) along propagation of the collimated THz radiation. Five THz images with a 30-mm step were reconstructed from their corresponding compressive signals. Fig. 6.16(b) and 6.16(c) show the cross-sectional images extracted from latitudinal and longitudinal directions of the captured 3D beam profile, illustrating a non-uniform radiation feature. This is a consequence of the non-Gaussian far-field beam profile of "standalone" QCLs and explains the limitation in the imaging area obtained in Fig. 6.14 and Fig. 6.15.

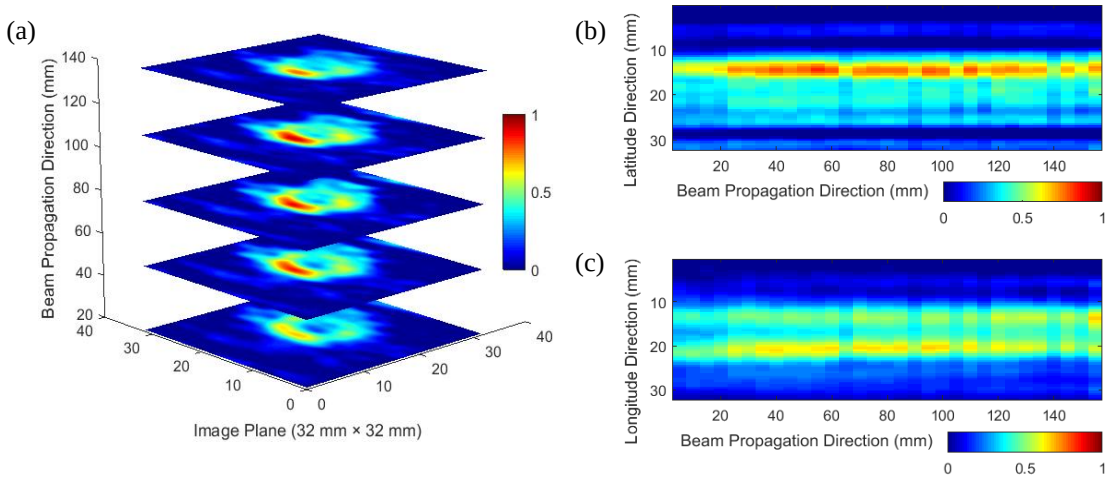

Figure 6.16 THz beam profiling via compressive imaging. (a) THz beam patterns selected from different positions along the THz beam propagation path. (b) Cross-sectional image extracted from the latitudinal direction of the imaging plane. (c) Cross-sectional image extracted from the longitudinal direction of the imaging plane.

6.5 Conclusion

To summarise, in this chapter, 1) a mechanical SLM has been developed as a core part of a compressive imaging system. The SLM was designed based on a block Toeplitz matrix and demonstrated a good reconstruction performance when comparing with other CS measurement matrices while it requires a less memory burden. The design of circular sampling patterns decreases the scattering effects and the diffraction effects resulted from the imaging beam with longer wavelengths; 2) a video-rate compressive imaging system has been developed with a visible LED source. The system is capable of capturing a video sequence at an imaging rate of 10 fps. The spatial resolution of the system is achieved as approximately 1 mm; 3) a THz compressive imaging system driven by QCL source has been developed. The proposed system and imaging scheme are capable of profiling the THz imaging beam, which can be used as an assistant tool for THz imaging system alignment. Non-uniform THz beam emitted from the QCL source was imaged.

It can be seen that the proposed SLM is well suitable for the compressive imaging at the frequency range from visible to THz band. It could be applicable to build a compressive FF-OCT system by using the SLM pattern in the near future since the 2D compressive sampling at image plane has been proved in the study.

References

[1] E. J. Candès and T. Tao, “Near optimal signal recovery from random projections: Universal encoding strategies?” IEEE Transactions on Information Theory, vol. 52, no. 12, pp. 5406-5425, 2006.

[2] M. E. Gehm, R. John, D. J. Brady, R. M. Willett, and T. J. Schulz, "Single-shot compressive spectral imaging with a dual-disperser architecture," Optics Express, vol. 15, no. 21, pp. 14013-14027, 2007/10/17 2007.

[3] M. F. Duarte, M. A. Davenport, D. Takhar, J. N. Laska, T. Sun, K. F. Kelly, and R. G. Baraniuk, "Single-pixel imaging via compressive sampling," IEEE Signal Processing Magazine, vol. 25, no. 2, pp. 83-91, 2008.

[4] E.J. Candès, J.K. Romberg and T. Tao, "Stable signal recovery from incomplete and inaccurate measurements". Communications on Pure and Applied Mathematics: A Journal Issued by the Courant Institute of Mathematical *Sciences*, vol. 59, no. 8, pp. 1207-1223, 2006

[5] E.J. Candès and T. Tao., "Decoding by linear programming". IEEE Transactions on Information Theory, vol.51, no. 12, pp. 4203-4215, 2005.

[6] J. Haupt, W. U. Bajwa, G. Raz, and R. Nowak, "Toeplitz compressed sensing matrices with applications to sparse channel estimation," IEEE Transactions on Information Theory, vol. 56, no. 11, pp. 5862-5875, 2010.

[7] H. Rauhut: ‘Compressive sensing and structured random matrices', In Fornasier, M. (Ed.): ‘Theoretical Foundations and Numerical Methods for Sparse Recovery' (De Gruyter, 2010), vol. **9**, pp. 1–92

[8] G. Zhang, S. Jiao, and X. Xu., 2010, July. Compressed sensing and reconstruction with semi-hadamard matrices. In 2010 2nd International Conference on Signal Processing Systems (Vol. 1, pp. V1-194). IEEE.

[9] N. Mohan, I. Stojanovic, W. C. Karl, B. E. Saleh, and M. C. Teich, "Compressed sensing in optical coherence tomography," in Three-Dimensional and Multidimensional Microscopy: Image Acquisition and Processing XVII, 2010, vol. 7570, p. 75700L: International Society for Optics and Photonics.

[10] X. Liu, and J. U. Kang, "Compressive SD-OCT: the application of compressed sensing in spectral domain optical coherence tomography," Optics Express, vol. 18, no. 21, pp. 22010-22019, 2010.

[11] D. Xu, Y. Huang, and J. U. Kang, "Volumetric (3D) compressive sensing spectral domain optical coherence tomography," Biomedical Optics Express, vol. 5, no. 11, pp. 3921-3934, 2014.

[12] H. Shen, L. Gan, N. Newman, Y. Dong, C. Li, Y. Huang, Y. Shen, "Spinning disk for compressive imaging," Optics Letters, vol. 37, no. 1, pp. 46-48, 2012.

[13] T. Vasile, V. Damian, D. Coltuc, and M. Petrovici, "Single pixel sensing for THz laser beam profiler based on Hadamard transform," Optics & Laser Technology, vol. 79, pp. 173-178, 2016.

[14] K. E. Peiponen, A. Zeitler, M. Kuwata-Gonolami: 'Generation and detection of terahertz radiation'. In Rhodes, W.T. (Ed.): 'Terahertz Spectroscopy and Imaging' (Springer, USA, 2013), vol. **171**, pp. 1–25.

[15] J. Haupt, W. U. Bajwa, G. Raz, and R. Nowak, "Toeplitz compressed sensing matrices with applications to sparse channel estimation," IEEE Transactions on Information Theory, vol. 56, no. 11, pp. 5862-5875, 2010.

[16] F. Sebert, L. Ying, and Y. M. Zou, "Toeplitz block matrices in compressed sensing," *arXiv preprint arXiv:0803.0755*, 2008.

[17] L. Gan, "Block compressed sensing of natural images," in 2007 15th International Conference on Digital Signal Processing, 2007, pp. 403-406: IEEE.

[18] A. Hore and D. Ziou, "Image quality metrics: PSNR vs. SSIM," in 2010 20th International Conference on Pattern Recognition, 2010, pp. 2366-2369: IEEE.

[19] L. Zhang, L. Zhang, X. Mou, and D. Zhang, "FSIM: A feature similarity index for image quality assessment," IEEE Transactions on Image Processing, vol. 20, no. 8, pp. 2378-2386, 2011.

[20] H. Hou and H. Andrews, "Cubic splines for image interpolation and digital filtering," IEEE Transactions on Acoustics, Speech, and Signal Processing, vol. 26, no. 6, pp. 508-517, 1978.

[21] S. R. Islam, S. P. Maity, and A. K. Ray, "On compressed sensing image reconstruction using multichannel fusion and adaptive filtering," in 2015 International Conference on Image Processing Theory, Tools and Applications *(IPTA)*, 2015, pp. 479-484: IEEE.

[22] J. Calic and E. Izuierdo, "Efficient key-frame extraction and video analysis," in Proceedings. International Conference on Information Technology: Coding and Computing, 2002, pp. 28-33: IEEE.

[23] Y. Zhuang, Y. Rui, T. S. Huang, and S. Mehrotra, "Adaptive key frame extraction using unsupervised clustering," in Proceedings 1998 International Conference on Image Processing. ICIP98 (Cat. No. 98CB36269), 1998, vol. 1, pp. 866-870: IEEE.

[24] N. Ejaz, T. B. Tariq, and S. W. Baik, "Adaptive key frame extraction for video summarization using an aggregation mechanism," Journal of Visual Communication and Image Representation, vol. 23, no. 7, pp. 1031-1040, 2012.

[25] N. Gallagher and G. Wise, "A theoretical analysis of the properties of median filters," IEEE Transactions on Acoustics, Speech, and Signal Processing, vol. 29, no. 6, pp. 1136-1141, 1981.

[26] S. Gupta and S. G. Mazumdar, "Sobel edge detection algorithm," International Journal of Computer Science and Management Research, vol. 2, no. 2, pp. 1578-1583, 2013.

[27] L. H. Li, C. Li, J. X. Zhu, J. Freeman, P. Dean, A. Valavanis, A. G. Davis, and E. H. Linfield, "Terahertz quantum cascade lasers with> 1 W output powers", Electronics Letters, vol. 50, no. 4, pp. 309-311, 2014.

[28] P. Dean, Y. L. Lim, A. Valavanis, R. Kliese, M. Nikolić, S. P. Khanna, M. Lachab, D. Indjin, Z. Ikonić, P. Harrison, A. D. Rakić, E. H. Linfield, and A. G Davies, "Terahertz imaging through self-mixing in a quantum cascade laser", Optics Letters, vol. 36, no. 13, pp. 2587-2589, 2011.

[29] P. Dean, A. Valavanis, J. Keeley, K. Bertling, Y.L. Lim, R. Alhathlool, A.D. Burnett, L.H. Li, S.P. Khanna, D. Indjin, T. Taimre, A.D. Rakić, E.H. Linfield, A. G. Davies, "Terahertz imaging using quantum cascade lasers—a review of systems and applications", Journal of Physics D: Applied Physics, vol. 47, no. 37, 2014.

[30] A. W. M. Lee, B. S. Williams, S. Kumar, Q. Hu, J. L. Reno, "Real-time imaging using a 4.3-THz quantum cascade laser and a 320/spl times/240 microbolometer focal-plane array", IEEE Photonics Technology Letters, vol. 18, no. 13, 2006.

[31] A. W. M. Lee, Q. Qin, S. Kumar, B. S. Williams, Q. Hu, "Real-time terahertz imaging over a standoff distance (>25meters)", Applied Physics Letters, vol. 89, no. 14, 2006.

Chapter 7 Conclusion and Future Work

In this thesis, a single-point Spectral-Domain (SD) Optical Coherence Tomography (OCT) system and a Full-Field (FF) OCT systems have been developed with the following advantages: high resolution, high imaging speed, effective cost, compactness and portability. The intended contribution is to optimise OCT techniques, thereby improving the practicability for industrial applications.

Focusing on the emerging pharmaceutical applications, the SD-OCT has been used to investigate the applicability of resolving pharmaceutical film coatings with different common formulations. Also, the SD-OCT has been used to monitor the coating process of small pellets on a pilot scale (3 Kg) with a fluid bed coater. For pharmaceutical tablets/pellets with more complex coating structures and thinner coating layers, the FF-OCT has been used to characterise the inner structures of multi-layer micropellets. It has been also used to differentiate paracetamol tablets from branded and generic suppliers through a thin film coating used in GlaxoSmithKline (GSK) Panadol tablet.

For a completely new area of application, such as using OCT technique to evaluate the effectiveness of detergent products, the FF-OCT has been used to discriminate and quantify the cleanliness/stain removal from clean, washed and soiled cotton fabric samples, and the FF-OCT has also been used to resolve and quantify the soilalibity from the kitchen countertops that are treated with different-level greasy soils.

Furthermore, in order to explore next-generation OCT system, i.e. ultrahigh-speed (50 kA-scans/s) and ultrahigh-resolution (better than 1 μm) Three-Dimensional (3D) OCT imaging technique, Compressive Sensing (CS) imaging technology at visible and terahertz (THz) frequencies have been investigated, where a Spatial Light Modulator (SLM) with high compression rate has been developed for the CS imaging.

Overall, below summarises the ***key contributions*** of each chapter in detail:

Chapter 3: In-line Monitoring Pharmaceutical Coating Process

Compared with conventional Time-Domain (TD) OCT, the significant advantages of SD-OCT technique are faster measurement speed and higher Signal-to-Noise Ratio (SNR), which is, therefore, an appropriate technique to be employed as a novel Process Analytical Technologies (PAT) tool to monitor pharmaceutical coating process through

the coaters used in the industry. SD-OCT has been being attractive to the pharmaceutical community due to the reported application potentials. In this chapter, a cost-effective single-point SD-OCT system was reported. The SD-OCT was driven by a customised light source with an achieved coupling efficiency of 44%, where a Superluminescent Diode (SLD) was used. This enables the cost of the proposed system is much lower than other reported SD-OCT systems in the application, in which either the broadband supercontinuum lasers or the composite SLD source was used. The axial and lateral resolutions achieved by the SD-OCT are 9 μm and 19 μm, respectively.

The SD-OCT imaged a series of tablets with different common coatings. From the experimental results, it is found that the ability to image coatings for an SD-OCT measurement depends on the properties relevant to coating pigment, coating materials, tablet core and coating process. In particular, it is found that the SD-OCT cannot discriminate the coating/core interface on the tablets where titanium dioxide (TiO_2) is contained in coating formulations. The film coatings on the tablets even without TiO_2 also cannot be measured due to the scattering effects and/or narrowed differences of refractive index between the coating and the tablet core. It is demonstrated that the applicability of the SD-OCT technique as a PAT tool is highly dependent on the formulation of functional polymeric coatings.

A preliminary study was carried out to monitor the coating process for pilot scale (3 Kg) pellets with the proposed SD-OCT system. The coating material used for the in-line measurement was determined before the in-line measurement by imaging several film coated pellets with different coating formulations. From the in-line experiment results, it was found that the increase in coating thickness along with the coating process time is in general agreement with the results obtained from the off-line OCT and particle size analyser measurements. It is demonstrated that the proposed SD-OCT with lower costs and better flexibility has the capability of the on-site and in-line monitoring of pellet coating process through fluid bed coater.

Chapter 4: Ultrahigh-resolution Imaging of Thin Film Coatings

Compared with conventional SD-OCT, the time-domain FF-OCT is more suitable to do 3D imaging since only a single axial scan is required for 3D data acquisition. As one of the off-line measurement techniques for pharmaceutical applications, it had been discussed but with a common resolution level. In this chapter, an FF-OCT system with

Ultrahigh-Resolution (UHR) performance (i.e. 1-µm axial resolution and 1.6 µm lateral resolution) was proposed. This system was driven by a broadband Light-Emitting Diode (LED) which enables an approximately 1-µm axial resolution, and the use of two objectives with a Numerical Aperture (NA) of 0.3 achieves a lateral resolution of 1.6 µm. In order to improve the measurement speed, a continuous measurement scheme is developed, where simulations were conducted to compare it with the classic phase-shift method, demonstrating a close performance.

Paracetamol tablets from generic and branded suppliers are differentiated by the proposed FF-OCT system. From the experimental results, it is found that a thin film coating at approximately 4 µm can be resolved from GSK's Panadol tablets, which is absent on the generic tablets. In addition, it is found that particulates adsorbed to the tablet surface on generics are resolved, indicating that branded tablets have a smoother surface finish.

The proposed UHR FF-OCT system acquired 3D images of micropellets (0.8-mm diameter). As a result, the measured pellet sample with three thin coating layers was characterised. The FF-OCT result then was validated by measuring the same sample with X-ray Micro Computed Tomography (XµCT). In order to derive the Refractive Index (RI) of each coating layer, a comparison was made between the A-scan signals of OCT and XµCT. Moreover, a 3D image segmentation technique was developed, which enables a fine coating thickness map to be obtained automatically. It is demonstrated that the FF-OCT system can be used as a powerful off-line inspection tool to analyse the pellets even with thinner and multi-layer coatings.

Chapter 5: An Alternative Method to Evaluate Cleaning Effectiveness of Washing Products

In this chapter, the application potential of the proposed UHR FF-OCT is further exploited, such as the application in the detergent industry.

From the study on cotton fabrics, it is found that the FF-OCT can resolve the removal of oily and fatty stains in washed and unwashed fabrics, which have been subjected to cleaning processes. In particular, by the achieved axial and lateral resolutions of 1 µm and 1.6 µm, respectively, the micron-sized fibres/fibrils consisting of the cotton fabric can be resolved. The fibres, which can be detected from the sub-surface area, enables

the assessment of the cleaning effect. A stain removal assessment method is developed by analysing the reconstructed 3D datacube. The volume of the detectable sub-surface fibres can be used to evaluate the cleaning effect related to the FF-OCT measurement. The technique results are verified by the current gold standard method of colourimetry, but it has also shown the applicability without the invasive staining required by colourimetry.

From the study on the hard surface sample, the UHR FF-OCT was used to carry out the surface profilometry measurements on the kitchen countertop treated with different-level soils. It is found that the topography image containing the dimension information of the soil can be used to discriminate the soilability of the soiled samples. The soilability can then be quantified by calculating the area covered by soils.

Chapter 6: Compressive Imaging Technique for New-gen FF-OCT

As for SD-OCT imaging modality, there is a trade-off between higher axial resolution and deeper imaging depth due to the Nyquist-criterion for a spectrometer. As for FF-OCT imaging modality, the finer 3D image requires a huge data storage (i.e. > 100 GB). CS technology could provide an effective solution. In this chapter, the state-of-art CS imaging technique is investigated.

A block Toeplitz matrix was developed and fabricated to a mechanical SLM based on stainless-steel substrate. The SLM illustrated a reconstruction performance which is close to those well-studied CS measurement matrices (i.e. fully random matrix). In practical imaging test, the round sampling holes (chemically etched on the substrate) can minimise scattering effects, and each of the sampling holes with the 2-mm diameter allows the beam with longer wavelength to pass through them without diffraction effects.

Imaging studies were conducted at both visible and THz frequencies. From the experimental results, it can be found that the proposed SLM enables video-rate compressive imaging at the visible band. A hundred image signals (each has 96 × 96 pixels) were compressed and acquired simultaneously with a compression rate of 12% and a frame rate of 10 frames per second. At THz band, a THz imaging beam emitted from THz Quantum Cascade Lasers (QCLs) was profiled by compressive imaging with

the SLM. These findings will contribute to the future study toward developing a suitable compressive FF-OCT.

The author would like to acknowledge the ***work contributed by collaborators***:

The author acknowledges Colorcon Ltd. (Dartford, UK) for providing the table samples used in the SD-OCT imaging applicability study (**Chapter 3**).

The author acknowledges Bosch Hüttlin GmbH (Schopfheim, Germany) for providing the pellet samples used in the SD-OCT in-line monitoring study and for inviting the author to carry out the in-line measurement in Germany (**Chapter 3**).

The author acknowledges Neil Turnbull from Pfizer Ltd. (UK) for supplying samples of coated pellets used in the micropellet imaging study (**Chapter 4**).

The author acknowledges Bryan Williams, from the Department of Eye and Vision Science at the University of Liverpool, for developing the 3D segmentation algorithm used in the analysis of micropellet inner structures (**Chapter 4**).

The author acknowledges Uyai Ikpatt from Unilever Port Sunlight Centre (Port Sunlight, UK) for supplying the cotton fabric samples and kitchen countertop samples used in the study of using OCT for evaluation of stain removal (**Chapter 5**).

The author acknowledges Alexander Valavanis, from the School of Electronic and Electrical Engineering at the University of Leeds, for supplying the THz QCL source and the signal detection components used in the study of compressive imaging (**Chapter 6**).

Recommendations for possible ***future work*** related to this thesis are discussed below:

Based on the conclusions drawn from above and taking into account the limitations of the work presented in each chapter, future work can be carried out in the following area.

From Chapter 3, despite the potential of our developed SD-OCT as a PAT tool has been illustrated, the pellet hit rate revealed by the effective B-scan is approximately 20%–30%. This, on one hand, results from the random speed of the flying pellets across the sensor head. A possible solution is to fabricate a shaped trough (i.e. ‘U’ shape, trapezoid and arc) and fix it with the sensor head. The friction between trough surface and flying pellet could slow down the pellet flying through the probe beam. Depending on the

shape of the trough, it may allow more pellets flying around the sensor head to be detected. Another possible extension of this work would be spectrometer triggering based on hit pellets.

In Chapters 4 and 5, the applicability of the developed UHR FF-OCT has been discussed in terms of off-line inspection. Ways to transition and develop it to an attractive in-line technique still need more work. Possible future work may include ultra-fast FF-OCT imaging by using a fibre bundle. In addition, we have discussed the limitation in imaging depth due to the used high-NA objectives. Depending on the imaged sample, another possible area for future work would be the increase of the practical imaging depth by compensating the reference arm. Thirdly, since our UHR FF-OCT system can be set up with fewer optical and electrical components, it can be changed to a common-path UHR FF-OCT configuration by using a single Mirau objective. This would be more suitable to deploy an OCT device to the on-site evaluation of car paint quality for the automobile industry, such as characterisation of the individual paint layer thickness of multiple layered automotive paints and analysis of flakes used in metallic base coat layer.

In Chapter 6, the ability of the proposed SLM as a measurement matrix is advantageous, especially for the measurement of a large volumetric dataset. Introducing an SLM into FF-OCT system to achieved 3D compressive imaging remains an issue. Possible future work may include compressive depth scanning through modulating the movement of the reference arm. Moreover, we can notice that metamaterial has attracted enormous attention from the scientific community, and they have been proved to be a breakthrough technology. To develop a metamaterial-based SLM could achieve compressed sampling at the *en-face* plane, and it is a significant topic for future work.